Pulsed Blue and Ultraviolet Laser System for Fluorescence Diagnostics based on Nonlinear Frequency Conversion

Cheng, Haynes Pak Hay

Publication date:
2011

Document Version
Publisher's PDF, also known as Version of record

Diode Pumped Solid-State Laser for Pulsed UV Generation

Haynes Pak Hay Cheng

鄭栢禧

Main Supervisor: Christian Pedersen

Co-Supervisors: Ole Bjarlin Jensen
Peter Eskil Andersen
Paul Michael Petersen

February 16, 2011

Abstract

The motivation for the current thesis work is to build a compact, efficient, pulsed, diode-pumped solid-state (DPSS) laser at 340 nm to be used for autofluorescence imaging and related cancer diagnostic experiments. By exciting endogenous fluorophores in the UV spectrum, autofluorescence imaging eliminates the need for prior preparation on the patient, and further reduces the cost of fluorescence imaging, and potentially, cancer diagnostic.

By taking advantage of the relatively short wavelength of the 946 nm transition in a quasi-three-level Nd:YAG laser, the target 340 nm wavelength could be reached through sum-frequency generation (SFG) with a frequency-doubled 532 nm Nd:YAG laser. However, since the quasi-three-level transition suffer from reabsorption loss and a ten-fold reduction in stimulated emission cross-section compared to the four-level 1064 nm transition, optimization of the 946 nm laser is non-trivial.

Detailed investigation into pump beam optimization has been carried out for an end-pumped 946 nm CW laser. Using an innovative external cavity tapered diode laser as pump source, a record 800 mW of output power was obtained using a single-emitter diode laser pump source. The spatial and spectral properties of the pump source were also investigated individually, and it was concluded that a broad spectrum tapered diode pump source may be most stable and cost-effective.

To generate high peak power pulsed output, Q-switched lasers were considered. In particular, synchronized Q-switching between a 946 nm and 1064 nm Nd:YAG laser was achieved in a passive approach. To the author's knowledge, stable, passive synchronization between a quasi-three-level and a four-level laser was achieved for the first time over a wide range of pump powers. The minimum delay between the two pulses was 64 ns, which translates into a 79% temporal overlap when compared to the zero-delay scenario. The minimum timing jitter between the two pulses was 9 ns, which is one-standard deviation of the delay measurements. This is comparable to previously published results for an actively synchronized system if either a four-sigma or six-sigma definition was used.

Detailed investigation into the relative timing jitter between the two synchronized pulses was also carried out, where it was found that the lower limit on the relative jitter, determined by pump power fluctuations and

amplified spontaneous emission, was 6 ns. Comparing this to the 9 ns relative jitter achieved in the passive system shows the performance penalty incurred in using the passive approach.

Lastly, practical applications of compact semiconductor and DPSS lasers in the blue and UV spectral region are presented. A CW tapered diode at 808 nm was directly frequency-doubled to 404 nm using an external cavity, and was used in an animal experiment for a novel approach in estimating photosensitizer concentration using fluorescence imaging. Secondly, a frequency-tripled, 355 nm, Q-switched, DPSS laser was used in a preliminary clinical investigation in autofluorescence diagnostic of skin cancer. While the preliminary results are promising, the system would benefit from a 340 nm light source that tunes into the absorption peaks of endogenous fluorophores. The imaging system would also benefit from a high-peak power light source that would increase the signal-to-noise ratio.

Based on the clinical results, there is a clear need for a high peak-power, 340 nm pulsed laser source for autofluorescence experiments. While the current results on passively synchronized Q-switching seem very promising for SFG generation into such wavelength, the technique could be equally applied to other wavelengths; specifically, those in the blue and UV spectral region. Using the passive synchronization technique and the optimization procedure reported for quasi-three-level lasers, a new generation of high peak power, pulsed, blue and UV laser light sources could be realized.

Abstrakt

Motivationen for denne afhandling er ønsket om en kompakt, effektiv, pulset diodepumpet faststoflaser ved 340 nm, som kan anvendes til autofluorescensafbildning og kræftdiagnose. Ved at excitere endogene fluoroforer med ultraviolet lys kan autofluorescensafbildning eliminere tidskrævende patientforberedelse og dermed yderligere reducere omkostningerne i forbindelse med kræftdiagnostik.

Ved at udnytte den relativt korte bølgelængde af 946 nm overgangen i en kvasi-treniveau Nd:YAG laser kan den ønskede bølgelængde på 340 nm nås ved sumfrekvensgenerering med en frekvensfordoblet 532 nm Nd:YAG laser. Men da kvasi-treniveau overgangen medfører et reabsorptionstab og en ti gange reduktion af det stimulerede emissionstværsnit i forhold til fireniveau 1064 nm overgangen, er optimering af en 946 nm laser ikke triviel.

Der er foretaget detaljerede undersøgelser af pumpestrålens egenskaber til en endepumpet 946 nm CW laser. Ved at benytte en innovativ ekstern kavitets taperet diodelaser som pumpekilde, er der opnået 800 mW udgangseffekt med en enkelt emitter pumpekilde, hvilket er en rekord. Indflydelsen af de rumlige og spektrale egenskaber af pumpekilden er blevet undersøgt hver for sig og det blev konkluderet at en bredspektret taperet diode pumpekilde vil være både mest stabil og kosteffektiv.

Q-switchede lasere undersøges med henblik på at generere laserpulser med høj spidseffekt. I særdeleshed er der opnået synkroniseret *Q-switching* mellem en 946 nm og en 1064 nm Nd:YAG laser ved hjælp af en passiv metode. Det er første gang stabil, passiv synkronisering mellem en kvasi-treniveau og en fireniveau laser er opnået over et stort interval af pumpeeffekter. Den mindste forsinkelse mellem de to pulser var 64 ns, hvilket gav 79% tidsligt overlap. Den mindste *jitter* mellem de to laserpulser var på 9 ns. Dette er sammenligneligt med tidligere publicerede resultater for et aktivt synkroniseret system.

En detaljeret undersøgelse viser at den nedre grænse for den relative *jitter* er 6 ns. Denne grænse er bestemt af fluktuationer i pumpeeffekten og den forstærkede spontane emission. Konklusionen er således at den foreslåede passive metode kun er 3 ns dårligere end det optimale.

Endelig er der præsenteret praktiske anvendelser af kompakte halvleder- og faststoflasere i det blå og ultraviolette bølgelængdeområde. En CW taperet diodelaser, frekvensfordoblet til 404 nm i en ekstern kavitet, er blevet brugt i et dyreforsøg til bestemmelse af koncentrationen af *photosensitizer* ved hjælp af fluorescensafbildning. Desuden er en frekvens tredoblet 355 nm *Q-switched* faststoflaser anvendt i en præliminær klinisk undersøgelse af autofluorescens diagnostik af hudkræft. Selvom de prælimenære resultater er lovende, vil systemet med fordel kunne benytte en 340 nm lyskilde, som passer med absorptionstoppene i de endogene fluoroforer. Det billeddannende system vil med fordel kunne benytte en lyskilde med høj spidseffekt, da dette forbedrer signal-støj forholdet.

De kliniske resultater viser at der er et klart behov for en 340 nm pulset laser med høj spidseffekt til autofluorescens målinger. De nuværende resultater med passivt synkroniseret *Q-switching* er meget lovende til 340 nm sumfrekvensgenerering. Teknikken kan udvides til andre bølgelængder, specielt i det blå og ultraviolette spektralområde. En ny generation af pulsede blå og ultraviolette lasere med høj spidseffekt kan realiseres ved at benytte de præsenterede teknikker til passiv synkronisering og optimering af kvasi treniveau lasere.

(Translation by Ole Bjarlin Jensen and Christian Pedersen)

Preface

The work reported here was carried out on the Risø campus of DTU Fotonik in Roskilde, Denmark, between January, 2008 and November, 2010. It was partially supported by the European Union FP-6 project WWW.BRIGHTER.EU, contract no. IST-2005-035266. The tapered diode amplifiers used to pump the quasi-three-level laser was provided by Ferdinand-Braun-Institut, Leibniz Institut für Höchstfrequenztechnik.

I performed the experimental work involving the quasi-three-level laser. This includes the continuous wave (CW) laser, the single Q-switched laser, and the synchronized Q-switching experiments. I also carried out numerical modeling on the CW laser and on the single quasi-three-level Q-switched laser. Numerical modeling of the synchronized system, however, was performed by Prof. Peter Tidemand-Lichtenberg, while I assisted in the qualitative fitting.

I also spent one year at DTU Fysik, where Prof. Tidemand-Lichtenberg provided access to many of the specialized equipment and optical components needed for the experiments. Prof. Tidemand-Lichtenberg has since joined DTU Fotonik at Risø, where I continued to work under joint guidance from my supervisors and from Prof. Tidemand-Lichtenberg.

In terms of the clinical experiments, the 404 nm laser, directly frequency-doubled from an 808 nm tapered diode laser, was built by Jesper Holm Lundeman. My role was to assist in the transportation, alignment, and operation of the laser during the animal measurements, which took place at Biolitec AG in Jena, Germany. I also assisted in the manuscript preparation.

For the autofluorescence clinical experiments, I was involved with the assembly and optimization of the 355 nm laser excitation source. Two PhD students from Lund University – Pontus Svenmarker and Haiyan Xie, together with myself, integrated the laser with the imaging system, and collected data from patients. I contributed to post-processing of the images, and submitted a conference contribution based on the preliminary results.

For the unidirectional ring laser based on differential loss induced by sum-frequency mixing, I assisted in some of the experimental work and manuscript preparation.

This page intentionally left blank.

Table of Contents

This page intentionally left blank.

List of Symbols and Abbreviations

BAL	broad area diode laser
Cr:YAG	chromium-doped yttrium aluminum garnet
CW	continuous wave
ECDL	external cavity tapered diode laser
FWHM	full width half maximum
SDWL	simultaneous dual-wavelength laser
Nd:YAG	neodymium-doped yttrium aluminum garnet
SA	saturable absorber
SFG	sum-frequency generation

c	speed of light in vacuum [m s^{-1}]
h	Planck's constant [J s]
n	refractive index
I	intensity [W m^{-2}]
l_{cav}	optical length of laser cavity [m]
l_{xtal}	physical length of laser crystal [m]
M^2	beam quality
N	population density [m^{-3}]
S	total number of photons in a cavity
z	propagation distance along the optic axis [m]
α	absorption coefficient [m^{-1}]
δ	losses (related to laser cavities)
ΔN	population inversion density [m^{-3}]
ε	fraction of spontaneously emitted photons that contribute to the laser mode
ϕ	photon flux density [m^{-3} s^{-1}]
η_Q	quantum efficiency
λ	wavelength [m]
ν	optical frequency [Hz]
σ	(absorption or stimulated emission) cross-section [m^2]
τ	lifetimes (usually related to fluorescence or cavity decay) [s^{-1}]
w	beam radius [m]
w_0	beam waist radius [m]

Glossary

Autofluorescene – the fluorescence that is generated by endogenous fluorophores that are naturally found inside the body. One such fluorophores thought to be responsible for autofluorescence is nicotinamide adenine dinucleotide (NADH), which has an absorption peak at around 340 nm.

Beam quality – it is generally understood as proportional to the product of the beam waist of a laser beam, and its divergence angle in the far field. In more precise terms, it is the M^2 variable in the following equation:

$$w(z)^2 = w_0^2 + \left(\frac{M^2 \lambda}{\pi w_0} \right)^2 z^2$$

where $w(z)$ is the beam radius at a certain distance, z, from the beam waist. w_0 is the beam waist radius, and λ is the wavelength. Thus, for a perfect Gaussian beam, $M^2 = 1$, and it is known as diffraction-limited.

The definition of beam radius is important here. According to ISO standards 11146, second-moment beam widths should be used for the fitting of M^2. For beams with a Gaussian transverse profile, the second-moment beam width is the same as the width where the intensity profile has fallen to $1/e^2$ of the intensity in the center of the beam. Thus, it would be appropriate to use the $1/e^2$ beam width only in this case. It may be interesting to note that the "2" in M^2 in fact stands for second-moment in the definition of beam quality.

Broad-stripe diode/ broad area diode – a semiconductor laser with an active area with dimensions on the order of ~100 μm x 1 μm x 2 mm. The height (fast-axis direction) of the active region is thin to allow single mode guiding, while the width (slow-axis direction) is relatively wide, which provides high gain, but also permits multiple transverse modes to oscillate. Output power of a broad-area diode laser is higher than a single-mode diode, but its beam quality is significantly worse along the slow-axis direction.

External cavity laser – a semiconductor laser using external frequency-selective components for gain feedback (e.g. gratings or mirrors), as opposed to high-reflection coatings deposited on the end facets of the semiconductor amplifier.

Fast axis – the axis (or direction) perpendicular to the plane of the p-n junction of a semiconductor diode emitter. Due to the relatively short emitter length along this direction, typically ~1 μm, the beam divergence along the fast axis is relatively high (hence the name "fast" axis.) Typically, only one transverse mode is guided in this direction, and as a result, the beam quality is typically close to 1 in the fast axis.

Fluorescence imaging – the variety of imaging methods that record fluorescence emissions produced by fluorophores, which can be found naturally inside the body or be introduced with an external substance. By observing the differences in fluorescence intensities (and wavelength), information can be extracted about the biological tissue under investigation. It is also possible to record the fluorescence spectrum at each pixel across a wide-field image to perform multispectral fluorescence imaging. More exotic analysis can be done using the characteristic decay lifetime of the fluorescence signal as the contrasting parameter for imaging, which is known as fluorescence lifetime imaging (FLIM). A pair of donor-acceptor fluorophores could also be used to sense changes in the molecular bond in biological samples using Förster resonance energy transfer (FRET).

Fluorophore – molecules that emit red-shifted fluorescence when excited by a shorter wavelength light source. These molecules can be found naturally in our bodies (endogenous fluorophores), or be introduced with an external substance (exogenous fluorophores). Exogenous fluorophores can be introduced topically, intravenously, orally, or injected directly into the tissue.

M^2 – see "beam quality."

Photosensitizer – in photodynamic therapy of cancer, it is the substance that is activated by light and initiates the photochemical reaction that kills the cancer cells. For example, aminolevulinic acid (5-ALA) initiates the protoporphyrin IX (PpIX) synthesis pathway, which produces singlet oxygen that causes cell death. PpIX is itself fluorescent and has emission peaks between 600 – 700 nm, while 5-ALA has an absorption peak near 405 nm.

Quasi-three-level laser – as opposed to the common four-level laser systems, the lower laser level of a quasi-three-level laser is in the ground state manifold. This means that the lower laser level is thermally populated even when the laser crystal is not pumped. The un-pumped population in the

lower laser level can be determined with Boltzmann statistics, as discussed in section 2.2 of this thesis.

Rate equations – a set of coupled equations that describe the temporal dynamics of the laser. Specifically, these are partial differential equations in time that describe the photon flux and population inversion density. In passively Q-switched lasers, these also include the saturable absorber's population densities at the relevant energy levels.

Relative timing jitter – in the context of synchronized Q-switching, it is defined as the variation in timing between the two synchronized pulse trains, i.e. the variation in the amount of delay between two synchronized pulses. Following conventions by laser manufacturers and prior art, this is defined as one standard deviation of the delay measurements.

Second-moment beam width – the second-moment beam width is calculated from a weighted average of the transverse intensity profile. To be precise, the width is weighted by the intensity at the corresponding transverse position:

$$w_x = 2\sigma = 2\sqrt{\frac{\int (x - x_0)^2 I(x,y)dxdy}{\int I(x,y)dxdy}}$$

where w_x is the beam radius in the dx direction, x-x_0 is the distance from the centroid of the transverse profile, $I(x,y)$ is the transverse intensity distribution, and σ can be seen as the standard deviation of the transverse photon distribution. For a Gaussian-shaped transverse profile, the second-moment beam width is the same as the $1/e^2$ beam width – for high order beams however, the second-moment method should be used, according to ISO 11146.

Slow axis – the axis (or direction) in the plane of the p-n junction. For broad area diode lasers (BAL's) and tapered diode lasers, this is along the wide dimension of the emitter. Due to the relatively wide emitter dimension along this direction, the beam divergence along the slow axis is relatively low (hence the name "slow" axis.) For the same reason, multiple modes are guided in BAL's and tapered diode lasers, and the beam quality is typically bad in the slow axis.

Tapered diode laser – a semiconductor laser with two active structures: a single-mode (ridge) region and a tapered region that diverges outwards following natural diffraction of the beam. The design is a compromise to maintain the good beam quality of a single-mode diode, while increasing the output power towards those of a broad-strip diode.

Timing jitter – in the context of Q-switched laser pulse trains, this is the variation in the time separation from pulse to pulse, i.e. variation in the pulse-to-pulse period. Following conventions by laser manufacturers and prior art, this is defined as one standard deviation of the pulse-to-pulse period. In the context of synchronized Q-switching, the term relative timing jitter is used. (See "Relative timing jitter").

Acknowledgements

The work presented here would not have been possible without the kind support of the people who surround me. I would first like to thank my main supervisor, Christian Pedersen, for his guidance on the PhD project, valuable input for preparing the publications, and for always keeping his door open. I would also like to express my gratitude to Ole Bjarlin Jensen, who is always available to discuss work and personal issues alike. I have enjoyed our many interesting conversations, and his breadth of knowledge and experience in the lab is invaluable to my PhD. I also owe thanks to Peter Eskil Andersen for his frank and honest advice on the work as well as on my career, and to Paul Michael Petersen for his kind encouragement and confidence in my work.

I would like to give a special thanks to Peter Tidemand-Lichtenberg for his help, guidance, and collaboration on many of the experiments presented here, as well as for providing access to his lab space and equipment. I enjoyed learning many interesting subtleties about solid-state lasers from him.

At DTU Fysik, I thank Mikael Østergaard Lassen, Alexander Huck, and Anders Tipsmark for sharing their equipment, offices, and occasionally a laugh to make the day go by quickly.

To Stefan Andersson-Engels, Katarina Svanberg, and Niels Bendsoe at Lund University, thank you for your enthusiastic support, advice, and organization for the fluorescence imaging measurements. I also want to thank the PhD students at Lund University – Pontus Svenmarker, Haiyan Xie, Johan Axelsson, and Jesper Holm Lundeman. It had been a pleasure working with you, and I enjoyed your professionalism very much. Thank you for taking the time to introduce me to fluorescence imaging, for your patience with my endless questions, and for your help in preparing the corresponding manuscripts. We had some long working days together, but you made them enjoyable.

Thanks also to André Müller and Sebastian Marschall for insightful discussions on the tapered diode lasers and lasers in general, and to Deepak Vijayakumar for being a great office mate who can always share a laugh when I need it. To Martin Thalbitzer Andersen, thank you for your guidance and valuable advice early on in my PhD program. It had always been a

pleasure talking to you about physics, and other subjects. To Pernille Klarskov Pedersen, thank you for your help in proof-reading and preparing this thesis.

I would also like to thank Nina Bendix and Charlotte Melgaard Larsen for helping me sort out the day-to-day administrative issues. From ordering components, to registering my sick days, to helping get this thesis printed, you have made life easier at Risø.

To Peter Jensen at Risø and Søren Hjort at DTU Fysik, thank you for your help in assembling and fabricating mechanical and electronic components that are often needed in such short notice. I especially want to thank Peter Jensen for teaching me to use the lathe and milling machine, and entertaining conversations during coffee breaks.

Last but not least, I would like to thank my friends in Copenhagen who have made my stay here very memorable, and then to help forget some when the going gets tough. I could not have done it without you guys. I set aside my deepest thanks to my family – my parents and brother – for the sacrifice they made, for their endless and unconditional support, and for encouraging me to pursue what I love.

This page intentionally left blank.

TO MY PARENTS,

KWONG PUI LAN AND CHENG TAI HONG

1. Introduction

Laser induced fluorescence (LIF) is a promising diagnostic tool that could detect cancerous tissue non-invasively, economically and in real-time. By observing the differences in the fluorescence spectra and intensities between the tumor site and normal tissue, information regarding differences in biological composition could be extracted. LIF has found particular use in monitoring treatment progress during photodynamic therapy (PDT), where exogenous photosensitizers used for the treatment would also produce fluorescence. However, using exogenous fluorophores generally require time for drug uptake, and the patients would need to avoid light exposure before and after the measurement.

By taking advantage of endogenous fluorophores, autofluorescence imaging is an alternative that require no prior preparations on the patient and could serve as a useful screening tool. It requires excitation light sources in the UV spectrum, and preferably a high peak-power, pulsed light source which would increase the signal-to-noise ratio. Unfortunately, such light sources are not readily available using current technologies.

One option is to use a nitrogen laser at 337 nm to excite the absorption peak of nicotinamide adenine dinucleotide (NADH), an endogenous fluorophore thought to be responsible for autofluorescence when imaging skin lesions. However, these light sources are bulky, require special high-voltage power supplies, and periodic refill of the nitrogen cartridge.

Another option is to perhaps use UV diode lasers (e.g. PicoQuant LDH-P series). These light sources are cheap, compact, and efficient, but they tend to have a low upper state lifetime and suffer from catastrophic optical damage at high intensities. Q-switched operation is therefore not practical using diode lasers.

Diode-pumped solid-state (DPSS) lasers, on the other hand, have been widely adopted. Both frequency-doubled green lasers, and frequency tripled, and even quadrupled lasers in the blue and UV spectral region have been reported and are commercially available [1-5]. However, since these are limited to wavelengths at multiples of the fundamentals, the spectral availability is fairly limited.

In this PhD thesis, we aim to improve the spectral coverage of pulsed blue and UV DPSS lasers in a passive approach by a combination of three methodologies:

1. To take advantage of the shorter wavelengths associated with quasi-three-level lasers and therefore, expand the coverage into the blue and UV spectral region.
2. To expand the spectral coverage by considering sum-frequency generation, as opposed to relying solely on the degenerate case of frequency-doubling, tripling, etc.
3. To perform the above in passively Q-switched lasers to obtain high peak powers, and efficient non-linear conversion.

By performing the above using a passive approach, bulky and expensive electronic components could be avoided, thereby reducing complexity and cost, and increasing reliability of the laser. One drawback of using passive optical components, however, is reduced stability due to thermal noise and mechanical vibration. This is understandably an important performance metric and was also investigated as part of the PhD work.

Since all of the above three points require efficient operation and application of a quasi-three-level laser, the PhD work can be divided into the following four areas:

A. Continuous-wave (CW) operation of quasi-three-level lasers – **Chapter 2**
B. Passively Q-switched operation of quasi-three-level lasers – **Chapter 3**
C. Passively synchronized Q-switching between a quasi-three-level and a four-level laser – **Chapters 4 and 5**
D. Several applications involving novel solid-state lasers and fluorescence imaging are presented to showcase the possibilities and the potential of future work. – **Chapter 6**

The body of the PhD thesis will therefore be divided into chapters according to the four areas identified. The main contribution of this PhD project is in areas A, C and D; however, optimization and design of quasi-three-level Q-switched lasers is included in Chapter 3 for completeness and serve as a background to Chapters 4 and 5. Within each area, the basic theory, working principles, state of the art, and critical assessment of related work will be

presented in the introduction of the corresponding chapter. The sub-sections that follow will then describe the contributions made during the PhD. A short summary at the end of each chapter puts the work into context of the current state of the art, and provides outlook for future work.

While the results presented in this thesis are from the perspective of 340 nm generation, the approach described herein can be equally applied to other laser transitions and can be used as a generic approach to building pulsed blue and UV lasers at other wavelengths. This argument will be further discussed in Chapter 4.

1.1 General Background

In the particular example of autofluorescence imaging, the aim of the PhD project is to build a pulsed, 340 nm light source. The specific approach to reaching this goal is through a cascaded non-linear process, illustrated in Figure 1.1 below.

Figure 1.1 - Intended nonlinear interactions for reaching 340 nm – based on non-linear frequency mixing between a four-level and a quasi-three-level Nd:YAG laser.

The setup would require a frequency-doubled four-level Nd:YAG laser and a quasi-three-level Nd:YAG laser to overlap both temporally and spatially. In the non-depleted regime, the converted power from a non-linear process is dependent on the product of the powers of the fundamental wavelengths; thus, high powers in the fundamental lasers are important for efficient conversion:

$$P_{SFG} = \eta_{NL} P_{532} P_{946}$$

where η_{NL} is a constant relating to the wavelengths of the three electromagnetic waves, the phase mismatch between the three waves, the mode sizes, Planck's constant, the impedance of free-space, the length of the non-linear medium and its non-linear coefficient [6]. To achieve the high instantaneous powers needed for efficient conversion, Q-switched lasers or intracavity conversion using continuous-wave (CW) lasers could be used. Thus, optimization of the quasi-three-level laser under these operating regimes will be investigated.

As a brief introduction to the subject, basic descriptions of quasi-three-level lasers and tapered diode lasers – which are particularly suitable for pumping quasi-three-level systems – are described in sections 1.1.1 and 1.1.2 respectively.

1.1.1 Quasi-three-level laser

Figure 1.2 shows the energy level diagram of neodymium-doped yttrium aluminum garnet (Nd:YAG). In diode-pumped Nd:YAG lasers, the atoms are optically pumped from the ground state manifold ($^4I_{9/2}$) to the pump bands. From there they quickly relax to the long lifetime $^4F_{3/2}$ energy bands ($\tau = 230$ μs). The common-four level transitions at ~1.06 μm then take place between the $^4F_{3/2}$ and $^4I_{11/2}$ energy bands, whereas the quasi-three-level transitions at ~0.9 μm take place between the $^4F_{3/2}$ and $^4I_{9/2}$ energy bands.

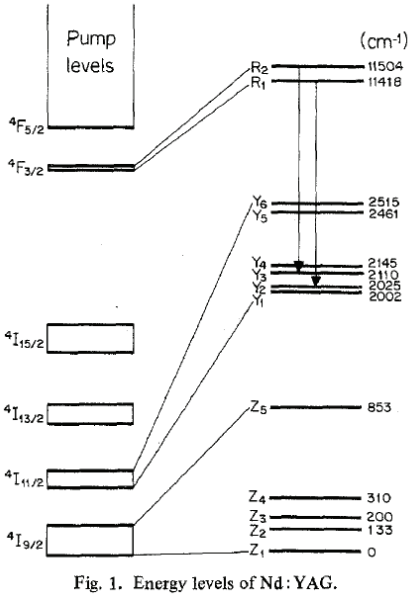

Fig. 1. Energy levels of Nd:YAG.

Figure 1.2 - Energy level diagram of Nd:YAG. Source: Aull et al. [7].

Unlike the more common four-level laser systems, a quasi-three-level laser has its lower laser energy level lying inside the ground state manifold. At 946 nm, for example, the emission transition is from the R_1 Stark energy level to the Z_5 Stark energy level. Therefore, the lower laser level in a quasi-three-level system is thermally populated and causes absorption of photons at the laser wavelength, introducing additional losses in the laser. This is more commonly referred to as reabsorption loss.

Since reabsorption of the laser photons would induce significant losses wherever the pump intensity is not sufficient to depopulate the ground state-manifold, optimization of quasi-three-level lasers is non-trivial. In particular, the pump beam should have a good spatial overlap with the cavity mode

inside the laser crystal, while a high pump-photon density is needed to depopulate the lower laser level and create a high population inversion for efficient lasing. On the other hand, diffraction of the pump and cavity beams prevents small beam sizes to be maintained throughout the length of the laser crystal. Thus, a high beam-quality pump source is particularly important for efficient lasing. Fortunately, recent innovations in diode pump sources have made significant headway in improving pump beam beam quality without sacrificing its power. One such example is the tapered gain geometry in diode lasers, where the shape of the active material follows the far-field diffraction of a fundamental Gaussian mode. This special tapered design is one of the enabling technologies that make the current PhD work possible, and a brief introduction on tapered diode lasers will be described in section 1.1.2. The optimization of the pump and cavity beam size, and the rate equations for quasi-three-level lasers will be discussed in detail in sections 2.1 and 2.2 respectively.

1.1.2 Tapered diode laser

Tapered diode lasers offer improved spatial properties in its output beam over traditional broad area diode lasers (BAL) without sacrificing its compactness, wavelength tunability, and gain. It usually consists of a tapered gain section that follows the diffraction of the beam, and a single-mode ridge section that is useful for wavelength and transverse mode selectivity. Figure 1.3 shows an example of a tapered amplifier.

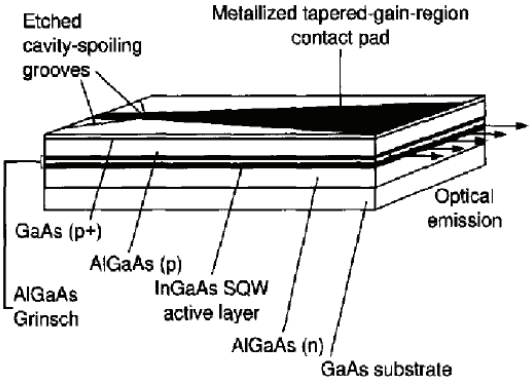

Figure 1.3 - Illustration of a tapered amplifier with a graded index, separate confinement heterostructure (GRINSCH) active region. Source: J. N. Walpole [8].

In early works, most tapered diodes were used as the amplifier stage in master oscillator power amplifiers (MOPA's) [9,10]. In fact, the amplifier illustrated in Figure 1.3 was used as the amplifier to a Ti:sapphire master oscillator to investigate the performance of the tapered diode [10], and a small input aperture (~10 μm) is shown instead of a ridge gain region. The cavity spoiling grooves were etched in place to suppress parasitic oscillations due to back reflections from the end facets. The direction along the wide dimension of the output aperture, parallel to the quantum well plane, is referred to as the slow axis direction, while the direction perpendicular to the quantum well plane is known as the fast axis direction.

Improvement of beam quality in tapered diodes result from the input beam being amplified as it diffracts naturally. Thus, the input beam divergence (or beam waist) should be chosen to match closely with the tapered angle of the gain geometry. If the input beam diverges slower than the gain geometry, there would be unused gain and the overall efficiency is lowered. If the input beam diverges faster than the gain geometry, only the central part of the beam would be amplified and the output profile would be non-uniform. In

practice, if a fundamental Gaussian mode is coupled into the amplifier, the central part of the gain structure saturates first due to the higher optical intensity in the center, while the outer portion of the beam experiences a higher gain. As a result, the output profile should be a relatively uniform top-hat distribution, assuming negligible filamentation effects [8].

Along the longitudinal direction, astigmatism between the fast and slow axis is present. In the fast axis, the source is at the output facet. However, in the slow axis, a virtual image of the source is located at a distance L/n_g behind the output facet, where L is the length of the tapered section, and n_g is the refractive index. In Figure 1.4, the side view shows the divergence of the source in the fast axis, while the top view shows the divergence in the slow axis. The astigmatism could be corrected by using cylindrical lenses to collimate the two axes independently. In practice, however, thermal lensing causes the degree of astigmatism to change with pump current; thus, in the experiments, the diode was always pumped at maximum current and the combination of a half-wave plate and polarizer was used to attenuate the beam when necessary.

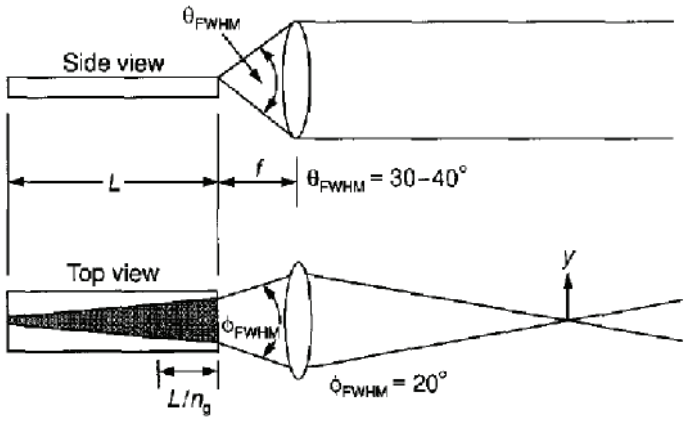

Figure 1.4 - Illustration showing the astigmatic nature of the output beam from a tapered diode amplifier. Source: J. N. Walpole [8].

Another advantage of the tapered design is that, as the beam and gain structure diverges, the gain saturation parameter, P_{sat}, actually increases with increased amplifier length [8]:

$$P_{sat} = 2\phi r I_{sat} \tag{1.1}$$

where ϕ is the angle away from the center of the beam, r is the distance from the input aperture (i.e. amplifier length) and I_{sat} is the saturation power density and is constant.

Figure 1.5 shows the quantum efficiency of the tapered amplifier as a function of amplifier length. Near the input facet, the efficiency drops rapidly due to a relatively low photon density and a poor overlap between the slowly diverging beam and the gain geometry [8,11]. The efficiency increases to a maximum as the photon density increases, but drops off again as it is offset by the increase in current. In principle, the output power in a long amplifier still increases linearly with amplifier length; however, as the total current is increasing quadratically with amplifier length, the overall efficiency decreases [8].

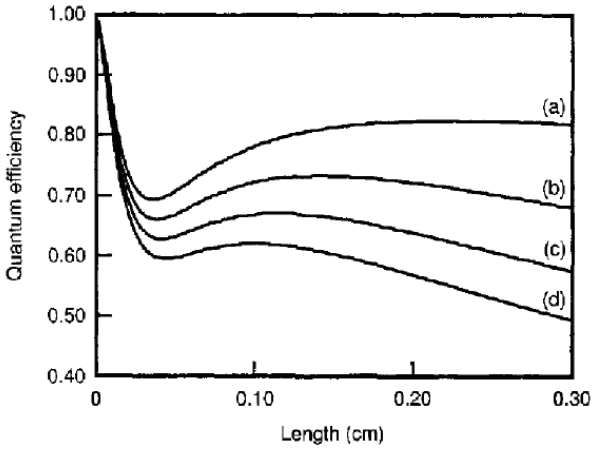

Figure 1.5 - Quantum efficiency of a tapered amplifier as a function of amplifier length. The different curves (a)-(d) are plots for different loss values. Source: J. N. Walpole [8].

Similar to BALs, as the photon density increases with pump current and amplifier length, filamentation becomes significant and causes degradation in the beam's spatial profile. Thus, the tapered amplifier length is usually on the order of millimeters.

1.2 List of Publications

Peer-Reviewed Journals:

1. H. P. H. Cheng, P. Tidemand-Lichtenberg, O. B. Jensen, P. E. Andersen, P. M. Petersen, and C. Pedersen, "Experimental investigation of relative timing jitter in passively synchronized Q-switched lasers," Optics Letters **36**, 415-417 (2011).

2. H. P. H. Cheng, P. Tidemand-Lichtenberg, O. B. Jensen, P. E. Andersen, P. M. Petersen, and C. Pedersen, "All passive synchronized Q-switching of a quasi-three-level and a four-level Nd:YAG laser," Optics Express **18**, 23987-23993 (2010).

3. H. P. H. Cheng, O. B. Jensen, P. Tidemand-Lichtenberg, P. E. Andersen, P. M. Petersen, B. Sumpf, G. Erbert, and C. Pedersen, "Efficient quasi-three-level Nd:YAG laser at 946 nm pumped by a tunable external cavity tapered diode laser," Optics Communications **283**, 4717-4721 (2010).

4. P. Tidemand-Lichtenberg, H. P. H. Cheng, and C. Pedersen, "Unidirectional ring-laser operation using sum-frequency mixing," Optics Letters **35**, 2567-2569 (2010).

5. H. Xie, H. Liu, P. Svenmarker, J. Axelsson, C. T. Xu, S. Gräfe, J. H. Lundeman, H. P. H. Cheng, S. Svanberg, N. Bendsoe, P. E. Andersen, K. Svanberg, and S. Andersson-Engels, "Drug quantification in turbid media by fluorescence imaging combined with light-absorption correction using White Monte Carlo Simulations," Journal of Biomedical Optics (under review).

International Conferences:

6. H. P. H. Cheng, P. Tidemand-Lichtenberg, O. B. Jensen, P. E. Andersen, P. M. Petersen, and C. Pedersen, "All passive synchronization of a quasi-three-level Q-switched laser and a four-level Q-switched laser," in *Proceedings of SPIE Photonics West 2011*, paper 7912-33. (Oral)

7. H. Xie, H. Liu, P. Svenmarker, J. Axelsson, S. Gräfe, J. H. Lundeman, H. Cheng, M. Kyriazi, N. Bendsoe, P. Andersen, K. Svanberg, and S. A. Engels, "Accurate Study of FosPeg® Distribution in a Mouse Model Using Fluorescence Imaging Technique and Fluorescence White Monte Carlo Simulations," in *Biomedical Optics*, OSA Technical Digest (CD) (Optical Society of America, 2010), paper BTuD6. (Poster)

8. H. P. H. Cheng, P. Svenmarker, H. Xie, P. Tidemand-Lichtenberg, O. B. Jensen, N. Bendsoe, K. Svanberg, P. M. Petersen, C. Pedersen, S. Andersson-Engels, and P. E. Andersen, "Autofluorescence of pigmented skin lesions using a pulsed UV laser with synchronized detection: clinical results," in *Proceedings of SPIE Photonics Europe 2010*, vol. 7715. (Oral)

9. P. Tidemand-Lichtenberg, H. P. Cheng, and C. Pedersen, "$\chi^{(2)}$ Induced Non-Reciprocal Loss and/or Phase Shift for Unidirectional Operation of Ring Lasers," in *Advanced Solid-State Photonics*, OSA Technical Digest Series (CD) (Optical Society of America, 2010), paper ATuA19. (Poster)

10. H. P. H. Cheng, O. B. Jensen, P. M. Petersen, P. E. Andersen, P. Tidemand-Lichtenberg, and C. Pedersen, "Tapered diode laser pumped 946 nm Nd:YAG laser," in *European Conference on Lasers and Electro-Optics 2009 and the European Quantum Electronics Conference. CLEO Europe - EQEC 2009,* paper CA12_5. (Oral)

11. P. Tidemand-Lichtenberg, C. Pedersen, H. P. Cheng, P. M. Petersen, and P. Buchhave, "Pulsed UV-Light Source for Auto-Fluorescence Diagnostics," in *Frontiers in Optics*, OSA Technical Digest (CD) (Optical Society of America, 2008), paper FTuX3. (Oral)

Summer School Posters:

12. H. P. H. Cheng, P. Tidemand-Lichtenberg, O. B. Jensen, P. E. Andersen, P. M. Petersen, and C. Pedersen, "Pulsed UV Light Source for Autofluorescence Diagnostics," in iNano PhD Summer School 2010: Nano-optics (2010).

13. H. P. H. Cheng, P. Tidemand-Lichtenberg, O. B. Jensen, P. E. Andersen, P. M. Petersen, and C. Pedersen, "External cavity tapered diode pumped laser to generate pulsed UV light for autofluorescence diagnostics," in 4th International Graduate Summer School: Biophotonics '09 (2009).

14. H. P. H. Cheng, O. B. Jensen, P. E. Andersen, P. M. Petersen, and C. Pedersen, "Pulsed UV Laser for Fluorescence Diagnostics based on Non-Linear Frequency Conversion," in Quantum and Nonlinear Optics PhD Summer School (2008).

2. Continuous Wave Operation

The vision of the current PhD work is to produce a pulsed UV laser for autofluorescence imaging – specifically, by taking advantage of the shorter wavelength quasi-three-level lasers. However, quasi-three-level transitions suffer from significant reabsorption loss at the laser wavelength, and reduced stimulated emission cross-sections when compared to four-level transitions. Thus, optimization of quasi-three-level lasers is non-trivial and it is worthwhile to study such lasers under CW operation prior to attempts on a pulsed system.

In this chapter, numerical modeling and experimental investigation into the performance of an Nd:YAG quasi-three-level laser at 946 nm is presented. In particular, an external cavity tapered diode laser (ECDL) was used to probe how the pump source spectral and spatial properties separately affect laser performance. The background and state of the art on diode end-pumped quasi-three-level lasers are presented in section 2.1; the quasi-three-level rate equations are described in section 2.2; the experimental setup is described in section 2.3; the experimental results are discussed in section 2.4, and a brief summary and outlook is presented in section 2.5.

2.1 Background

Traditionally, broad area diode lasers (BAL) have been used as pump sources for solid-state lasers, providing high efficiency, wavelength tunability and compactness. But these pump sources generally suffer from poor beam quality and a relatively broad spectrum, the effects of which are particularly pronounce when working with quasi-three-level lasers, resulting in increased thresholds and reduced slope efficiencies. By establishing the laser rate-equations for quasi-three-level systems (which will be described in the next section), Fan and Byer established the condition for optimizing the lasing threshold in quasi-three-level lasers [12]. In particular, the threshold in terms of absorbed pump power is:

$$P_{th} = \frac{\pi h \nu_p}{4 f \sigma \tau}\left(w_c^{\,2} + w_p^{\,2}\right)\left[\delta \frac{n l_{xtal}}{l_{cav}} + 2\alpha_{reab} l_{xtal}\right]; \quad \alpha_{reab} = \sigma \Delta N^0 \quad (2.1)$$

where ν_p is the pump source frequency, f is the fraction of atoms that are in the laser energy levels according to Boltzman distribution and will be described in more details in the next section, σ is the stimulated emission cross-section, τ is the fluorescence lifetime, w_c and w_p are the cavity mode and pump beam waist radius respectively, δ is the roundtrip passive loss of the cavity, n is the refractive index of the gain medium, l_{cav} is the optical path length of the cavity, and l_{xtal} is the physical length of the gain medium. α_{reab} can be seen as the loss coefficient associated with the reabsorption loss, where ΔN^0 is the population inversion in the laser crystal when it is not being pumped. It can be approximated as the population in the lower laser level (populated thermally in a quasi-three-level system), when the crystal is not pumped.

The most interesting term in equation (2.1) is $(w_c^2 + w_p^2)$, where it is clear that the threshold is proportional to the square of both the cavity and pump beam waist radius; thus, in theory, one would prefer the smallest cavity and pump mode sizes possible to achieve a low lasing threshold. In practice, this is limited by diffraction, and optimization of the mode sizes will be further discussed later in this section.

In terms of the slope efficiency, Fan and Byer showed that the reabsorption loss simply acts an extra saturable loss term in the steady-state solution of the output power. Thus, the slope efficiency of a quasi-three-level laser is

proportional to $T/(\delta+\delta_s)$, as opposed to T/δ in four-level systems [13]. T denotes the output coupling, and δ_s is a saturable loss associated with reabsorption at the laser wavelength [12]:

$$\delta_s = -\sigma \Delta N^0 l_{xtal} \frac{I_{sat}}{I} \ln\left(1+\frac{2I}{I_{sat}}\right) \tag{2.2}$$

where I is the circulating intensity, I_{sat} is a constant relating to the laser wavelength, f, σ, τ, n, l_{cav} and l_{xtal}.[1] When the laser is below threshold ($2I/I_{sat} << 1$), the reabsorption loss is approximated to $\delta_s \approx 2\sigma\Delta N^0 l_{xtal}$, which is in agreement with equation (2.1). When the laser is far above threshold, $\delta >> \delta_s$, and the slope efficiency approaches that of four-level systems.

Risk elaborated further on Fan and Byer's work, and found that, in the presence of reabsorption, there exists an optimal ratio of the pump and cavity beam radii, w_p/w_c, that gives the maximum slope efficiency for a particular pump power level [14]. This ratio depends on the circulating field inside the cavity, and is ≤ 1. This is expected: if the pump mode is larger than the cavity mode, the pump photons that are absorbed outside the cavity mode is simply wasted, and therefore the efficiency decreases. However, Risk noted that the output power is more influenced by a low threshold than it is by a high slope efficiency, leading to the conclusion that w_p/w_c should also tend to zero for optimizing output power of a quasi-three-level laser.

To arrive at these elegant results, Risk, Fan and Byer excluded diffraction effects of the Gaussian pump and cavity beams from their numerical models. This may be a valid approximation for pump sources with good beam quality and high absorption, such as dye lasers and single-mode diodes. For broad area diode lasers and diode arrays, equation (2.1) breaks down, and the requirement for $w_p \rightarrow 0$ no longer holds.

Lindsay and Ebrahimzadeh examined the effect of diffraction using an average beam radius that is calculated over the laser crystal length [15]:

[1] Fan and Byer assumed a monolithic cavity in [12] where the laser crystal length is the same as the cavity length. In the case where $l_{cav} \neq l_{xtal}$, the definition of I_{sat} should be modified to: $I_{sat} = (h\nu_c/f\sigma\tau)(nl_{xtal}/l_{cav})$. However, the results on the effect of reabsorption loss on the slope efficiency remains the same.

$$\bar{\omega}^2 = w_0^2 + \frac{1}{3}\left(\frac{M^2 \lambda l_{xtal}}{\pi n w_0}\right)^2 \tag{2.3}$$

where $\bar{\omega}$ is the averaged beam radius, w_0 is the actual beam waist radius, n is the refractive index of the gain medium, and M^2 is the beam quality.

From (2.3), the optimal actual beam waist that would give the minimum average beam radius is:

$$w_{0,opt} = \left(\frac{1}{\sqrt{3}}\frac{M^2 \lambda l_{xtal}}{\pi n}\right)^{1/2} \tag{2.4}$$

Using these relations, Lindsay and Ebrahimzadeh suggested that a quasi-three-level laser could be optimized by first determining the optimal pump beam waist radius using the pump source's beam quality, wavelength, and the laser crystal length. In effect, the pump beam waist radius would then be optimized for low lasing threshold. After this, the cavity mode size could be optimized experimentally for the maximum output power. In all of the experiments reported in this thesis, the optimal pump-to-cavity mode size ratio, w_p/w_c, was always found to be close to and slightly less than 1.

2.1.1 Prior Art

Various experimental approaches have been pursued in the literature to obtain efficient lasing at the 946 nm line of Nd:YAG. In the first diode-pumped demonstration of such laser [16], Fan and Byer used a Rhodamine 6G dye-laser to simulate the performance of a diode laser with good beam quality. A slope efficiency of 34% in terms of absorbed pump power was inferred using a 1.3 mm long Nd:YAG crystal. One alternative is to use very thin crystals and multiple passes of the pump light as in the thin disc laser geometry presented in [17], but this is in general more complicated to implement compared to end-pumped systems. Another approach using a pump-resonant cavity to reduce the lasing threshold is presented in [18], but further scaling of the output power may be difficult due to the relatively large optical feedback back into the diode amplifier. With a single stripe 2 W BAL, Hollemann et al. obtained 250 mW of output power in a 3 mm end-pumped Nd:YAG laser [19]. An injection locked broad area diode laser has also been used to improve the spatial and spectral properties of a BAL pump source, resulting in 120 mW of output power at a slope efficiency of 60% in terms of absorbed pump power [15].

Tapered diode lasers that have inherently better spatial and spectral properties are becoming more readily available and are promising pump sources for quasi-three-level systems. Paboeuf et al. [20] used a 798 nm tapered diode laser with volume Bragg grating (VBG) feedback to pump a quasi-three-level Nd:ASL system, achieving a slope efficiency of 34% in terms of absorbed pump power and an output power of 156 mW at 900 nm.

While stacked and arrayed broad area diodes have been used to pump Nd:YAG at the 946 nm transition [21-23], achieving relatively high output powers, it is argued that tapered diodes may be similarly stacked and beam combined in the future [24,25]. Thus, the investigation presented here is concerned only with single-emitter pump sources, and their spatial and spectral properties.

In this work, tunable Littrow grating feedback is used on a tapered diode amplifier to further investigate the importance of the spectral properties of the pump source. A direct experimental comparison between a single emitter external cavity tapered diode laser (ECDL) pumped and a single emitter broad area diode laser (BAL) pumped 946 nm Nd:YAG laser is presented. A slope efficiency of 65% in terms of absorbed pump power is achieved with

the ECDL pump source, resulting in an output power of 800 mW at 946 nm in a pure Gaussian mode, which to the authors' knowledge is the highest achieved with a single emitter diode laser pump source. Good agreement between the experimental results and numerical model [12,14,26] is found, when using a quantum efficiency of 0.85 to account for all non-radiative losses in the upper laser energy level. The improved performance is then investigated in terms of the spatial properties and spectral properties of the pump source, respectively. Based on this, a simple and cost-effective feedback scheme of the tapered diode laser pump source is proposed and demonstrated experimentally.

2.2 Rate Equations for Quasi-Three-Level Lasers

The numerical model used in the following section is a combination of the quasi-three-level laser models described in [12,14,26]. The model includes the quasi-three level nature of the 946 nm Nd:YAG laser line and the non-perfect Gaussian pump beams, described by their M^2 values, as suggested by Auge et al. [26]. In this work, we use the quantum efficiency, η_Q, defined as the number of fluorescent photons produced from the upper manifold divided by the number of absorbed pump photons, to fit the experimental data of section 2.3. The fitted η_Q is then compared to previously published values.

Since the lower laser level is thermally populated in a quasi-three-level laser, it would be useful to determine the fraction of atoms that are in the lower laser level out of the whole population in the lower energy manifold in thermal equilibrium. This can be determined using the Boltzmann distribution [12]:

$$\begin{aligned} N_a &= \frac{g_a N_L}{Z_a} \exp(-E_a / kT) = f_a N_L \\ Z_a &= \sum_i g_i \exp(-E_i / kT) \end{aligned} \tag{2.5}$$

where the summation is over all energy levels in the manifold. kT is the Boltzmann constant and temperature as per usual, while g_i is the degeneracy of energy level i, and E_i is the corresponding energy. N_a is the population in energy level a, and N_L is the total population in the manifold. Thus, f_a is the fraction of atoms in the particular energy level a out of the whole population in the manifold. For the 946 nm transition in Nd:YAG at room temperature, f_a for the lower laser level is 0.0075. Similarly, the upper energy manifold is also Stark-splitted, and the fraction of atoms in the upper laser energy level, f_b, is 0.612.

The rate equations for the upper and lower laser energy levels could then be written [12,14]:

$$\frac{dN_b(r,z)}{dt} = f_b R r_p(r,z) - \frac{N_b(r,z) - N_b^0}{\tau} - \frac{f_b c\sigma(N_b(r,z) - N_a(r,z))}{n} Sr_c(r,z)$$
$$\frac{dN_a(r,z)}{dt} = -f_a R r_p(r,z) - \frac{N_a(r,z) - N_a^0}{\tau} + \frac{f_a c\sigma(N_b(r,z) - N_a(r,z))}{n} Sr_c(r,z) \quad (2.6)$$

where N_a and N_b are the population densities in the lower and upper laser levels respectively, R is the pump rate, τ is the fluorescence lifetime, c is the speed of light in free-space, σ is the stimulated emission cross section, n is the refractive index of the laser crystal at the laser wavelength, and S is the number of 946 nm photons in the cavity. N_a^0 and N_b^0 are the population densities in the lower and upper laser energy levels when the crystal is not pumped. $r_p(r,z)$ and $r_c(r,z)$ are the normalized pump and cavity photon distribution throughout the laser crystal and the laser cavity respectively:

$$r_c(r,z) = \frac{2}{\pi w_c(z)^2} \frac{1}{l_{cav}} e^{\frac{-2r^2}{w_c(z)^2}}; \quad r_p(r,z) = \frac{2}{\pi w_p(z)^2} \frac{\alpha}{1 - e^{-\alpha l_{xtal}}} e^{\frac{-2r^2}{w_p(z)^2}} e^{-\alpha z} \quad (2.7)$$

where α is the absorption coefficient at 808 nm, and l_{cav} and l_{xtal} are the cavity and laser crystal length respectively. $w_p(z)$ and $w_c(z)$ are the beam radii of the pump and cavity mode respectively as a function of propagation distance, and are governed by Gaussian mode propagation that takes into account M^2 of the corresponding pump sources:

$$w_c(z)^2 = {w_{0c}}^2 + \left(\frac{\lambda_c}{\pi w_{0c}}\right)^2 z^2; \quad w_p(z)^2 = {w_{0p}}^2 + \left(\frac{M^2 \lambda_p}{\pi w_{0p}}\right)^2 z^2 \quad (2.8)$$

The cavity mode is assumed to be diffraction limited, and M^2 in equation (2.8) is the beam quality of the pump source. λ_c and λ_p are the laser and pump beam wavelength respectively, and w_{0c} and w_{0p} are the cavity and pump beam waist radii respectively. z is the propagation distance from the

beam waist position, which is assumed to be at the pump incident facet of the laser crystal.

The steady-state population inversion density, $\Delta N = N_b - N_a$, could then be calculated from (2.6):

$$\Delta N(r,z) = \frac{\tau f R \eta_Q \cdot r_p(r,z) + \Delta N^0}{1 + \frac{c\sigma\tau}{n} f S \cdot r_c(r,z)} \tag{2.9}$$

ΔN^0, as defined before, is the population inversion density in the laser crystal when it is not pumped, and can be approximated by $-f_a N$ if most of the atoms are assumed to be in the lower manifold when the crystal is not pumped, N being the dopant concentration. f is then $f_a + f_b$, the sum of the population fractions corresponding to the lower and the upper laser levels.

Finally, the steady-state condition of the quasi-three-level Nd:YAG laser can be expressed as:

$$G = \delta = \frac{2\sigma l_{cav}}{n} \iiint_{crystal} \Delta N(r,z) \cdot r_c(r,z) r dr d\theta dz \tag{2.10}$$

where G is the roundtrip gain and equals the roundtrip cavity passive loss, δ, at steady state. The intracavity photon density ($S \cdot r_c(r,z)$), hence also the output power, could then be solved numerically by substituting equation (2.9) into (2.10). It should be noted that equation (2.10) is slightly modified from those presented in [12,14] to account for a laser cavity that is longer than the laser crystal, as pointed out in footnote 25 of [14]. Detailed derivation of equation (2.10) is provided in the Appendix.

2.3 Experimental Setup

The experimental apparatus is illustrated in Figure 2.1.

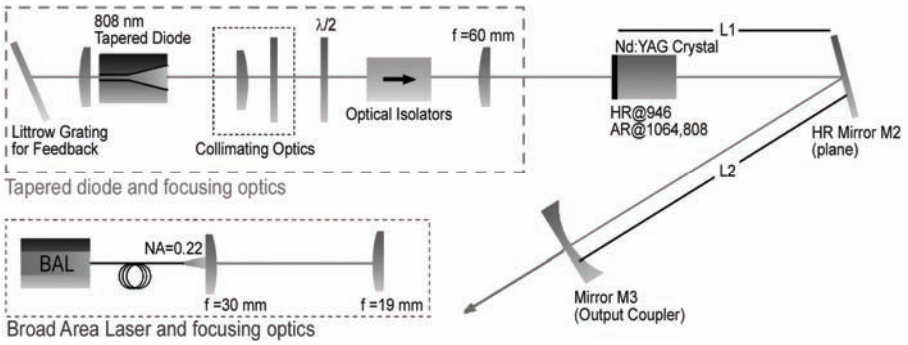

Figure 2.1- Experimental setup showing the two pump sources used, the ECDL (dashed line) and the BAL (dotted line), respectively. An extra plane mirror, M2, was inserted in the laser cavity to eliminate back reflections of the 808 nm pump light.

The tapered diode amplifier consists of a 1 mm long ridge region, and a 3 mm long tapered gain region that has a full divergence angle of 4˚. The output facet on the tapered side was coated to give a reflectance of 0.5%, while the ridge side facet was AR coated to below 0.1% reflectance. An external Littrow grating on the ridge side was used to provide feedback and wavelength selectivity. The angle of the grating was tuned until the single pass absorption through the Nd:YAG crystal was maximized. General operating principles of tapered amplifiers can be found in section 1.1.2, while a detailed description of the particular tapered amplifier used here can be found in [27].

At the maximum driving current of 4.0 A, the external cavity tapered diode laser (ECDL) emits 2.7 W at 808 nm. The output was collimated using an f=3.1 mm aspheric lens and an f=50 mm cylindrical lens. Two optical isolators were used in series to provide 60 dB of isolation to protect the tapered diode laser from feedback, which could otherwise destabilize its operation. Before the isolators, a half-wave plate was inserted, which in combination with the polarizers inside the isolators, allowed for power control without altering the beam quality. A maximum power of 1.8 W at 808 nm was available after the isolators. The M^2 values of the fast and slow axes of the tapered diode laser were 1.2 and 2.8 respectively using the $1/e^2$ beam widths, and 1.2 and 4.1 respectively using the second-moments

method, which were measured directly with a Thorlabs BP109-IR beam profiler.

The pump beam from the ECDL was focused into the Nd:YAG crystal using an f=60 mm plano-convex lens, resulting in a beam waist radius measured to be 33 μm x 46 μm for the fast and slow axis respectively, according to the second-moments definition. The focusing into the Nd:YAG crystal described here, as well as in the BAL case, was optimized experimentally to obtain the highest output power at 946 nm. Figure 2.2 shows the corresponding beam waist profiles.

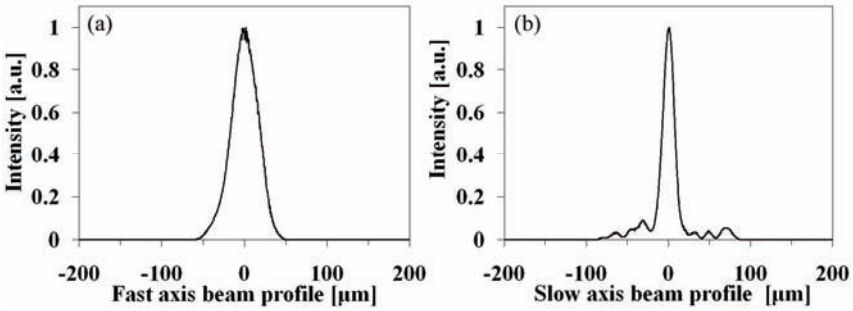

Figure 2.2 - Beam waist of the ECDL pump beam at the position of the Nd:YAG crystal for (a) the fast and (b) slow axis of the tapered diode laser using an f=60 mm plano-convex lens.

As seen in Figure 2.1, a simple hemispherical resonator was used. However, an extra plane mirror, M2 (AR@808/1064nm, HR@946nm), was inserted to avoid any 808 nm light from being reflected back through the 1% atm. Nd:YAG crystal. This arrangement further allowed for direct measurement of the intra-cavity beam waist, by analyzing the leakage 946 nm beam through M2. A 2% output coupler, M3, (R=100 mm) and a 5% output coupler (R=150 mm) were used respectively. The Nd:YAG crystal was 3 mm long, HR coated at 946 nm and AR coated at 808 and 1064 nm on the pump incident facet, and AR coated at 946, 808 and 1064 nm on the intra-cavity facet.

When pumping with the BAL, the output from the diode laser was coupled into a fibre with a core diameter of 105 μm and an NA=0.22 (Lumics LU0808M030). The output from the fibre was collimated with an f=30 mm lens and then focused into the Nd:YAG crystal with an f=19 mm lens, as illustrated in Figure 2.1 (dotted box). The maximum driving current of the

BAL pump was 3.5 A, yielding an output power of 2.5 W. The M^2 value of the BAL was measured to be 39, using $1/e^2$ beam widths, and was power independent. The beam was circularly symmetric and the waist radius at the focus of the f=19 mm lens was measured to be 46 μm. Figure 2.3 shows the BAL beam waist profile.

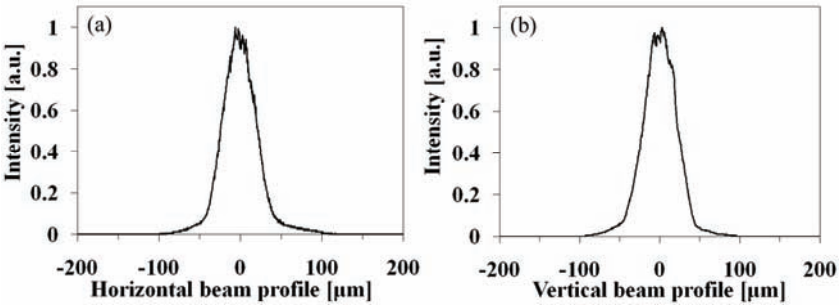

Figure 2.3 - BAL beam waist spatial profile at 3.5 A pump current, operated at 26.5 ˚C.

The emission spectra of the ECDL and BAL were measured with an Advantest Q8347 optical spectrum analyzer and are shown in Figure 2.4. The maximum single pass absorption achieved with the ECDL was 85% with the pump spectrum shown in Figure 2.4 (a), where it could be seen that the ECDL bandwidth was below the instrument resolution of 4 pm. The corresponding absorption coefficient was 6.4 cm^{-1}. The BAL wavelength was temperature tuned to obtain the maximum single pass absorption through the Nd:YAG crystal. This was achieved at a diode temperature of 26.5˚C. The corresponding spectrum was centered at 805.5 nm with a 2.5 nm bandwidth, as illustrated in Figure 2.4 (b). The maximum absorption achieved with the BAL was 70%, corresponding to an absorption coefficient of 4.0 cm^{-1}. The difference in absorption is due to the narrow spectral width of the ECDL and its ability to tune into the highest absorption peak of the laser material. In the latter part of section 2.4, the separate effects of spectral and spatial properties of the pump source and their relevance to the quasi-three-level laser's performance will be illustrated.

Equation (2.1) could be differentiated with respect to l_{xtal} to find the optimal crystal length based on the pump absorption, the cavity's passive roundtrip loss and output coupling [14]. For the ECDL with 5% output coupling, this was calculated to be 2.8 mm, which was close to the 3 mm crystal used. For the BAL, the theoretical optimal length was 3.7 mm. This could not be

confirmed experimentally, but a 3 mm crystal was found to perform better than a 1.5 mm crystal experimentally.

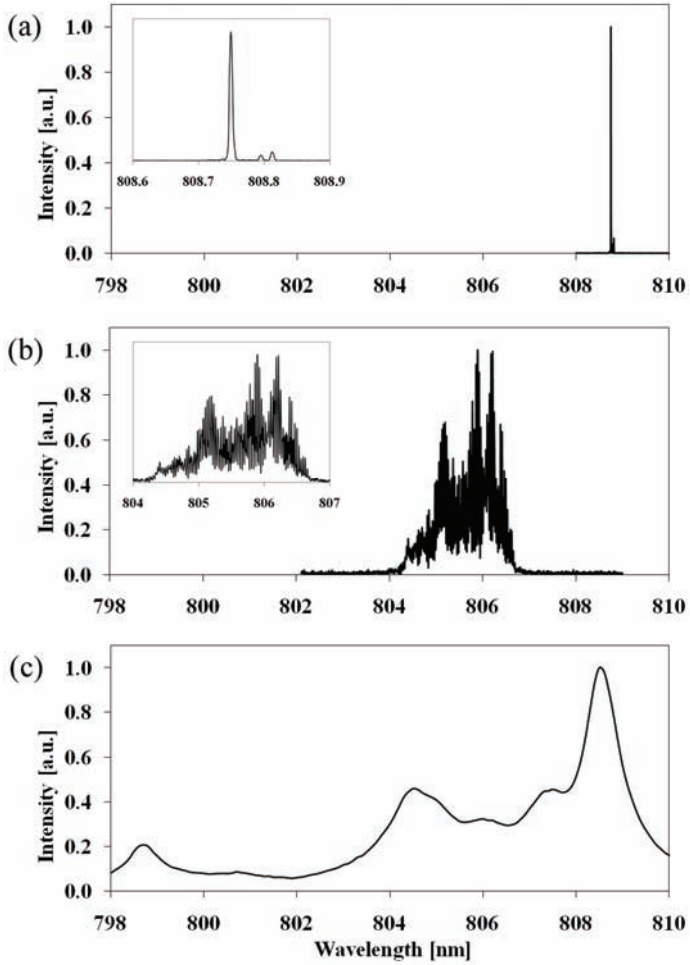

Figure 2.4 - Output spectrum of (a) the ECDL at 4.0 A drive current and a temperature of 20 ˚C and (b) the BAL at 3.5 A drive current and a temperature of 26.5 ^{o}C, along with (c) the absorption spectrum of Nd:YAG. The absorption data plotted in (c) is taken from NASA Database LASERS [28].

2.4 Experimental Results and Discussion

The model described in the previous section is used to analyze the experimental results. In order to compare the experimental data with the numerical calculations, Eq. (2.1) is integrated over the laser crystal volume and the resulting roundtrip gain is equated with the losses. Operating points of the 946 nm laser at various pump powers could then be obtained. The resulting output power curves as well as the experimental data are plotted in Figure 2.5.

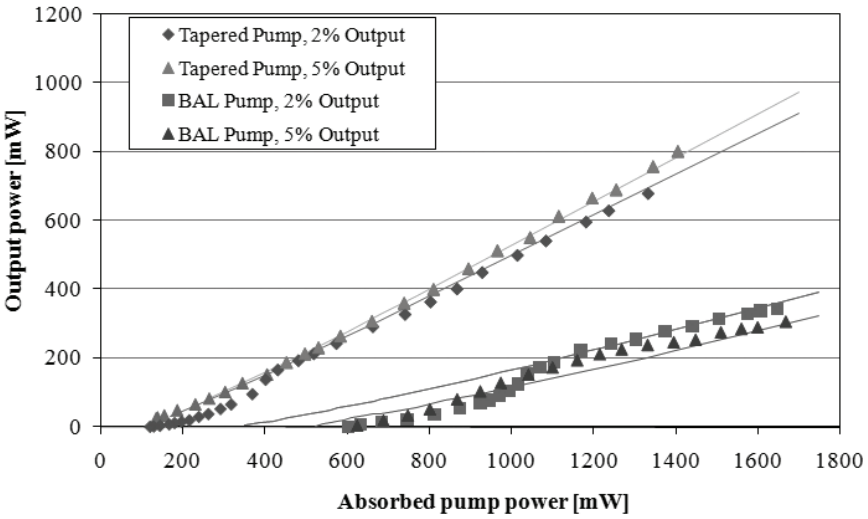

Figure 2.5 - Numerical modeling (solid lines) and experimental results (dots) of the output power from the 946 nm Nd:YAG laser pumped by an ECDL and a BAL respectively.

Table 1 summarizes the constants used in the numerical calculation while Table 2 lists the pump and cavity beam parameters used. The passive roundtrip loss of the cavity was determined by comparing experimental slope efficiencies for the different output couplers, while keeping the overlap between the pump and laser cavity mode constant, and was found to be 0.4%. Thus the total roundtrip loss, δ, used in the numerical calculation, was 2.4% and 5.4% respectively for the 2% and 5% output couplers, while the quantum efficiency, η_Q, was used as the fitting parameter. The crystal temperature was assumed to be at 300 K.

Table 2.1 - Material constants for Nd:YAG used in the numerical calculations.

Constants	Value	Ref.
Stimulated emission cross section, σ	5.3 x 10^{-20} cm^2	[7]
Population fraction in lower laser level, f_a	0.0075	[12]
Population fraction in upper laser level, f_b	0.612	[12]
Refractive index at 808 nm, n_p	1.8212	[29]
Refractive index at 946 nm, n_c	1.8172	[29]
Nd^{+3} doping density, N	1.38 x 10^{20} cm^{-3}	[13]
Upper state fluorescence lifetime, τ	230 μs	[13]

Table 2.2 - Measured parameters that were used in the numerical calculations.

	Tapered Diode Pump		BAL Pump	
	2% O.C.	5% O.C.	2% O.C.	5% O.C.
Pump waist radius, w_{0p}	33 μm	33 μm	46 μm	46 μm
Cavity mode waist radius, w_{0c} [a]	55 μm	38 μm	55 μm	50 μm
Pump beam quality, M^2	4	4	39	39
Absorption coefficient, α	6.4 cm^{-1}	6.4 cm^{-1}	4.0 cm^{-1}	4.0 cm^{-1}
Radius of curvature of output coupler	100 mm	150 mm	100 mm	150 mm
Cavity length, l_{cav}	102 mm	153 mm	106 mm	151 mm

[a] Differences in the cavity mode waist radii were due to slight differences in cavity lengths between experiments. The cavity mode waist radius is very sensitive to cavity length as the laser is near its stability limit.

Due to thermal lensing and gain aperture effects, cavity lengths in the experimental setups are in fact a few millimeters outside the stability region, as per the usual ABCD matrix analysis for cold cavities. As the cavity mode size is very sensitive to slight variation in the cavity length in this region, the cavity lengths, hence also the cavity mode sizes, were optimized experimentally to obtain the highest 946 nm output power for each experiment. The cavity mode sizes used in the numerical calculations were, in turn, measured experimentally, using the leakage power through mirror M2. The quantum efficiency term, η_Q, was used as a fitting parameter to fit the calculated output power curves to the experimental data points shown in Figure 2.5. Good fits were obtained when a quantum efficiency, η_Q, of 0.85 was used for all four experimental configurations. N. P. Barnes et al. measured η_Q for a 1% atm. doped Nd:YAG crystal to be 0.874 and 0.835 using a photometric and a calorimetric method respectively [30], while N. Pavel published a value of 0.78 [31]. Variations in the quantum efficiency may be due to variation in the actual Nd concentration of the YAG crystals, crystal imperfections, as well as experimental inaccuracies. Our value of

0.85, calculated from the laser model, is in good agreement with the previously published values of N.P. Barnes et al. [30]. This indicates that by only taking into account second-moment M^2 of the pump source, and the quantum efficiency values reported by N.P. Barnes et al., reasonable prediction of laser performance can be made with the relatively simple model described in the previous section. This is in contrast to the more elaborate models recently proposed, that for example, take into account excited state absorption [32], and thermal effects on fluorescence lifetime and absorption saturation [26].

From Figure 2.5, it can be seen that the threshold is significantly reduced from 0.60 W absorbed pump power in the BAL pumped laser to 0.15 W with the ECDL pumped laser. The slope efficiency, in terms of absorbed pump power, increased from 28% in the case of the BAL pump to 65% in the ECDL pumped laser, resulting in an output power of 800 mW at 946 nm, which to the authors' knowledge is the highest attained with a single emitter diode laser pump source.

The measured M^2 of the BAL pumped 946 nm laser was 1.4 and 1.2 for the horizontal and vertical direction respectively when using the 5% output coupler at maximum pump power. Similarly, the M^2 of the ECDL pumped 946 nm laser was measured to be 1.1 in both directions using the 5% output coupler, at maximum pump power.

Despite the theoretical calculation in [14] calling for $w_p/w_c \rightarrow 0$, it was found in all of our experiments that the optimal w_p/w_c was always close to and slightly less than 1. By slightly varying the cavity length, one can probe the effect that changing w_p/w_c has on the output power. It was observed experimentally that, if $w_p/w_c < 1$, the wings of the cavity mode is not pumped sufficiently, and the output power decreases rapidly. If $w_p/w_c > 1$, the pump photons hitting areas outside the fundamental laser mode in the slow axis starts to excite higher order modes, and M^2 of the 946 nm laser starts to degrade. Figure 2.6 illustrates these observations. The pump waist radius for this particular experiment was 35 μm x 15 μm for the slow and fast axis respectively, and it can be clearly seen that the M^2 of the laser starts to degrade once the cavity mode size becomes smaller than the pump beam mode size in the slow axis direction.

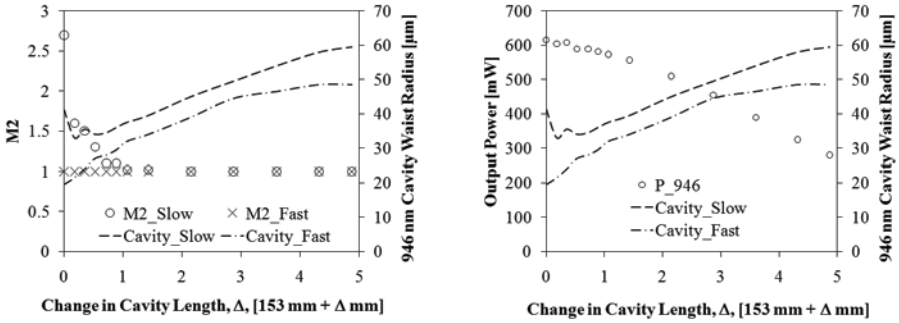

Figure 2.6 - M^2 (left) and output power (right), as a function of the cavity mode size, plotted in dashed lines and are determined by the cavity length.

2.4.1 Spectral properties of pump source

The spectrum of external cavity diode lasers are typically narrow; thus, spectral overlap between the pump emission spectrum and the absorption peak of Nd:YAG becomes critical. The absorption coefficient was found experimentally to vary from 6.4 cm^{-1} to 3.9 cm^{-1} for a wavelength shift from 808.76 nm to 808.32 nm, leading to a 20% reduction in the 946 nm output power, thus underlining the necessity for a stable pump spectrum in case of narrow spectral ECDL pumping. A BAL usually emits light at a broad spectrum that can excite atoms across several absorption peaks, thus making the output power less sensitive to changes in the pump spectrum.

In the following, the overall improvement moving from a BAL to an ECDL pumped system is separated into a spatial and a spectral contribution. This is done by detuning the ECDL spectrum to match the absorption coefficient of the BAL. Figure 2.7 shows three plots of the 946 nm output power using the 5% output coupler: the two upper curves show the performance when pumping with the ECDL source, diamonds indicating optimum pump wavelength, squares illustrating the case where the pump wavelength has been detuned by 0.44 nm, resulting in an absorption coefficient of 3.9 cm^{-1}, close to that of the BAL pumped system (4.0 cm^{-1}). A plot of the BAL pumped 946 nm laser is also shown for comparison (triangles).

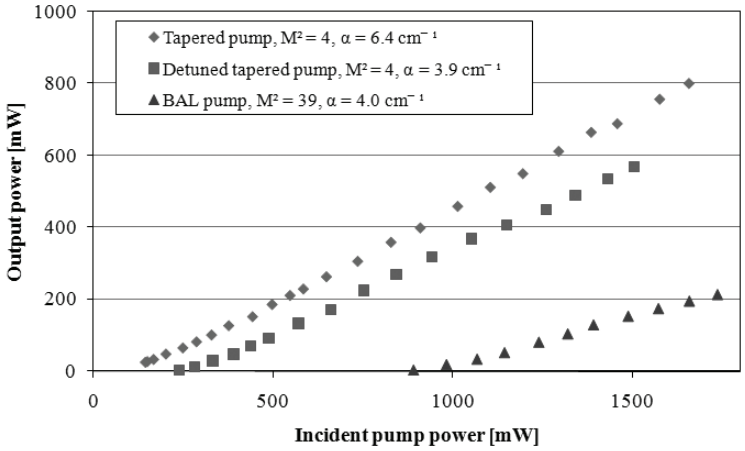

Figure 2.7 - Power characteristics showing the power sensitivity on center wavelength of the external cavity tapered diode laser pump source.

With the ECDL pump laser detuned to match the absorption obtained with the BAL pump, the output power is still increased from 150 mW to more

than 550 mW (at an incident pump power of 1.5 W). This emphasizes the improvement in output power is primarily due to the better beam quality provided by the ECDL over the BAL. The improved spectral properties of the ECDL pump laser further allows matching of the pump spectrum to the highest absorption peak of Nd:YAG, increasing the output power additionally by 23 % to 700 mW at 1.5 W incident pump power.

Figure 2.7 clearly shows that the slope efficiency of the detuned ECDL case is only slightly reduced when compared to that at the optimal wavelength, indicating that the spectral properties of the pump laser is of less importance when compared to its spatial beam quality. This suggests that a tapered diode pump source operating in broad spectrum mode may suffer marginal performance degradation, while, as in the BAL case, would benefit from a broad spectrum covering several absorption peaks of Nd:YAG, making the output power at 946 nm less susceptible to drift. In addition, the tapered diode's reduced sensitivity to feedback in broad spectrum mode could mean that expensive and lossy Faraday isolators could be removed to significantly increase the available pump power. This in turn may offset the slightly lower output power at 946 nm, as illustrated by the detuned curve in Figure 2.7.

The recommendation above was experimentally tested by replacing the grating feedback in Figure 2.1 with a broadband dielectric mirror, and by replacing the isolators with a polarizer in combination with a quarter-wave plate to provide optical isolation. This made 2.7 W of incident pump power available, resulting in 850 mW of output power at 946 nm. The emission spectrum of the tapered diode laser was observed to shift as the Nd:YAG crystal became aligned, indicating the presence of feedback from the crystal surface. This did not appear to affect the laser's operation, and good absorption could be achieved by temperature tuning. However, it underlines the importance of proper coatings on the crystal and output coupler surfaces, and/or the use of a folded cavity design to minimize feedback from the output coupler. It was observed that a slight tilt of the Nd:YAG crystal, of 17 mrad, was sufficient to eliminate any observable feedback to the diode. This resulted in slightly lower output power (700 mW @ 2.7 W incident pump power.) One practical realization of this is the use of tapered diode lasers with the rear facet of the single mode waveguide coated for high reflectivity, as opposed to VBG's or Littrow gratings; thus, making the pump source simpler and more efficient.

2.5 Summary and Outlook

A detailed experimental comparison between a ECDL pumped and a BAL pumped quasi-three-level laser has been carried out; based on the results, a simple and cost-effective broad-spectrum tapered diode pump source has been proposed and demonstrated. In the narrow spectrum experiments, a stable output of 800 mW with a slope efficiency of 65% has been achieved, which to the authors' knowledge is the highest attained with a single-emitter diode laser pump source, while at the same time, achieving an M^2 of 1.1 for the 946 nm beam. Experimental data shows good agreement with a relatively simple quasi-three-level laser model when using a quantum efficiency, η_Q, of 85%, which was in good agreement with previously published values.

In broad-spectrum pumping, it was demonstrated that the combination of a quarter-wave plate and a polarizer was sufficient in providing isolation for the tapered diode laser pump source, without the use of Faraday isolators, eliminating the complexity in aligning and the cost associated with the use of such components. Furthermore, significantly higher pump power became available, resulting in an output power of 850 mW at 946 nm.

With the pumping scheme of the quasi-three-level CW laser optimized, efficient non-linear parametric conversion using novel cavity configurations is possible. For example, a relatively large CW intracavity circulating field could be coupled out through a non-linear loss that is introduced by frequency mixing with an external, single-passed, pulsed laser [33]. Alternatively, the procedure for pump beam optimization could be applied to quasi-three-level Q-switched lasers, where the instantaneous power would be significantly increased, which would also increase the efficiency of the non-linear conversion process. Cavity design and operation of a Q-switched quasi-three-level Nd:YAG laser will be described in the next chapter.

3. Passive Q-switched Operation

The goal of this chapter is to give a brief and broad overview of passively Q-switched, quasi-three-level lasers. It aims to give the reader an introduction to passively Q-switched lasers, and serves as the background to Chapter 4 – passively synchronized Q-switching between two solid-state lasers. In particular, a general background is given in section 3.1, the rate equations for a single passively Q-switched, three-level laser is derived in section 3.2, and finally, a brief discussion on the issues encountered during experimental work will be presented in section 3.3. The contribution of the PhD work towards single passively Q-switched lasers is minimal.

3.1 Background

With the rapid growth and emergence of high brightness semiconductor diode lasers, diode pumped passively Q-switched quasi-three-level lasers that are becoming more common. The first demonstration of such a laser at the 946 nm transition of Nd:YAG was demonstrated by Liu et al. in 1997 using a monolithic chromium, neodymium co-doped YAG laser crystal [34]. The authors achieved 25 mW of average power and 7 μJ of pulse energy using a 2 W broad area diode pump source. Since then, several reports have been published on passively Q-switched operation of diode pumped quasi-three-level lasers [35-37]. Most notably, Kimmelma et al. achieved 3.7 kW of peak power in a 6 ns pulse, using a 9 mm long hemispherical cavity and a 4.6 W diode pump source [35].

As with CW operation, passively Q-switched lasers at 946 nm pumped by diode arrays have also been reported [5,38-41]. However, using the same argument that tapered diodes could similarly be arrayed and stacked in the future, the discussion reported here will be limited to single-emitter pump sources.

The first demonstration of an actively Q-switched Nd:YAG 946 nm laser is reported in [42]. However, because active systems are generally more expensive and require additional electronics and bulky Q-switches, the current PhD work is focused on passive Q-switching, and the synchronization experiment described in Chapter 4 is also performed passively.

As discussed in the previous chapter, the pump beam radius should be minimized in CW operation to ensure efficient conversion of the absorbed pump photons into useful laser photons if diffraction effects of the pump and cavity beams are neglected. Under Q-switched operation, however, there is a trade-off between efficiency and energy storage. While small pump and cavity beam waists in the laser crystal would ensure efficient lasing, large pump and cavity beam waists would achieve high energy pulses – since a larger number of atoms will be excited during the low Q period and more energy will be stored. Therefore, low repetition rate, high pulse energy operation is a balancing act between the two. In the experiments that will be described in Chapters 4 and 5, the pump and cavity beam waist radii are optimized experimentally in terms of peak power. As with the CW experiment, the optimal cavity beam waist radius was experimentally found

to be close to or slightly larger than the pump beam waist radius in the laser crystal, but the pump beam waist radius in this case was increased to 59 μm (h) x 80 μm (v).

With the relatively large pump beam waist radius, one can argue that the pump source beam quality is not as important as in the CW case, but as reported by [15], a high beam-quality pump source for an actively Q-switched laser yielded more than twice the output power than a similar system with poorer pump beam quality. To illustrate this point more precisely, a diffraction limited beam at a wavelength of 808 nm, with a beam waist radius of 100 μm, propagating in a medium with refractive index 1.8, has a Rayleigh range of 70 mm. For a beam with $M^2 = 4$ (as in the case of the tapered diode pump source), this reduces to 17 mm. For a beam with $M^2 = 40$ (as in the case of the BAL pump source), this reduces further yet to 1.7 mm. Since the Rayleigh length is the point where the beam cross-sectional area has diffracted to twice its area at the beam waist (and larger still beyond this point), beam quality is an important factor for efficient lasing in a 3 mm laser crystal.

Yet another way to look at this is: assuming the pump absorption remains at approximately 4 cm^{-1}, the optimal laser crystal length as indicated by equation (2.1) remains to be approximately 3.7 mm. Then, it implies that the worst beam quality that can be tolerated in the current system without degrading the efficiency significantly is approximately $M^2 = 19$, which would give a Rayleigh length of 3.7 mm.[2]

[2] To be completely precise, equation (2.4) should be used to obtain the smallest pump volume that is obtainable with a pump source with a certain beam quality and crystal length. This would further reduce the Rayleigh length by a factor of 3, and similarly, reduce the worst tolerable M^2 by a factor of 3. Given a 3.7 mm long laser crystal, the worst tolerable beam quality is then: $M^2_{worst\ case} = 19/3 = 6.3$.

3.2 Rate equations

Similar to the CW laser, coupled rate equations describing the population inversion density and the photon density can be derived for Q-switched lasers. The difference here is that the cavity loss is now time dependent. To be precise, the cavity loss is now the cavity passive loss plus the additional time dependent loss introduced by the Q-switch.

The purpose of the model described here is to study the behavior of passively synchronized Q-switching between two end-pumped solid-state lasers, which is the topic of Chapter 4. Several assumptions are made to simplify the rate equations used in the CW model. Firstly, we now consider a strictly three-level system. This is simply done by setting $f = f_a + f_b = 1+1 = 2$. Secondly, we again neglect the effect of diffraction in the pump and cavity beams:

$$r_c(r,z) = \frac{1}{\pi w_c l_{cav}}; \quad r_p(r,z) = \frac{1}{\pi w_p l_{xtal}} \tag{3.1}$$

where w_c and w_p are now the z-independent beam radii. The population inversion density, ΔN, in units of m^{-3}, then becomes:

$$\frac{d\Delta N}{dt} = \frac{2R}{\pi w_p{}^2 l_{xtal}} - \frac{2\Delta N}{\tau} - \frac{2c\sigma S l_{xtal}\,\Delta N}{n\pi w_c{}^2 l_{cav}} \tag{3.2}$$

where the parameters are defined as in section 2.2 and summarized in the List of Symbols and Abbreviations at the beginning of this thesis. The exception is that R is now the absorbed pump photon density, and the absorbed pump photons are assumed to be evenly distributed throughout the length of the laser crystal. The time derivative of the total number of photons in the cavity, S, is then:

$$\frac{dS}{dt} = \frac{c\sigma}{n}\Delta N\, S\frac{l_{xtal}}{l_{cav}} - \frac{cS\delta(t)}{2l_{cav}} + \frac{\Delta N}{\tau}\left(\pi w_c{}^2 l_{xtal}\right)\varepsilon \tag{3.3}$$

where ε is the fraction of photons emitted spontaneously that contribute to the laser mode. The cavity roundtrip loss, δ, is now time dependent – specifically, it depends on the loss induced by the saturable absorber. $\delta(t)$ will be defined later, towards the end of this section.

Furthermore, in order to be able to more easily calculate the output power, the photon flux density, instead of the total number of photons, is considered:

$$\phi = \frac{Sc}{n}\frac{1}{\pi w_c{}^2 2l_{cav}}; \quad \frac{d\phi}{dS} = \frac{c}{2n\pi w_c{}^2 l_{cav}} \tag{3.4}$$

where ϕ is the photon flux density in $m^{-2}s^{-1}$. In this case, equation (3.3) becomes:

$$\frac{d\phi}{dt} = \frac{d\phi}{dS}\frac{dS}{dt} = \frac{c\sigma}{n}\Delta N\phi\frac{l_{xtal}}{l_{cav}} - \frac{c\delta(t)}{2l_{cav}}\phi + \frac{\Delta N}{\tau}\frac{cl_{xtal}}{2nl_{cav}}\varepsilon \tag{3.5}$$

With this definition of the photon flux density, output power of the laser as a function of time is simply:

$$P_{out}(t) = T_{out}\,\phi(t)\,\pi w_c{}^2\frac{hc}{\lambda_c} \tag{3.6}$$

where T_{out} is the output coupling.

Having established the rate equations for the population inversion density and the photon flux density in equations (3.2) and (3.5) respectively, we can now turn our attention to the time dependent loss, $\delta(t)$. The passive Q-switch under consideration is a saturable absorber, which acts as a four-level system itself. Figure 3.1 illustrates the energy level diagram of the saturable absorber used, a Cr^{4+}:YAG crystal.

The transitions between energy levels $1 \rightarrow 3$, and between levels $2 \rightarrow 4$, are responsible for a fairly wide absorption spectrum at around 1 μm. Energy level 2 has a relatively long lifetime of $\tau_2 = 3.5$ μs [43], while levels 3 and 4 have quick lifetimes that allow electrons to relax back to energy level 2 after an absorption has taken place. Thus, when ground level 1 is depleted, the loss is saturated and the crystal becomes transparent to the laser wavelength, assuming σ_e is small or negligible.

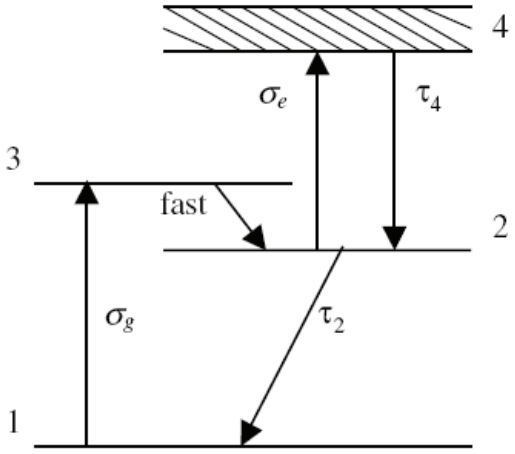

Figure 3.1 - Cr:YAG energy level diagram. Source: Zhang et al. [43]

In the simulation, the transition from energy level 3 to 2 is assumed to be instantaneous, and therefore, the population density in energy level 3, N_3, is assumed to be zero. The lifetime of energy level 4, τ_4, is between 50 to 550 ps [43], and the equations that describe the cavity loss, $\delta(t)$, are then:

$$\delta(t) = \delta_{passive} + T_{out} + 2\sigma_g \Delta N_{gsa} l_{SA}\left(\frac{w_{SA}^{\,2}}{w_c^{\,2}}\right) + 2\sigma_e \Delta N_{esa} l_{SA}\left(\frac{w_{SA}^{\,2}}{w_c^{\,2}}\right)$$

$$\frac{d\Delta N_{gsa}}{dt} = -2\sigma_g \Delta N_{gsa}\left(\frac{w_{SA}^{\,2} l_{SA}}{w_c^{\,2} l_{cav}}\right)\phi + \frac{N_2}{\tau_2}$$

$$\frac{d\Delta N_{esa}}{dt} = 2\sigma_g \Delta N_{gsa}\left(\frac{w_{SA}^{\,2} l_{SA}}{w_c^{\,2} l_{cav}}\right)\phi - 4\sigma_e \Delta N_{esa}\left(\frac{w_{SA}^{\,2} l_{SA}}{w_c^{\,2} l_{cav}}\right)\phi - \frac{N_2}{\tau_2} + \frac{2N_4}{\tau_4}$$

$$\Delta N_{gsa} = N_1$$

$$\Delta N_{esa} = N_2 - N_4$$

$$N_{SA} = N_1 + N_2 + N_4 \tag{3.7}$$

where $\delta_{passive}$ is the cavity's passive loss, T_{out} is the output coupler transmission, ΔN_{gsa} is the population density difference between energy levels 1 and 3, and ΔN_{esa} is the population density difference between energy levels 2 and 4, l_{SA} is the thickness of the saturable absorber, w_{SA} is the beam

radius inside the saturable absorber, and N_{SA} is the doping concentration of the Cr^{4+} ions in the saturable absorber. It is noted that $\delta(t)$ is dimensionless, and ΔN_{gsa} and ΔN_{esa} are measured in m^{-3}.

Equations (3.2), (3.5), and (3.7) are then the set of coupled differential equations that describe the generation of passively Q-switched pulses in a single diode end-pumped solid-state laser. These will be expanded to describe two lasers in the next chapter, where the two are coupled through a common saturable loss to achieve synchronized Q-switching.

A more complete numerical model that includes the stark-split energy structure in a quasi-three-level system is described in [38]. However, in the qualitative analysis currently considered, the set of equations described above is used for simplicity.

3.3 Single Q-switched Laser Experiments

It has been previously reported that using Cr^{4+} ions to passively Q-switch the 946 nm transition lead to Q-switch mode-locking behavior, where mode-locked pulses are modulated by a Q-switch envelope [44,45]. This was also observed in the current experiment. A fast photodiode (Thorlabs SV2-FC, 3dB roll-off at 2 GHz, rise time = 150 ps) was used together with an Agilent 8563 spectrum analyzer with 27 GHz bandwidth. The resulting spectrum shows clearly the multiple longitudinal mode spacing that corresponds to the inverse of the cavity roundtrip time. Figure 3.2 shows the power spectrum of a 100 mm long cavity, which would give a mode spacing of 1.5 GHz. The cavity being considered is a linear hemispherical cavity consisting of a 3 mm long Nd:YAG laser crystal, a 0.25 mm thick Cr:YAG crystal placed at Brewster's angle, and a T = 15% curved output coupler (r = -100 mm).

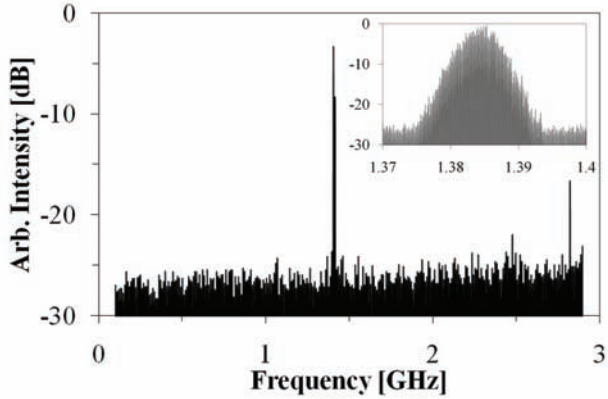

Figure 3.2 - Power spectrum of a passively Q-switched Nd:YAG laser at 946 nm, with l_{cav} = 100 mm.

While previous literature have pointed to excited state absorption in the Cr:YAG as being responsible for the loss modulation that causes mode-locking [44-46], this is not supported by the observations noted in the current setup. The mode-locking behavior persists even when: 1) a thicker Cr:YAG crystal is used, 2) the pump power is lowered to close to threshold, and 3) when the Cr:YAG crystal is moved away from the beam waist.

Several other attempts were made to suppress the mode-locking behavior in the 946 nm laser. An etalon (glass plate, $l \cong 1$ mm) was inserted into the cavity to induce differential loss for the longitudinal modes. The whole laser was put in an enclosure and was purged with nitrogen to eliminate the

possibility of water absorption. Neither of these methods was successful in obtaining pure Q-switching.

The laser cavity was also shortened to increase the longitudinal mode spacing, which could potentially achieve single mode operation if it exceeds the gain bandwidth of Nd:YAG. However, Q-switched mode-locking was still observed down to a cavity length of 50 mm. Figure 3.3 shows the corresponding power spectrum.

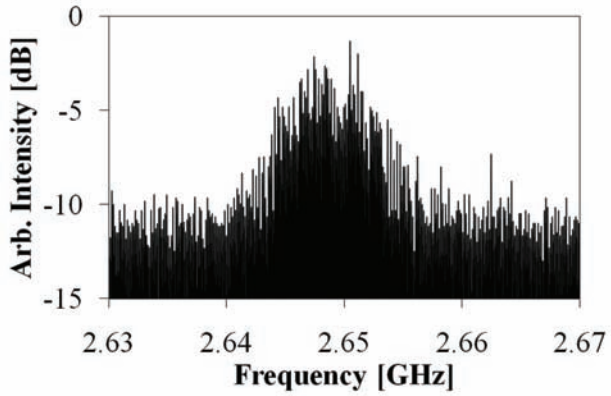

Figure 3.3 - Power spectrum of a passively Q-switched Nd:YAG laser at 946 nm, with l_{cav} = 50 mm.

As can be seen, the signal obtained at this point was fairly weak due to the 3dB roll off of the detector. Thus, further shortening of the cavity could not yield new information on the behavior of the laser.

In the end, it was determined that the Q-switched mode-locking behavior is not critical to system performance at this stage of the project. It would not be of concern for fluorescence imaging if the final UV pulse is shaped like the Q-switched mode-locked 946 nm pulse since the image acquisition would average out the signal. It would also not affect the non-linear conversion efficiency as long as the parametric conversion is non-depleted (i.e. as long as the 532 nm beam is not depleted). If however, the mode-locked pulses do deplete the 532 nm beam, the conversion could be significantly less efficient. In this case, a ring-laser, similar to the one described in section 6.4 could be used to enforce single-mode operation.

4. Synchronized Q-switching

4.1 Background

Synchronized pulsing of different wavelength lasers is by no means a new concept. In fact, simultaneous dual-wavelength operation of a ruby laser was reported by Schawlow and Devlin [47] just seven months after Maiman's demonstration of the world's first laser [48]. This was then quickly followed by several other publications for both the visible and near infrared spectrum [49-53]. Because these first lasers were either pumped by flash-lamps, or by electrical pulses, synchronization was effectively achieved by gain-switching.

To the author's knowledge, the first demonstration of synchronized Q-switching was reported by Caviello et al. in 1965 with a Ruby laser at 694.3 nm and 692.9 nm [54]. Figure 4.1 below shows their experimental setup.

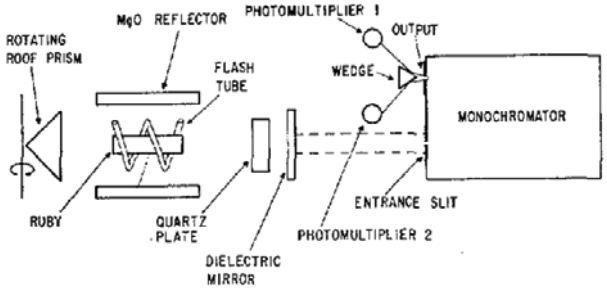

Figure 4.1 – Experimental setup for synchronized Q-switching in a ruby laser by Caviello et al. Figure extracted from [54].

It was an extremely elegant experiment, with both lasers sharing the same gain medium, Q-switch – a rotating roof prism in this case, and a birefringent quartz plate that was used to control the relative losses of each laser and compensated for the difference in stimulated emission cross-sections.

The main motivation in these early works were in long distance interferometry [52] and in power scaling [53]; in recent years, however, considerable interests have been placed on non-linear frequency mixing, which implies that the lasers should be able to operate at fairly different wavelengths in order to cover a wide spectral range. Figure 4.2 shows the

possible wavelengths that is covered by summing the various transitions of Nd:YAG, including the quasi-three-level transitions at 939 nm and 946 nm.

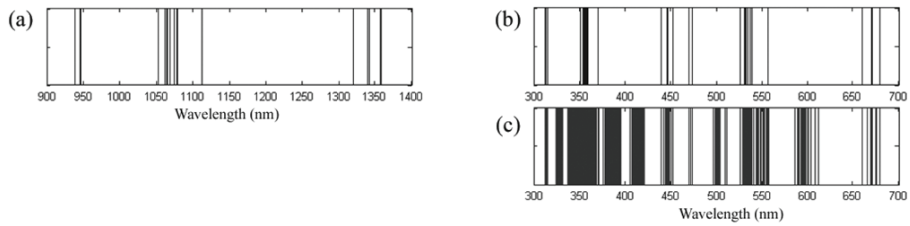

Figure 4.2 - Spectral range of non-linear frequency mixing covered by Nd:YAG up to the third harmonic. (a) fundamental wavelengths of Nd:YAG including the quasi-three-level transitions at 939 nm and 946 nm, (b) only the degenerate wavelengths of 2ω and 3ω, (c) possibilities using sum-frequency mixing.

The main difficulty in synchronization of lasers with significantly different wavelengths lies in compensating for their different gain cross-sections. In 1990, Henderson used two active Q-switches and compensated for the difference by opening the Q-switches at different times and achieved good, though not perfect, temporal overlap [55]. In the same year, Shen published an article on the oscillation condition for simultaneous multiple wavelength oscillations, deriving an equation to obtain the proper mirror reflectivities that account for the cross-section difference [56]. In addition to this, Lin et al. suggested using different cavity lengths to ensure the build-up times of the two pulses are equal [57].

All of the above approaches were suggested for simultaneous dual-wavelength lasers (SDWL's) that share a common gain medium. Alternatively, the cross-section difference could also be compensated for by using two separate gain crystals and separate pump sources, and this has indeed been demonstrated for two four-level lasers [58,59].

Depending on the type of Q-switches used, synchronization can be achieved either actively or passively, where the former uses electronics to control the timing of the laser pulses, and the latter uses optical methods. Passively synchronized systems are in general more compact and cost-effective; however, they are less stable due to thermal and mechanical noise that can affect the timing of the synchronized pulses.

In both actively and passively Q-switched systems, the cavity configuration can be roughly categorized into the following:

A. Simultaneous Dual Wavelength Lasers (one gain medium)
    a. Common cavity, with a shared Q-switch
    b. Y shaped cavity, with separate Q-switches
B. Separate gain media for the different wavelengths
    a. Separate cavities with separate Q-switches
    b. Y shaped cavity with separate gain crystals, but a shared Q-switch
C. Optical bleaching by external sources

Since synchronized active Q-switching is extensively studied [54-57,60-65], and is generally more costly and complex, the current PhD work is focused on using passively synchronized lasers for non-linear frequency mixing. In particular, a Y-shaped cavity, containing a shared saturable absorber (SA) and separate gain crystals, is used to synchronize a quasi-three-level and a four-level Nd:YAG laser. A brief description of prior art is presented in section 4.1.1; a numerical model is described in section 4.2, while the experimental results and a brief summary are presented in sections 4.3 and 4.4 respectively.

4.1.1 Prior Art

It should be noted that while the methods described above [56-59] have met with good success in passively synchronizing four-level Q-switched lasers, between the $^4F_{3/2} \rightarrow {}^4I_{13/2}$ and $^4F_{3/2} \rightarrow {}^4I_{11/2}$ transitions, and even between two quasi-three-level lasers [66], very little work has been done on passive synchronization between a quasi-three-level laser and a four-level laser. To the author's knowledge, only two works have been published toward this end. Zhang et al. used the loss difference method and obtained SDWL operation at 1.06 μm and 946 nm; however, this required a large loss on the 1.06 μm laser, and the authors reported significant output power fluctuations [67]. Recently, Tsai et al. used a Q-switched 976 nm laser to gain switch a ytterbium medium at 1064 nm in an all-fiber system, achieving stable synchronization between the two. However, the relative delay between the two pulses was 1 μs [68]. The difficulty in achieving synchronization between these two laser lines lie in the significant difference in gain cross-sections and the reabsorption loss suffered by the quasi-three-level laser. In Nd:YAG, for example, the gain cross-section of the 946 nm transition is ten times less than that at 1064 nm [7, 13].

While the focus of the PhD work is on passive methods, there is one publication regarding active synchronization that is of particular interest due to the similarity in operating wavelengths and potential applications. Herault et al. used two active Q-switches to synchronize a quasi-three-level laser at 912 nm and a four-level laser at 1063 nm. By making the 912 nm pulse relatively long, a good temporal overlap was achieved [69]. The authors reported a timing jitter of 40 ns and subsequently generated 9 kW of peak power at 491 nm through non-linear cavity dumping.

Recently, Walsh published a review article on simultaneous dual wavelength lasers (SDWL's) [70]. While Walsh did not make a clear differentiation between CW and pulsed systems, he pointed out the distinction between single ion systems, as in the case of Nd:YAG, and systems involving some energy transfer process between the two lasers, where the lower laser level of the first laser would have a large lifetime and can transfer its energy to the upper laser level of the second laser. In particular, Walsh highlighted the Er:Tm:Ho:YAG laser. These lasers are interesting as they eliminate the gain competition problem in SDWL's; however, since the pump photon energy is split between the two lasers, the emission wavelengths are in the 2 μm region.

Several simultaneous dual wavelength lasers have already been mentioned above [47,49-52,54-57,64-67], and good temporal overlap have been reported for passively Q-switched SDWL's with two four-level transitions [57,64-65]. Several SDWL's at 1064 nm and 946 nm have been reported for CW operation [71,72], while the most relevant publication is the passively Q-switched SDWL at 1064 nm and 946 nm by Zhang et al. described above [67]. Unfortunately, the authors noted fluctuations in the output power and did not report on the temporal characteristics of the two pulses.

SDWL's require only one laser crystal and one pump source, but with the significantly different gain cross-sections between a quasi-three-level transition and a four-level transition, passive synchronization using a common gain medium appears to be difficult [67,68]. Adding to the gain competition problem is the gain sensitivity of the quasi-three-level laser on pump mode overlap and its requirement for small SA mode sizes, forcing the cavity to operate at close to the stability limit. Any gain fluctuations due to mechanical vibration and thermal effects changes the "competitiveness" of the quasi-three-level laser, and thus, also the ratio of output powers between the two lasers.

In [53], Gregg et al. synchronized five ruby lasers passively by using separate gain crystals and Q-switches for each laser, but coupled the cavities with beam splitters ($R \geq 35\%$). More recently, Tidemand-Lichtenberg et al. [58] and Janousek et al. [59] used two separate laser crystals and two diode pump sources to avoid gain competition, and a shared passive Q-switch to synchronize two four-level lasers. These approaches effectively solve the gain competition problem by using separate gain media, and are particularly useful for synchronizing lasers with very different gain cross-sections, such as the quasi-three-level and four-level lasers being considered here.

Two flash-lamp pumped four-level Q-switched lasers have also been passively synchronized by directing the output of one laser (master) to the Q-switch of the other (slave) [73]. The authors achieved good temporal overlap by adjusting the timing of the two flash lamp pump pulses and by making one of the resulting laser pulses relatively long when compared to the other. However, it quickly became apparent in preliminary experiments of this PhD and in previous literature [74] that a relatively large delay between the two lasers would result (~1 μs) for CW diode-pumping. Thus, synchronized Q-switching by bleaching with an external source in CW

pumped DPSS lasers would require one external source that is used to bleach both lasers simultaneously, requiring essentially a minimum of three lasers in total [53,74-75].

In this chapter, two separate gain crystals and a shared saturable absorber were used in a Y-shaped cavity to achieve stable synchronization between a 946 nm and a 1064 nm Nd:YAG laser. In contrast to the systems reported in [58,59], synchronization was achieved over a wide range of pump powers. In addition, by fine-tuning the pump power to each laser crystal, the temporal dynamics of passively synchronized Q-switching is investigated. The results presented here are based on the publication in [76], where stable, passively synchronized Q-switching between a quasi-three-level and a four-level laser was reported for the first time.

4.2 Numerical Modeling

Similar to the equations described in section 3.2 for a single Q-switched laser, rate equations describing two passively Q-switched lasers, sharing one common saturable absorber, are derived in this section. The difference here is that the rate equations of the two individual lasers are now coupled through the rate equations of the saturable absorber. This has been previously described in [55,59]; however, as in equation (3.2), one set of equations was modified here to describe a three-level system:

$$\begin{aligned}
\frac{d\Delta N_{946}}{dt} &= \frac{2R_{946}}{\pi {w_{p_{946}}}^2 l_{xtal_{946}}} - \frac{2\Delta N_{946}}{\tau} - \frac{2c\sigma_{946} S_{946} l_{xtal_{946}} \Delta N_{946}}{n_{946}\pi {w_{c_{946}}}^2 l_{cav_{946}}} \\
\frac{d\Delta N_{1064}}{dt} &= \frac{R_{1064}}{\pi {w_{p_{1064}}}^2 l_{xtal_{1064}}} - \frac{\Delta N_{1064}}{\tau} - \frac{c\sigma_{1064} S_{1064} l_{xtal_{1064}} \Delta N_{1064}}{n_{1064}\pi {w_{c_{1064}}}^2 l_{cav_{1064}}}
\end{aligned} \tag{4.1}$$

$$\frac{d\phi_j}{dt} = \frac{c\sigma_j}{n_j}\Delta N_j \phi_j \frac{l_{xtal_j}}{l_{cav_j}} - \frac{c\delta_j(t)}{2l_{cav_j}}\phi_j + \frac{\Delta N_j}{\tau}\frac{c l_{xtal_j}}{2 n_j l_{cav_j}}\varepsilon_j \tag{4.2}$$

$$\begin{aligned}
\delta_j(t) &= \delta_{passive_j} + T_{out_j} + 2\sigma_{g_j}\Delta N_{gsa} l_{SA}\left(\frac{{w_{SA_j}}^2}{{w_{c_j}}^2}\right) + 2\sigma_{e_j}\Delta N_{esa} l_{SA}\left(\frac{{w_{SA_j}}^2}{{w_{c_j}}^2}\right) \\
\frac{d\Delta N_{gsa}}{dt} &= -\sum_j 2\sigma_{g_j}\Delta N_{gsa}\left(\frac{{w_{SA_j}}^2 l_{SA}}{{w_{c_j}}^2 l_{cav_j}}\right)\phi_j + \frac{N_2}{\tau_2} \\
\frac{d\Delta N_{esa}}{dt} &= \sum_j 2\sigma_{g_j}\Delta N_{gsa}\left(\frac{{w_{SA_j}}^2 l_{SA}}{{w_{c_j}}^2 l_{cav_j}}\right)\phi_j - \sum_j 4\sigma_{e_j}\Delta N_{esa}\left(\frac{{w_{SA_j}}^2 l_{SA}}{{w_{c_j}}^2 l_{cav_j}}\right)\phi_j \\
&\quad - \frac{N_2}{\tau_2} + \frac{2N_4}{\tau_4} \\
\Delta N_{gsa} &= N_1 \\
\Delta N_{esa} &= N_2 - N_4 \\
N_{SA} &= N_1 + N_2 + N_4
\end{aligned} \tag{4.3}$$

where the index *j=1,2* corresponds to the 946 nm and 1064 nm lasers. Equations (4.1), (4.2) and (4.3) are similar to equations (3.2), (3.5) and (3.7) respectively. The main difference here is that there are now two stimulated

absorption terms in the saturable absorber rate equation, eq. (4.3), which corresponds to absorption by both lasers.

The rate equations described here makes an adiabatic approximation, where the change in photon flux density is assumed to be much slower than the cavity round trip time. In addition, diffraction of the pump and cavity beams are neglected. To be explicit, the integral $\iiint_{SA} r_c(r,z) r dr d\theta dz$ simply becomes $\pi {w_{SA}}^2 l_{SA} / \pi {w_c}^2 l_{cav}$; thus, spatial overlap between the two lasers inside the SA is not taken into account. Nonetheless, the numerical model provides valuable insight into the (slow) temporal dynamics of synchronized Q-switching, and help explain some anomalies in the experimental results, as will be described in the next section. It should be noted that the numerical modeling was performed by Peter Tidemand-Lichtenberg. The model description will be limited to only the extent that is needed to help explain the experimental results in a qualitative manner.

As an interesting aside, similar rate equations can be used to describe simultaneous dual-wavelength lasers [55-57], where the equations are coupled through the population inversion in the laser crystal, $d\Delta N/dt$. Using these equations, Shen [56] and Lin et al. [57] suggested controlling the relative losses and cavity lengths of the two lasers to achieve simultaneous dual-wavelength operation. Notably, Lin et al. set the following conditions that ensure the thresholds and build-up times for both lasers are equal [57]:

$$P_{th1} = P_{th2}; \quad \frac{d\phi_1}{dt} = \frac{d\phi_2}{dt} \tag{4.4}$$

where P_{th1} and P_{th2} are the threshold pump powers for each laser. If the two lasers are both four-level transitions, equation (4.4) simplifies into rather elegant requirements for the relative losses and cavity lengths:

$$\frac{\delta_{passive_1} + T_{out_1}}{\delta_{passive_2} + T_{out_2}} = \frac{\sigma_1}{\sigma_2}; \qquad \frac{L_1}{L_2} = \frac{\sigma_1}{\sigma_2} \tag{4.5}$$

Towards the end of this chapter, it will be shown that for synchronized lasers using separate gain crystals and a common saturable absorber, the conditions in eq. (4.4) may not be desirable for stable operation, and that an alternate approach for synchronizing passively Q-switched lasers is needed.

4.3 Experimental Results

Figure 4.3 illustrates the experimental setup.

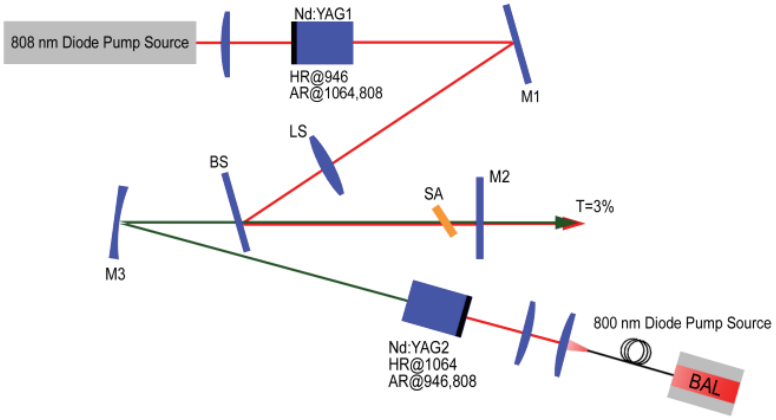

Figure 4.3 - Experimental setup for a Y-shaped cavity with a shared Q-switch between the 946 nm and 1064 nm lasers. Nd:YAG1 and Nd:YAG2 are the laser crystals for 946 nm and 1064 nm, respectively. SA is the saturable absorber.

The HR facet of Nd:YAG1, mirrors M1, BS and M2 form the 946 nm cavity, while the HR facet of Nd:YAG2, mirrors M3 and M2 form the 1064 nm cavity. The SA is a 0.97 mm thick Cr:YAG specified for 85% unsaturated transmission at 1064 nm at normal incidence. Taking into account the SA is oriented at Brewster's angle and using the absorption cross-sections published in [43], the unsaturated transmission at 1064 nm and 946 nm are 82% and 83% respectively. Similarly, using the excited state absorption cross-sections in [43], the saturated transmission are calculated to be 94% and 92% at 1064 nm and 946 nm respectively. M1, a plane folding mirror coated for high transmission at 808 nm and high reflection at 946 nm, is inserted to minimize feedback to the tapered diode pump source. BS is the coupling mirror coated for high transmission at 1064 nm and high reflection at 946 nm. M2 is the output coupler, coated for 3% transmission at both 1064 nm and 946 nm. M3, with a radius of curvature of r = -100 mm, is coated for high reflection at 1064 nm, and the intracavity lens, LS, with a focal length of 75 mm, is coated for high transmission at 946 nm.

The narrow spectrum, external cavity tapered diode laser, at 808.8 nm, used in the CW experiments, was used to pump the 946 nm laser. It has an M^2 of 1.4 and 5.7 for the fast and slow axis respectively, according to the second-

moments definition. After the optical isolators and focusing optics, 1.6 W of pump power was incident on the laser crystal (Nd:YAG1).

A fiber-pigtailed broad-area diode laser (LUMICS LU0808T045) was used to pump the 1064 nm laser. It has an NA = 0.15, a fiber core diameter of 105 μm, and is specified for up to 4.5 W output power. However, due to current limit of the diode driver, experimental data was collected only up to 3 W incident power after the coupling optics.

The single-pass pump absorption through the 3 mm long 946 nm laser crystal (Nd:YAG1) and the 5 mm long 1064 nm laser crystal (Nd:YAG2) were 90% and 47% respectively. The relatively low absorption in the 1064 nm laser crystal was due to a mismatch between the diode pump source spectrum and the absorption peak of Nd:YAG. The center wavelength of the broad area diode pump source is 801 nm, with a FWHM spectral bandwidth of 2.5 nm.

The mode sizes of the two lasers were optimized experimentally and are shown in Table 4.1 below:

Table 4.1 - Cavity and pump beam mode sizes for the 946 nm and 1064 nm laser

	946 nm	1064 nm
Pump diode mode size	59 μm (h) x 80 μm (v)	70 μm in both directions
Cavity mode size inside laser crystal	77 μm in both directions	88 μm (h) x 108 μm (v)
Cavity mode size inside SA	24 μm in both directions	72 μm (h) x 97 μm (v)

As described in Chapters 2 and 3, efficient Q-switching in a quasi-three-level laser requires two operating conditions: 1) a good overlap between the pump and cavity modes inside the laser crystal [12,14,35]. 2) a small cavity mode inside the passive Q-switch to achieve efficient bleaching. These imply that the 946 nm laser cavity is most efficient near the stability limit, where stability of the cavity itself is very sensitive to perturbation. Thus, an intracavity lens was used instead of a curved folding mirror to avoid astigmatism, which would have further reduced the stability region. The intracavity lens, LS, introduced an insertion round-trip loss of 1.9%.

Following the method reported in [69,73], the 946 nm laser cavity was made relatively long to ensure a good temporal overlap between the two pulses. The 946 nm cavity length was 37 cm, while the 1064 nm cavity length was

19 cm. These resulted in 200 ns and 45 ns FWHM pulse widths for the 946 nm and 1064 nm lasers, respectively.

The pulsed signals were separated using dichroic beamsplitters and detected using two Thorlabs PDA-255 photodiodes, each with a 7 ns rise time. The respective signals were then captured using a LeCroy Wavesurfer 104MXs-A oscilloscope with 1 GHz bandwidth.

The Q-switched mode-locking behavior of the 946 nm laser reported in the previous chapter is also present in the synchronized system. However, it did not appear to affect the synchronization, and since the subject of the current investigation is in synchronized Q-switching, this mode-locking behavior is not investigated in the current work.

Throughout the experiments presented here, the incident pump power of the 946 nm laser was held fixed at 1.6 W, while the pump power of the 1064 nm laser was varied.

4.3.1 General system performance

Stable locking of the two pulses was observed over a wide range of pump powers. Figure 4.4 illustrates the repetition rates of the two lasers. As a base-line comparison, repetition rates of the two free-running lasers were first measured individually with the other laser switched off. These are plotted in dashed lines.

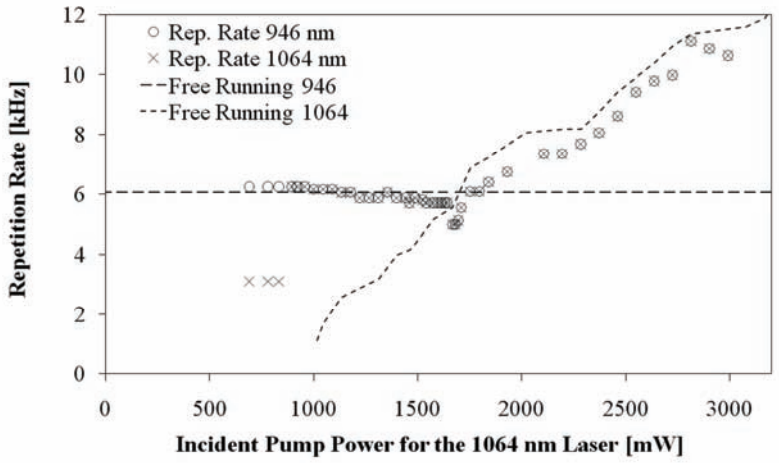

Figure 4.4 - Repetition rates of the synchronized system and of the respective free-running lasers at 946 nm and 1064 nm.

Repetition rates of the synchronized lasers are plotted in circles and crosses for the 946 nm laser and 1064 nm laser, respectively. It can be clearly seen that the repetition rates of the two lasers are stably locked up to 11 kHz, and that the threshold of the 1064 nm laser was reduced from 1.0 W incident pump power in the free-running case to 0.69 W in the synchronized system. The first three data points in Figure 4.4 indicate 2:1 synchronization, where the 1064 nm gain is so low that a 1064 nm pulse is only generated with every other 946 nm pulse. This is in agreement with previous reports [58,59]. It can be seen here, however, that the two lasers are locked together over a wide range of pump powers, with the 946 nm laser following the 1064 nm laser up to almost twice its natural free-running repetition rate.

Operation of the synchronized system can be divided into three regimes: 1) when the free-running repetition rate of the 1064 nm laser is below that of the 946 nm laser, the SA is bleached by the 946 nm photons before sufficient gain in the 1064 nm laser is accumulated; thus, in this case, the 946 nm pump power determines the repetition rate of the synchronized laser, and will be referred to as the master laser. 2) When the free-running repetition rate of the 1064 nm laser is higher than that of the 946 nm laser, the 1064 nm laser becomes the master laser. 3) When the free-running repetition rates of both lasers are matched, an unstable regime exists, where the 946 nm laser bleaches the SA first at times while the 1064 nm laser bleaches first at others. This unstable regime is narrow, within tens of mW of incident pump power, and will be described in greater detail in section 4.3.2.

Since the slave laser only starts to build up after the SA is bleached by the master laser, a small inherent delay between the two pulses is observed when the free-running repetition rates of the two lasers are not equal. This will also be described in section 4.3.2.

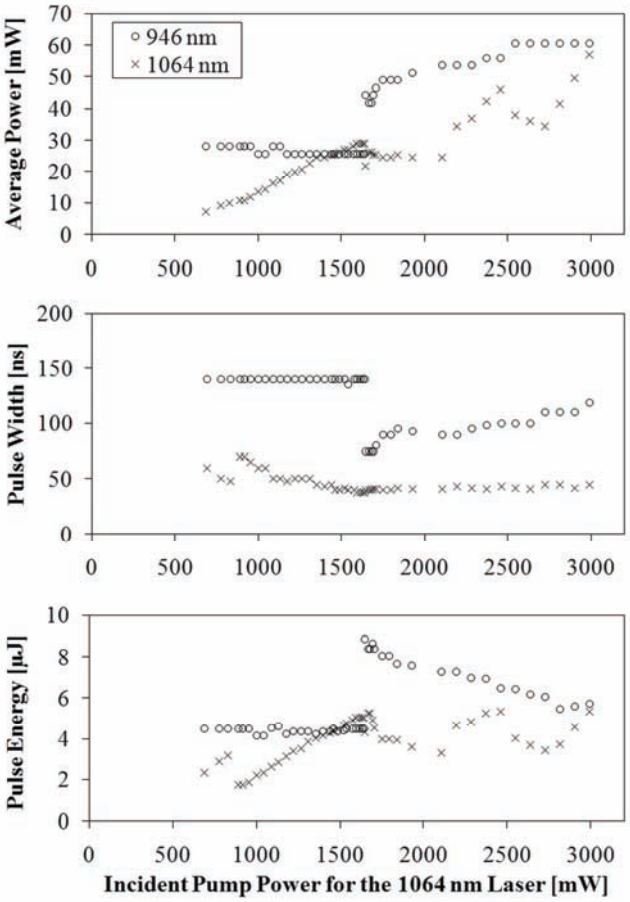

Figure 4.5 - Average power, Q-switch envelope width (FWHM), and pulse energy of the synchronized lasers.

When the 1064 nm laser becomes the master laser at ~1.6 W, both the average power and pulse energy of the 946 nm laser increased significantly, while the width of its Q-switch envelope decreased, as shown in Figure 4.5. The relatively significant increase in performance of the 946 nm laser is due to the quasi-three-level nature of the laser line, where for each photon sacrificed for bleaching the SA, the population inversion is reduced by two. When this burden is taken by the 1064 nm laser, the excess gain in the 946 nm laser crystal could then be converted into useful output.

The second dip in the 1064 nm average power (at ~2.6 W) was due to thermal lensing, which caused the 1064 nm laser cavity to become unstable in the horizontal direction. This was verified using a beam profiler, where wings in the horizontal directions were observed in the 1064 nm laser mode

at 2.6 W incident pump power. Higher order modes were observed when the pump power was further increased.

In [76], a video shows stable locking of the two lasers up to twice the natural free-running repetition rate of the slave laser (the 946 nm laser in this case). The abrupt change in the 946 nm output power when the 1064 nm laser became the master laser is also observed. Figure 4.6 shows the oscilloscope trace of the synchronized pulse trains when the 1064 nm laser pump power was at 3.0 W. The differences in the signals' peaks were due to the limited sampling rate of the oscilloscope.

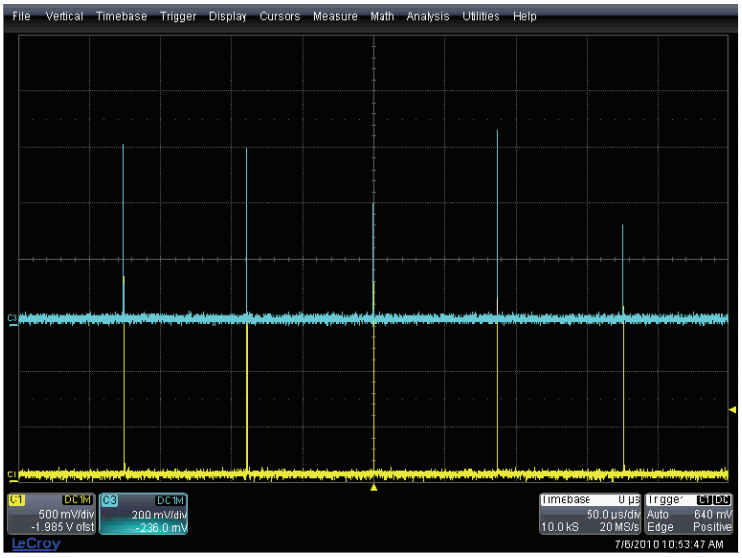

Figure 4.6 - Oscilloscope trace of the synchronized pulse trains at 3.0 W of 1064 nm laser pump power. The yellow and blue traces show the 946 nm and 1064 nm laser pulses, respectively.

4.3.2 Pulse delay and temporal overlap

Due to the unstable regime at around the switching point, a minimum delay between the two laser pulses was observed during stable operation. This delay is plotted in Figure 4.7 (a). A negative delay indicates the 1064 nm laser is lagging, while a positive delay indicates the 1064 nm laser is leading.

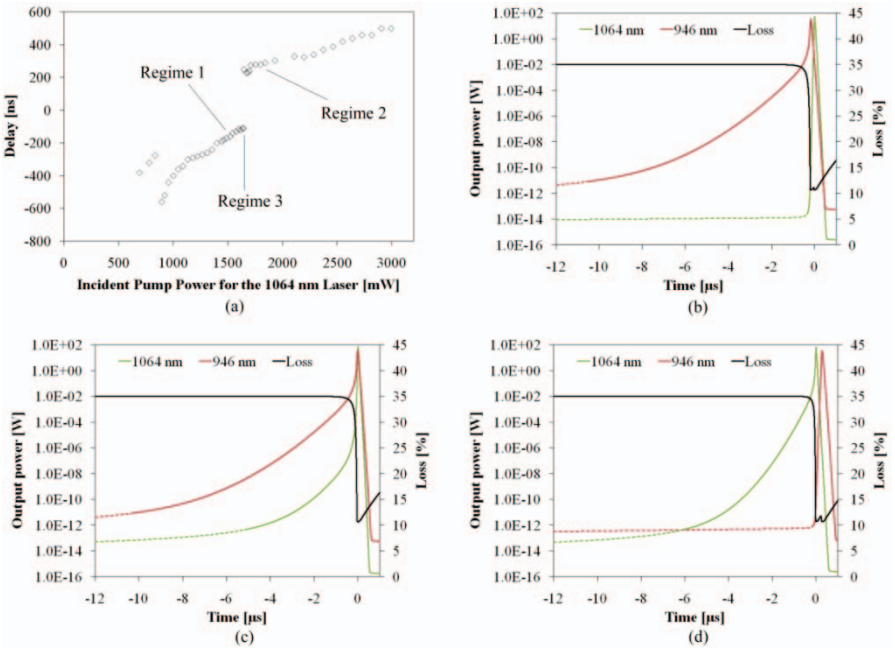

Figure 4.7 - (a) Relative delay between the two laser pulses as a function of 1064 nm laser pump power, with the 946 nm laser pump power held at 1.6 W. Qualitative plots of the pulse build-up and cavity losses are shown for (b) regime 1, (c) regime 3, and (d) regime 2 as functions of time. Dashed lines in (b)-(d) indicate when the lasers are below threshold.

At low pump powers, the instantaneous gain of the 1064 nm laser, when the SA is bleached by the 946 nm laser, is small, which leads to a slow build-up of the 1064 nm pulse and subsequently a long delay between the two pulses. As the 1064 nm laser pump power is increased, the instantaneous gain increases, and therefore the 1064 nm pulse build-up time decreases as a function of pump power, which in turn decreases the delay (regime 1). When the 1064 nm laser becomes the master laser, the two lasers switch roles and the 1064 nm pulse becomes the leading pulse. As the pump power is further increased, the two pulses start to move apart in time again (regime 2). This also explains the slow decrease in pulse energy and increase in the Q-switch envelope width for the 946 nm laser as the 1064 nm laser pump power is

increased beyond the switching point (see Figure 4.5). Regime 3 is characterized by an unstable and abrupt change in delay in the experimental data.

To better understand the physical mechanism responsible for the delay and in particular, the abrupt change in regime 3, numerical results from the model described in section 4.2 is shown in Figure 4.7 (b) – (d). It shows qualitatively the pulse build-up and cavity losses in the three regimes as functions of time. The absorbed pump power of the 1064 nm laser is increased by 100 mW in each subsequent plot, while the pump power of the 946 nm laser stays fixed.

It can be seen in regime 1 (Figure 4.7b) that the 1064 nm laser does not reach threshold until the SA is bleached by the 946 nm laser, thus the point at which the 1064 nm laser reaches threshold is well defined. In regime 2 (Figure 4.7d), the situation is reversed, and the 1064 nm pulse leads the 946 nm pulse. In regime 3 (Figure 4.7c), however, the free-running repetition rates of the two lasers are closely matched, and both lasers reach threshold before the SA is bleached. In this case, the photon flux for both lasers build up rapidly due to stimulated emission, and gain fluctuations that delay or advance the threshold on the order of microseconds will have a critical impact on the build-up time of the two pulses; thus, the theoretical minimum delay for stable operation depends on the jitter of the individual free-running lasers. Experimentally, the unstable regime 3 was observed to be very narrow, within tens of mW of incident pump power. The minimum delay with stable operation, observed experimentally, was 84 ns when the 946 nm laser was the master laser (regime 1) and 242 ns when the 1064 nm laser was the master laser (regime 2).

Reducing the 1064 nm mode size inside the SA, such that the horizontal beam waist radius matches that of the 946 nm laser (to 24 μm (h) x 80 μm (v)), reduced the minimum delay between the two pulses to 64 ns when the 946 nm laser was the master laser. Figure 4.8 shows the corresponding oscilloscope trace. The focusing lens of the 1064 nm pump beam was changed from 40 mm to 20 mm in this experiment to suppress lasing of higher order modes. Further reduction of the 1064 nm SA mode size was not possible due to physical limits with the current setup.

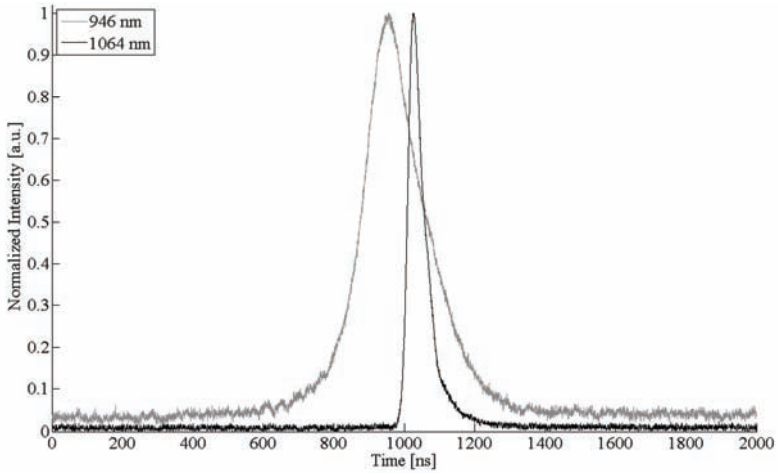

Figure 4.8 - Oscilloscope traces of the two pulsed signals, showing good temporal overlap - dark trace shows a 1064 nm pulse, light trace shows a 946 nm pulse. The overlap corresponding to the product of the two pulses was 79 % with respect to the best case scenario where no delay would be present.

By making one of the pulses relatively long compared to the other, good temporal overlap between the two could be achieved. It is reported in [69] that 40 ns of timing jitter in combination with a 250 ns long pulse resulted in less than 10% peak-to-peak fluctuation in the corresponding sum-frequency generation. In Figure 4.8, the FWHM pulse widths of the 946 nm and 1064 nm lasers were 200 ns and 45 ns respectively. Multiplying the two traces, and integrating the resulting product over time, the temporal overlap between the two pulse trains was calculated to be 79%. This was normalized against the best case scenario, where no delay between the two pulses would be present.

4.4 Summary and Future Work

To summarize, stable synchronized Q-switching between a quasi-three-level and a four-level laser has been demonstrated in an all passive approach. Stable locking of the two pulse trains was achieved over a wide range of pump powers. A minimum delay of 64 ns was achieved in stable operation, which translates into 79% temporal overlap when compared to the zero-delay scenario. The jitter observed here is comparable to the 40 ns jitter reported in an actively synchronized system [69], but a more detailed investigation into the relative timing jitter between the two laser pulses will be presented in next chapter.

For two lasers using separate gain crystals sharing a common Q-switch, there exists an optimal, stable operating point for minimal delay near the switching point. This occurs when the slave laser stays below threshold until the SA is bleached by the master. Furthermore, the slave laser should have a relatively fast build-up time so that it can "catch-up" to the master laser. This is in contrast to the conditions for simultaneous dual-wavelength oscillations previously reported for SDWL's [56,57].

Ideally, given the relatively weak transition at 946 nm, the 1064 nm laser should act as the master laser, opening the Q-switch for the 946 nm laser. In this case, the 1064 nm laser pulse should be made long when compared to the 946 nm pulse. However, due to the mode size constraints mentioned above, this was not possible with existing components. A possible improved design that allows for shorter cavity lengths for both lasers is suggested in Figure 4.9. The shared SA is placed close to the beam waist, while the laser crystals could be placed further away for good energy storage. The linear cavities would give half the current cavity lengths. However, the design is potentially limited by the practical issue of how well can the anti-reflection and high-reflection coatings on the laser crystals be manufactured.

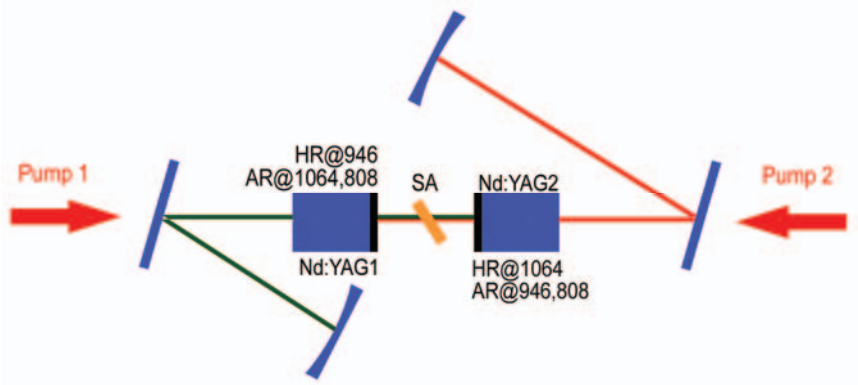

Figure 4.9 - Possible cavity for future experiments that allows for shorter cavity lengths and places the saturable absorber close to the beam waist.

5. Timing Jitter of Passively Synchronized Q-switching

5.1 Background

One criticism of passively Q-switched lasers has often been that they are too unstable for practical applications due to the relatively large timing jitter when compared to active systems. Indeed, in the previous chapter, the passive synchronization is unstable in a narrow operating range – when the free-running repetition rates of the two lasers are equal (regime 3 in Figure 4.7a). If the lasers are operated in this unstable regime, it would be difficult to maintain stable sum-frequency conversion due to the large fluctuation in temporal overlap. However, it may be of interest to quantify exactly how "unstable" is a passively synchronized system. This is particularly important for operations in regimes 1 and 2, and would then allow one to evaluate the cost – in terms of both performance and price – when choosing to use a passive system over an active one, or vice versa.

The dominant cause of timing jitter in a single passively Q-switched laser has previously been attributed to pump power fluctuations [77] and noise from amplified spontaneous emission [78]. Subsequently, jitter reduction methods that increases gain modulation [77], loss modulation [78-80], or self-injects a seed pulse [81] at close to the laser's repetition rate have been proposed. In particular, direct bleaching of the saturable absorber (SA) by a laser diode bar resulted in a 12 times decrease in timing jitter [80], while a self-injection seeded microchip laser achieved a 600 times reduction [81]. Loss modulation was applied at a slightly higher repetition rate than the laser's natural free-running repetition rate, just before the laser reaches threshold [79,80].

Both actively and passively synchronized Q-switching have previously been demonstrated and reviewed in section 4.1.1. However, to the author's knowledge, no detailed work has been done on timing jitter in synchronized Q-switching; in particular, the relative timing jitter between the two synchronized pulse trains. Zhang et al. demonstrated a quasi-three-level and four-level simultaneous dual wavelength laser (SDWL) at 1064 nm and 946 nm, but did not provide temporal measurements [67]. Tsai et al. reported on a four-level Ytterbium laser at 1064 nm gain-switched by a quasi-three-level laser at 976 nm in an all-fibre system, and quoted a relative timing jitter of 40 ns, defined as one standard deviation in the experimental measurements [68]. Herault et al. synchronized a quasi-three-level laser at 912 nm and a

four-level laser at 1063 nm using two active Q-switches, and reported a timing jitter of 40 ns, and a 10% fluctuation in the resulting sum-frequency generation peak power [69]. Unfortunately, the authors did not state how the jitter or fluctuations were defined or measured.

In this chapter, an experimental investigation into the relative timing jitter between two passively synchronized lasers is presented. In particular, the experimental setup described in Chapter 4 is considered. Detailed measurements on the timing of the two pulses, and on the pulse-to-pulse jitter are presented. Using the same rate equations described in section 4.2, qualitative but detailed performance characteristics can be modeled for both the delay and timing jitter. Towards the end of the chapter, conclusions are drawn regarding the performance penalty of using a passive system over an active system.

5.2 Experimental Results

For convenience, the experimental setup is illustrated again here.

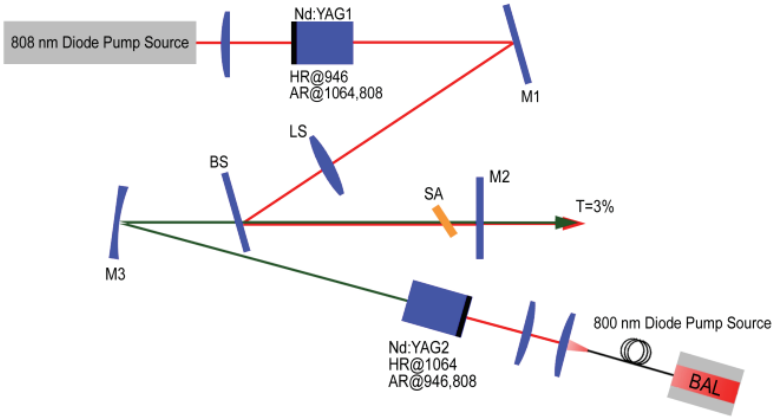

Figure 5.1 - Experimental setup for a Y-shaped cavity with a shared Q-switch between the 946 nm and 1064 nm lasers. Nd:YAG1 and Nd:YAG2 are the laser crystals for 946 nm and 1064 nm, respectively. SA is the saturable absorber.

The detailed coating specifications and cavity parameters can be found in section 4.3. The high reflection facet of Nd:YAG1, mirrors M1, BS, and M2 form the 946 nm laser cavity, while the high reflection facet of Nd:YAG2, mirrors M3 and M2 form the 1064 nm laser cavity. BS is the coupling mirror coated for high transmission at 1064 nm and high reflection at 946 nm. Synchronized Q-switching is achieved by placing one saturable absorber (SA) in the common section between mirrors BS and M2. The 946 nm laser cavity was made relatively long to ensure its pulses are long when compared to the 1064 nm pulse widths, which translates into better temporal overlap between the two pulse trains [69,73]. The cavity lengths were 37 cm and 19 cm for the 946 nm and 1064 nm lasers respectively, and the resulting pulse widths (FWHM) were 200 ns and 45 ns respectively. Incident pump power of the 946 nm laser was held fixed at 1.6 W, while incident pump power of the 1064 nm laser was varied.

Following the convention of laser manufacturers and the measurements reported in [68,80,81], timing jitter in this thesis is defined as the root-mean-square deviation from the mean, or one standard deviation. Statistical measurements of the relative delay between the 1064 nm pulses and 946 nm

pulses are obtained over 1000 samples. It will be confirmed below that the timing jitter follows a Gaussian distribution.

Figure 5.2 (a) and (b) show, respectively, the relative delay and timing jitter between the two lasers as a function of the 1064 nm laser incident pump power. As described in section 4.3.2, the 1064 nm laser is lagging the 946 nm laser when its pump power is below the switching point at 1.6 W. It will therefore be referred to as the slave laser in this operating regime, while the 946 nm laser is the master laser. When the 1064 nm laser pump power is above the switching point, it becomes the leading, master laser. The delay between the two pulse trains is the smallest at the switching point, when the free-running repetition rates of the two lasers are equal. However, as analogous to the jitter reduction techniques reported in [79,80] for a single laser, the jitter becomes significantly large if loss modulation (by the master laser in this case) is equal to the slave laser's free-running repetition rate – or to be precise, when the free-running repetition rates of both lasers are equal. The temporal dynamics of this operating regime is described in section 4.3.2 – in particular, both lasers are above threshold when the SA is bleached; thus, small changes in the photon flux, amplified by stimulated emission, have a large impact on the timing and consequently, on the relative delay, between the two pulses. Conceivably, this instability could be avoided in actively synchronized systems if the active Q-switch is cycled at a higher repetition rate than the free-running repetition rates of both lasers.

The minimum jitter on either side of the switching point in Figure 5.2 (b) then corresponds to the optimal operating point in the passive system, where both the delay and jitter would be the lowest for stable operation. When the 946 nm laser is the master laser, the minimum relative delay and timing jitter observed was 110 ns and 9 ns, respectively. While the authors in [69] did not state how the timing jitter was defined in their actively synchronized system, the 9 ns standard deviation reported here is comparable to the 40 ns reported in [69] if either a four-sigma or a six-sigma definition is assumed. As will be shown below, the timing jitter follows a Gaussian distribution; thus, these definitions correspond to 96% or 99.7% probability respectively.

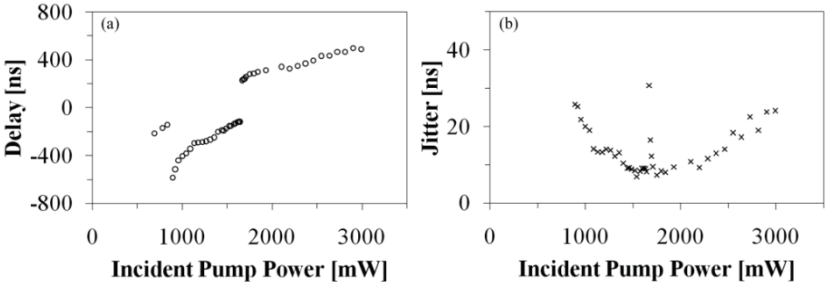

Figure 5.2 - Experimental data of (a) delay and (b) timing jitter as a function of 1064 nm laser pump power.

In [82], a video shows the change in the delay statistical distribution as the 1064 nm laser pump power is increased. It can be clearly seen how the delay and timing jitter both change as a function of pump power.

To confirm the experimental results with theoretical rate equations, the numerical model described in section 4.2 could be used again. The theoretical delay and the relative jitter between the two pulses are shown qualitatively in Figure 5.3 (a) and Figure 5.3 (b), respectively. The 946 nm laser absorbed pump power was varied by 0.05% while the 1064 nm laser absorbed pump power was varied by 0.5%. The smaller fluctuation of the 946 nm laser pump power can be justified by the narrow spectrum pump source used. It can be seen that the steep slope in the delay curve and the minimum jitter observed at around the switching point are well matched with the experimental data. The inset of Figure 5.3 (b) shows the full scale of the timing jitter numerical results, where it can be seen that the large timing jitter at the switching point increases to 150 ns. This was not observed in the experiments possibly due to the high sensitivity in the unstable region, and the difficulty in maintaining the laser pump power at exactly the switching point.

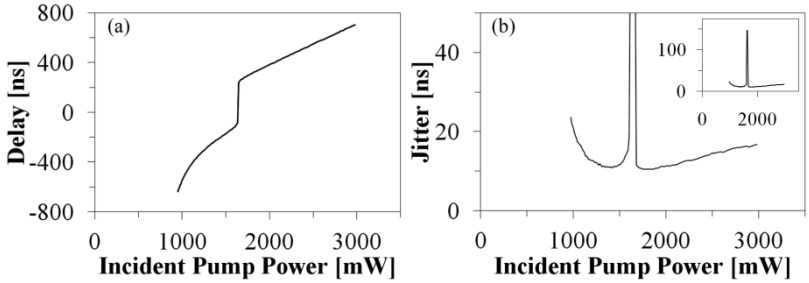

Figure 5.3 - Numerical model of (a) delay and (b) timing jitter as a function of 1064 nm laser pump power.

To investigate the increase in timing jitter when working with passively synchronized systems, as opposed to active systems, one can examine the relative timing jitter of the two lasers as a function of the pulse-to-pulse timing jitter in the master laser. This is shown in Figure 5.4 (a), where the inset shows graphically the measurement that is taken. The incident pump power of the 1064 nm laser was 1.58 W; thus the 946 nm laser was the master laser at this operating point. Projecting the data points in Figure 5.4 (a) onto the vertical axis, a histogram of the relative delay can be obtained, and is shown in Figure 5.4 (b). The mean relative delay and timing jitter between the two pulse trains were 119 ns and 9 ns, respectively. Similarly, the master laser pulse-to-pulse separation and jitter were 202 μs and 4 μs respectively, and the corresponding histogram is shown in Figure 5.4 (c). The solid lines in Figure 5.4 (b),(c) show good fits to the Gaussian distribution.

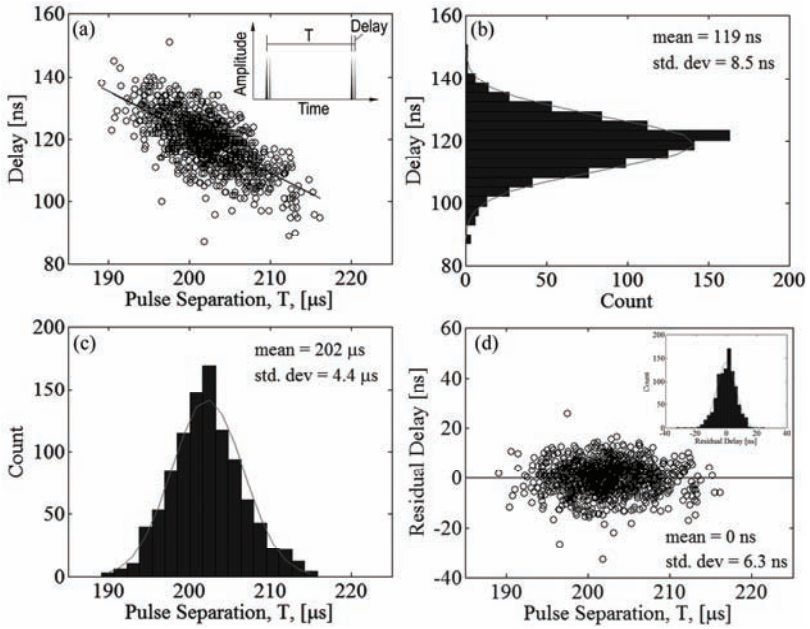

Figure 5.4 - (a) Correlation of pulse separation of the master laser and the delay between the two lasers at a fixed pump power. Inset depicts the measurement that was carried out, while the solid line shows the least square fit. Projection of the data points onto the vertical axis is shown as a histogram in (b), while projection of the data points onto the horizontal axis is shown as a histogram in (c). The slope of the least square fit is subtracted from the experimental data, and the resulting residual jitter, with the effect of the master laser's jitter removed, is shown in (d). Solid lines in (b) and (c) show the Gaussian fits.

The solid line in Figure 5.4 (a) is the least-square fit, which shows the correlation between the pulse-to-pulse separation and the relative delay between the two lasers. This was found to be 1.3 ns/μs. Subtracting this fitted line from the experimental data removes the effect of pulse-to-pulse jitter in the master laser and maps the delay onto the horizontal axis. This is shown in Figure 5.4 (d). By projecting the data points in Figure 5.4 (d) onto the vertical axis, the residual relative jitter is plotted as a histogram in the inset. The residual relative jitter between the two lasers, without the effect of pulse-to-pulse jitter in the master laser, is 6 ns.

Figure 5.4 (d) implies that, if the pulse-to-pulse jitter in the master laser can be well controlled, as in the case of actively Q-switched systems, the expected relative jitter between the two lasers can be no better than 6 ns. This is the lower limit set by pump power fluctuations and noise from amplified spontaneous emission. Comparing this value to the 9 ns relative timing jitter currently observed in the experimental data, shows the penalty that is being paid by using an all passive system.

5.3 Overlap Stability

The previous section describes the effect that pulse-to-pulse jitter in the master laser has on the relative jitter between the two lasers, and the performance penalty incurred by using a passively synchronized system, as opposed to an active system. It could then be interesting to determine how the relative timing jitter translates into fluctuations in temporal overlap.

Using the same experimental setup, but with a reduced 1064 nm mode size in the SA, the overlap fluctuations was measured. The 946 nm laser was acting as the master laser, and an average delay of approximately 80 ns was observed. Due to the large data set, it was not practical to perform post-processing, and LabView was used to calculate the product of the two oscilloscope traces and integrate the product over one sweep (~2 μs) in real time. The experiment was carried out over 13 minutes and 20 seconds, and 10 000 traces were acquired. Figure 5.5 (a) shows the integrated product as a function of time, with the mean normalized to 1, while Figure 5.5 (b) shows the corresponding histogram. The standard deviation in the overlap measurements was 0.19. The sharp drops in the temporal overlap (to ~0.2) is due to the 1064 nm laser briefly becoming the leading, master laser, and the synchronization became unstable. Between the 6 minute mark and the 10 minute mark, the lab was vacated, and the synchronization was relatively stable, which suggests that the stability could be improved by building an enclosure around the laser. Alternatively, the lasers could be operated slightly further away from the switching point. This would improve stability at the expense of a reduced temporal overlap.

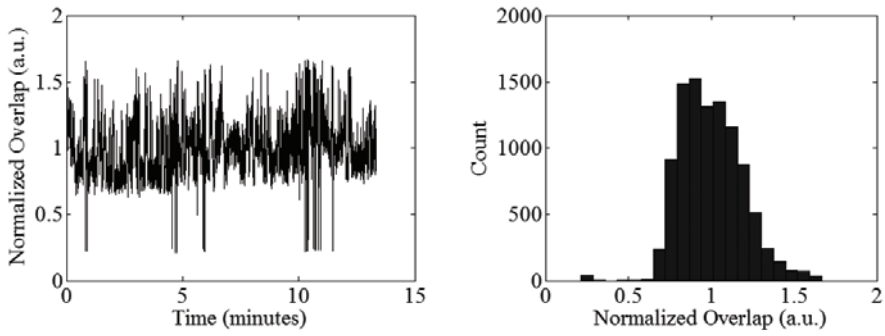

Figure 5.5 - Stability of the temporal overlap between the two synchronized pulse trains. Temporal fluctuations is shown on the left, while the corresponding histogram is plotted on the right.

5.4 Summary and Future Work

Experimental investigation into the relative timing jitter of passively synchronized Q-switched lasers has been presented. Results from a numerical model supported the experimental results and showed the detailed features that were observed experimentally. While the pulse-to-pulse jitter in the individual laser was on the order of μs, the relative jitter between the two lasers was in the ns range. In particular, relative jitter between the two lasers would be the lowest at just before and after the unstable regime where the free-running repetition rates of the two lasers are equal. These correspond to the optimal operating point where both the relative delay and timing jitter are the lowest for stable operation. Relative timing jitter between the passively synchronized lasers was 9 ns at the best operating point, and increased significantly at the switching point. If the effect of pulse-to-pulse jitter in the master laser is removed, the residual jitter is 6 ns, which is the lower limit determined by pump power fluctuations and amplified spontaneous emission.

Naturally, the most promising and exciting work to be done here is to perform sum-frequency generation of the two beams, and to measure directly the efficiency and stability of the final system.

Performing intracavity non-linear frequency conversion has the advantage that the peak power available is significantly higher, and that a beam waist is already formed near the SA, where the non-linear crystal could be placed – leading to a more compact design. However, intracavity conversion also changes the dynamics of the laser cavities, since the non-linear loss is also time dependent and losses for both lasers are increased. If critical phase-matching is used in an intracavity setup, spatial walk-off may reduce the spatial overlap between the two lasers inside the SA, decreasing the coupling between the two lasers, thus potentially increasing the build-up time and relative delay between the two pulses. This is particularly critical for the quasi-three-level laser as photons used to bleach the SA is expensive in terms of population inversion.

6. Applications

6.1 Introduction

Spontaneous emission, or fluorescence, is an undesirable process in laser systems; however, if coming from a biological tissue, the fluorescence spectrum can provide valuable information about the composition of the sample. Obtaining such information in a biomedical image, either by wide-field imaging or from point-by-point B-scans, falls into the field of fluorescence imaging.

Preliminary experiments were carried out to evaluate the feasibility of using a pulsed DPSS laser for fluorescence imaging in the clinical setting. These include using compact blue and UV lasers to excite the fluorophores, as well as demonstration of a novel ring laser which could potentially suppress the Q-switch mode-locking behavior in the 946 nm laser. In section 6.2, a CW blue laser at 404 nm was used as the excitation source for fluorescence imaging with an exogenous fluorophore. In section 6.3, preliminary clinical results from an autofluorescence diagnostic experiment using a pulsed 355 nm UV laser is presented. Finally, in section 6.4, a novel ring laser that uses non-linear optics to enforce unidirectional single-mode operation, which could potentially suppress Q-switch mode-locking in the 946 nm laser, is described.

6.2 Quantification of Photosensitizer using Fluorescence Imaging

Determination of photosensitizer concentration is of great interest in photodynamic therapy (PDT) and in pre-clinical studies, because therapeutic outcome is critically dependent on photosensitizer concentration and on the corresponding light dosimetry. Fluorescence imaging is a promising method that could be used to determine photosensitizer concentration in vivo and in real-time. However, due to differences in optical properties between different tissues, absorption at the excitation and emission wavelengths, and noise from tissue autofluorescence, the fluorescence signal tend to become uncorrelated with fluorophore concentration in turbid media. Fluorescence ratiometric techniques and fluorescence diffuse optical tomography have been used to measure photosensitizer concentration in vivo. However, the former does not take into account absorption of the excitation light and of the emitted fluorescence, while the latter tend to be computationally expensive. The approach proposed in [83] uses white Monte Carlo (WMC) simulations to generate a correction factor that accounts for absorption at both the excitation and emission wavelengths. To obtain the fluorescence concentration in tissues with different optical properties, it is a matter of multiplying the captured image with the appropriate correction factor from the WMC simulation, which greatly reduces computation time:

$$F_{image}\,\Delta \propto Conc \tag{6.1}$$

where F_{image} is the averaged fluorescence intensity over the region of interest – the phantom or the organ in this case, Δ is the correction factor obtained through white Monte Carlo simulations, and *Conc* is the concentration of the photosensitizer.

A continuous-wave 404 nm laser, based on direct frequency-doubling of an 808 nm tapered diode laser, was used to support an animal fluorescence imaging experiment using an exogenous photosensitizer. The photosensitizer, FosPeg®, contains the active ingredient meso-tetra hydroxyphenyl chlorine (mTHPC), or temoporfin, which has a fluorescence emission peak at 652 nm when excited at 405 nm. Figure 6.1 below illustrates the absorption and emission spectra of mTHPC.

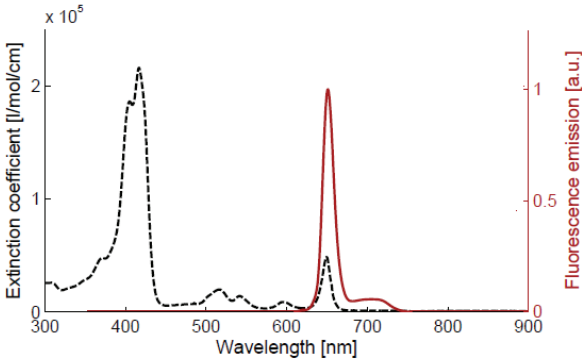

Figure 6.1 - Extinction (absorption) coefficient (dashed line) and fluorescence emission spectrum (solid line) of mTHPC in ethanol when excited with 405 nm radiation. Source: Xie et al. [83].

Although not strictly a DPSS laser, the CW laser used in this experiment had similar form factor and power requirements. The experimental set up was built by a previous PhD student at Lund University, Jesper Holm Lundeman, and detailed description of the laser can be found in [84,85]. Similar to the tapered diode pump source used in Chapter 2, an external Littrow grating provided feedback to the 808 nm tapered diode. The tapered diode laser cavity was then mode-matched to an external ring cavity containing the PPKTP crystal, where second harmonic generation into 404 nm takes place. The ring-cavity is resonant at 808 nm, and a piezo is attached to one of the mirrors to tune the cavity into and out of resonance to provide pulsed output when necessary. Figure 6.2 below shows the laser schematic.

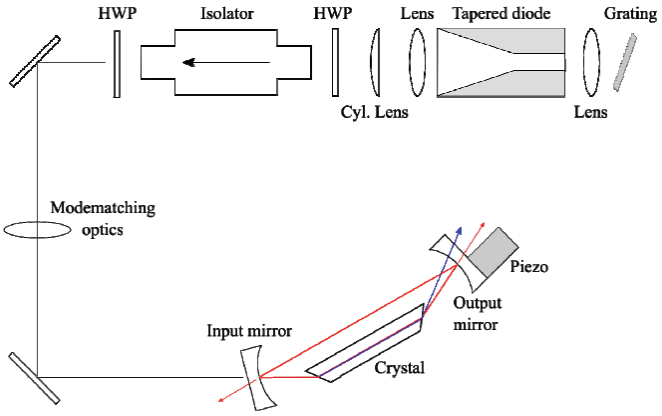

Figure 6.2 - Schematic of the laser used for generating 404 nm light. Source: Lundeman et al. [84].

During CW operation, the peizo is supplied with a DC voltage to maintain a fixed position. However, due to thermal expansion in the non-linear crystal, the ring cavity occasionally falls out of resonance, and mode-matching with the diode pump beam is lost. While it is possible to compensate for this using an electronic locking circuit at low pump powers, stronger thermal effects at high pump power introduces hysteresis that prevent effectiveness of the circuit. Thus, the CW laser was operated slightly away from perfect phase-matching to increase stability.

6.2.1 Experimental Results

Two measurements were made to test the WMC model. First, twenty homogenous liquid phantoms were prepared using water, intralipid, Indian ink, and Rhodamine 6G. The Indian ink acts as the absorber, while the Rhodamine 6G is a fluorescent dye with similar emission spectrum as mTHPC. Second, fluorescence imaging was performed on thirty mice following the guidelines established by European Council Directive 86/909/EC and approved by the Thüringer Landesamt für Lebensmittelsicherheit und Verbraucherschutz, Weimar. Fospeg® was injected into the tail vein of the mice and the animals were sacrificed at various times after photosensitiser injection. The organs were then excised for fluorescence imaging, after which they were flash frozen until high performance liquid chromatography (HPLC) was performed to determine the precise photosensitizer concentration.

Figure 6.3 shows the phantom measurements, and the inset shows the same plot in a semi-log scale. The different markers correspond to the raw fluorescence signals obtained directly from the images with different Indian ink concentrations (different absorption coefficients), while the circled data points show the fluorescence intensity after the light-absorption correction by WMC. It can be seen that the correlation between the fluorescence intensity and fluorophore concentration is dramatically improved after the correction.

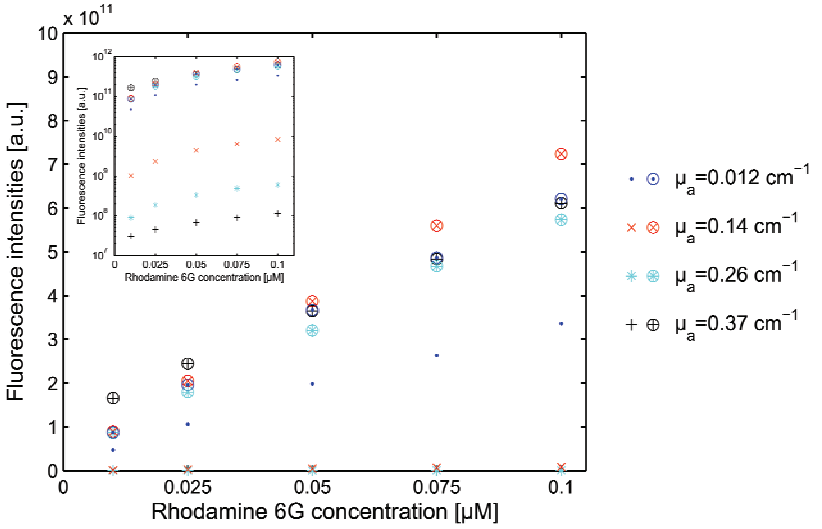

Figure 6.3 - Correlation between fluorescence intensity and fluorophore concentration in phantom measurements. Markers show the raw fluorescence intensity measured directly from the images, while circled data points show the fluorescence intensity after the light-absorption correction by WMC simulation. Inset shows the same plot in a semi-log scale. Source: Xie et al. [83].

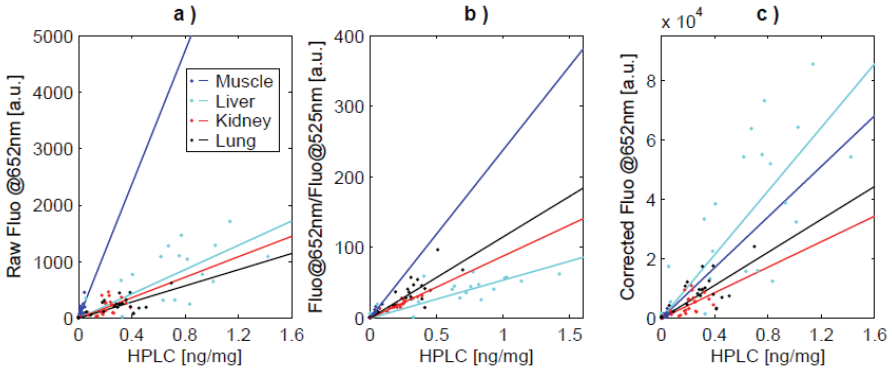

Figure 6.4 - Correlation between fluorescence intensity and fluorophore concentration measured in various excised organs. (a) shows the fluorescence intensity at 652 nm, (b) shows the ratioed fluorescence intensities at 652 nm / 525 nm, and (c) shows the 652 nm fluorescence intensity after the light-absorption correction. Source: Xie et al. [83].

Figure 6.4 shows the correlation between the averaged fluorescence intensity at 652 nm and the concentration measured by HPLC. It can be seen that the correlation here, indicated by the deviation of the data points from the linear fitted lines, is less reliable. Since optical properties for murine organs

reported in the literature seem to vary significantly, this is possibly due to uncertainties in the optical parameters used in the WMC simulation. Another issue that could affect the fluorescence measurement is the generation of autofluorescence by endogenous fluorophores inside the tissue when excited by UV or blue radiation. The autofluorescence signal has a broad spectrum that slightly overlaps the drug fluorescence signal and increases the noise floor. In Figure 6.4 (b) the ratio of the fluorescence at 652 nm and 525 nm is taken to suppress the effect of autofluorescence noise, where one could clearly see the improvement in correlation, confirming the presence of autofluorescence.

6.2.2 Summary and Outlook

In conclusion, using a compact 404 nm CW laser as the excitation source, determination of photosensitiser concentration using fluorescence imaging seem promising. While excellent correlation was achieved in the phantom measurements, the animal measurements seem to suffer from autofluorescence noise, and uncertainties in the optical properties reported in the literature. To improve reliability of the light-absorption correction method, future work is needed to determine the scattering and absorption coefficients for various organs more precisely and to circumvent the effects of autofluorescence.

6.3 Autofluorescene Imaging: Clinical Trial

One of the main motivations of the current thesis is the application of skin cancer diagnostic using fluorescence imaging, and a pulsed UV laser as the excitation light source. Fluorescence imaging provides a powerful diagnostic tool in monitoring treatment progress in photodynamic therapy (PDT) and in differentiating between malignant and benign lesions non-invasively prior to treatment. The technique is relatively economical, non-invasive, and provides information in real-time. While exogenous fluorophores exist, they generally require uptake of the photosensitizer, and the patient may need to avoid exposure to light for a period of time before and after the procedure. By taking advantage of endogenous fluorophores that are naturally found in our bodies, autofluorescence imaging is a promising diagnostic/screening tool for differentiating between different types lesions without prior preparation on the patient.

While the specific endogenous agents responsible for autofluorescence are not fully understood so far, it has been suggested that it could be due to collagen cross-links, elastin, NADH, and/or keratin [86]. Using a high pressure mercury lamp in combination with a bandpass filter at 366 nm, Lohmann et al. reported a fluorescence peak at 475 nm and a possible shoulder at 445 nm, which may be attributed to the fluorescence peak of NADH and NAD respectively [87]. Lohmann et al. suggested that the relative fluorescence intensities between healthy skin and the lesion area could be used to differentiate between a mole and a melanoma. Using a high pressure Xe-Hg lamp, and an algorithm based on that proposed by Lohmann et al., Chwirot et al. reported a clinical study achieving 82.7% sensitivity and 59.9% specificity for detecting melanomas in dark room conditions [86]. Troyanova et al. presented autofluorescence spectra of benign and dysplastic nevi and malignant melanoma using a nitrogen laser at 337 nm [88]. In a separate publication, Borisova et al. reported on autofluorescence spectra of basal cell carcinoma (BCC), squamous cell carcinoma (SCC), keratoacanthoma, and benign skin lesions using LED's at various wavelengths as excitation light source [89].

In a collaboration between DTU Fotonik, Lund University Department of Physics, Lund University Department of Dermatology, and Lund University Department of Oncology, a synchronized gated detection system has been put together for a clinical trial on autofluorescence imaging of pigmented skin lesion. A compact, diode-pumped, pulsed UV laser at 355 nm was built

and integrated with a tunable liquid crystal filter with gated detection, which increased the signal-to-noise ratio to the extent that imaging in ambient room light is possible. Pigmented skin lesions are targeted as they are difficult to diagnose without the use of histopathological methods. Sixteen patients participated in the clinical studies and the resulting autofluorescence images, as well as the corresponding histopathological results are presented.

6.3.1 Gated Detection System

The synchronized detection system is described below and is illustrated in the block diagram in Figure 6.5. The pulsed UV laser at 355 nm delivers 10 ns FWHM pulses at a repetition rate of 5 kHz through a 50 m long multimode fiber, which also serves as an optical delay line that accommodates the response time of the electronic components. Shutter 2 acts as the detection gate and is triggered by residual 1064 nm light (also at 5 kHz) that is coupled out through a separate port in the laser. The 1064 nm optical pulse train is converted into an electronic signal by a fast photodiode, which then goes to an electronic delay circuit that is used to fine-tune the temporal overlap between the UV light pulse and the shutter trigger signal during system calibration.

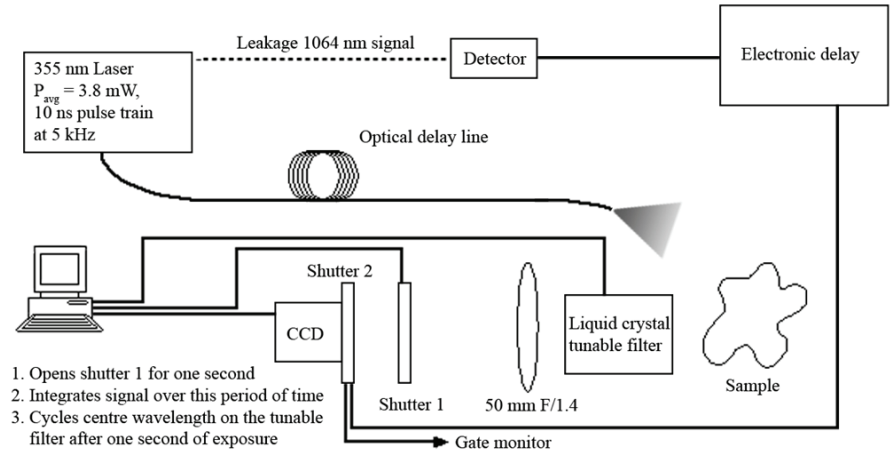

Figure 6.5 - Block diagram for the gated detection system used for autofluorescence clinical trial

The images are captured using a CCD camera (iSTAR DH734-18F-75) that comes with a proprietary PCI analog-to-digital (ADC) converter. The iSTAR CCD has an integrated optical intensifier on the front side, denoted as shutter 2 in Figure 6.5, that is controlled by the ADC and acts as the detection gate. Thus, the 5 kHz repetition rate is limited by the response time of shutter 2.

An external mechanical shutter, shutter 1 in Figure 6.5, is used to control the exposure time of each image taken, which is set to one second during the clinical trial. The tunable filter used is a VariSpec VIS from CRi with a bandwidth of 20 nm, and a tuning range from 400 nm to 720 nm, and is connected to a computer, which cycles through the pass-band wavelengths after an image has been taken. Thus, the pseudo-code that is running on the computer controlling the ADC is as follows:

1. Set the passband of the VariSpec to 400 nm
2. Cycle shutter 2 whenever a trigger is received (at ~5kHz)
3. Open shutter 1 for one second
4. Integrate the signal received on the CCD
5. Close shutter 1
6. Set the Varispec to the next passband and repeat steps 3-5

An exposure time of one second corresponds to integrating over approximately 5000 frames for each fluorescence image at a particular wavelength, with each frame being illuminated by a 10 ns FWHM laser pulse. Fluorescence images are taken at seven wavelengths: at 420 nm, 440 nm, 460 nm, 480 nm, 500 nm, 560 nm and 580 nm.

The target is imaged onto the CCD using an off-the-shelf 50 mm F/1.4 camera lens.

6.3.2 Pulsed UV Laser

The UV laser is a diode-pumped Nd:YAG 1064 nm Q-switched laser, frequency-tripled to 355 nm. Its schematic diagram is illustrated in Figure 6.6. The pump diode (RPMC LDX-3415-808, LD1 in Figure 6.6) produces 4 W of optical power at 808 nm when pumped at a current of 3.5 A. However, it was operated at approximately 3.1 A during the clinical trials to achieve a repetition rate of 5 kHz, the maximum allowed by the optical intensifier (Shutter 2 in Figure 6.5).

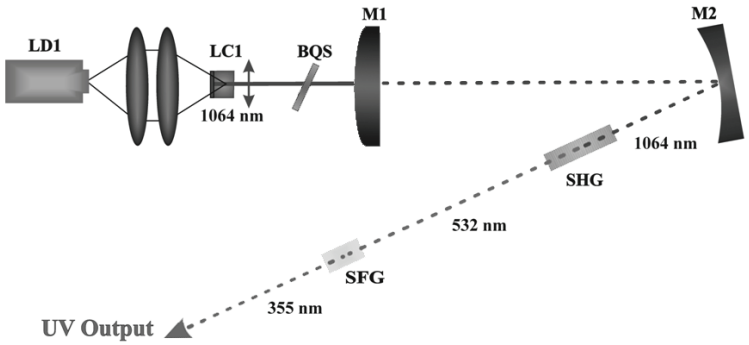

Figure 6.6 - Schematic of the frequency-tripled Nd:YAG laser at 355 nm used for the clinical trial.

The 5 mm long Nd:YAG crystal is placed in a 30 mm long optical resonator with a Brewster-cut Cr:YAG saturable absorber that gives 20% small signal absorption. Transmission of the output coupler (M1 in Figure 6.5) is 80% at 1064 nm. This gives approximately 121 mW of average power at 1064 nm, corresponding to 2.5 kW of peak power at 1064 nm. The laser beam is then focused into a PPKTP and a BBO crystal for second-harmonic generation and third-harmonic generation respectively. Mirror M2, with a curvature of 75 mm, was used such that a beam waist of approximately 100 μm is formed at the midpoint between the two crystals, placed approximately 20 mm apart. The PPKTP crystal is temperature-tuned so that approximately half of the 1064 nm light is converted into its second-harmonic at 532 nm. Sum frequency mixing between the residual 1064 nm and the generated 532 nm power then resulted in an average power of 3.8 mW at 355 nm, corresponding to a peak power of 76 W. Coupling losses and attenuation associated with the optical fibre has not been measured during this clinical trial, but it is observed that sufficient UV light is produced to achieve a one-second exposure time.

6.3.3 Calibration

To ensure a good temporal overlap between the illumination light pulse and the opening of shutter 2, a second fast photodiode (Melles Griot 13DAH001), with a rise time of less than 1 ns, is placed at the output of the optical fibre to monitor arrival of the UV pulses. The electronic delay is then adjusted, which in turn controls the timing of shutter 2. The photodiode signal is monitored on an oscilloscope, while the state of shutter 2 is monitored through a gate monitor signal from the iSTAR ADC. Shutter 2 is configured to remain open for 30 ns after it has been triggered, and the

electronic delay is adjusted such that the peak of the UV pulse arrives 15 ns after the shutter is opened. The Melles Griot photodiode is only used during calibration and is not used during normal operation of the laser.

6.3.4 Post-processing

To obtain consistent fluorescence signals with different scattering properties across different patients and to increase sensitivity, the fluorescence images are presented as a ratio of the fluorescence images at different wavelengths. Specifically, the fluorescence image at 580 nm is divided by the image at 460 nm, and a second ratioed image is produced using the signal at 440 nm divided by the signal at 500 nm. This in effect probes the fluorescence spectra of the different types of lesions at the four wavelengths. In principle, since fluorescence images at 7 wavelengths were captured, 21 combinations are possible. In this preliminary report, the mentioned wavelengths are chosen as they seem to provide the best contrast. Furthermore, to suppress the effects of hot pixels, the ratioed images are plotted in a log scale, in dB, using false colors.

6.3.5 Preliminary Results

By integrating over approximately 5000 frames per fluorescence image, sufficient signal could be collected in ambient room light to produce the ratioed images. Preliminary results show good contrast in six patients, while images from another six patients were not of good quality due to movement of the patient, out of focus, or hard-to-access areas, and four images showed poor contrast, which may be attributed to insufficient excitation light or lack of fluorophores in the lesion. Table 6.1 shows the patient data (age, sex, location of tumour and the corresponding histopathological diagnosis), while Figure 6.7 shows the corresponding autofluorescence images.

Table 6.1 - Patient data along with the corresponding histopathological results

	Age	Sex	Location of tumour	Histopathological Diagnosis
Patient 1	89	M	Trunk (right side)	Squamous cell carcinoma in situ
Patient 3	76	F	Lower left leg	Malignant melanoma
Patient 8	36	M	Trunk (back)	Benign nevus
Patient 12	85	F	Trunk (back)	Basal cell carcinoma
Patient 14	42	F	Left arm	Junction nevus with displasia
Patient 15	36	M	Trunk (left side)	Hemangioma

The first column in Figure 6.7 shows the grayscale images captured using white light illumination without any spectral filtering. The second column is the ratioed fluorescence images of 580 nm/ 460 nm, where the color-bars show the scale in dB. The third column is the ratioed fluorescence images of 440 nm/ 500 nm, where the color-bars show the scale in dB. The fourth column shows the raw fluorescence images at 480 nm, corresponding to the fluorescence peak of NADH. The raw images are plotted in a linear scale, rather than a log scale.

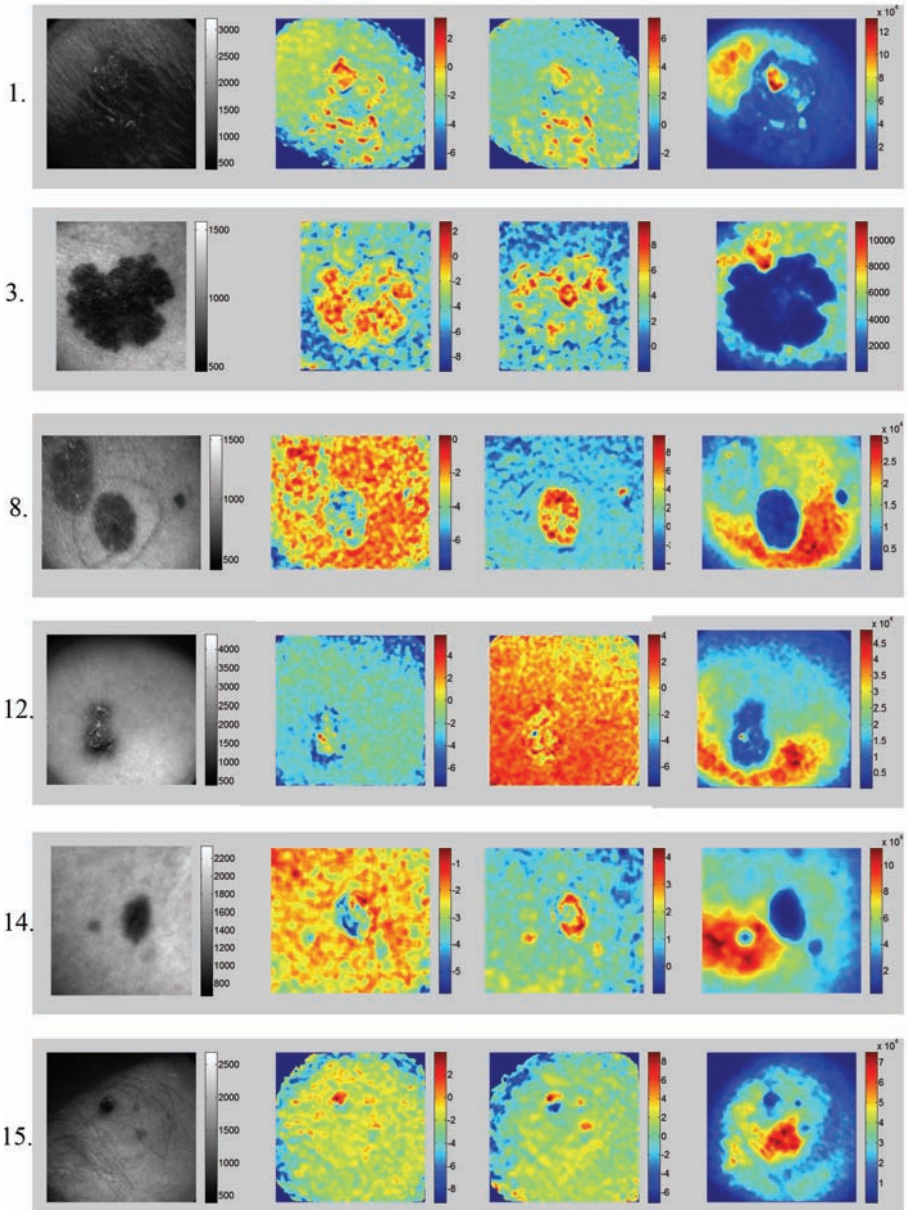

Figure 6.7 - Raw grayscale images of pigmented skin lesions (first column), ratioed fluorescence images at I(580 nm)/ I(460 nm), (second column), ratioed fluorescence images at I(440 nm)/I(500 nm), (third column), and finally, raw fluorescence images at 480 nm (fourth column).

It could be seen that in patient 8 and patient 14, the contrast in the ratioed images were particularly strong, which may be due to the stronger

fluorescence response in nevi when compared to melanoma, as previously reported in [88]. The ratioed signal from the nevi is slightly stronger than that coming from the surrounding tissue, which is true for both the 440 nm and 460 nm fluorescence. On the other hand, it could be seen that the raw fluorescence signal at 480 nm from the melanoma in patient 3 is particularly low, which is inline with fluorescence spectra previously reported in [87] and [88].

While previous reports on the emission spectrum of benign, malignant and normal skin tissue [88] suggest fluorescence signals between 430 nm and 450 nm may be of interest in detecting the NADH/NAD fluorescence contrast, thereby aiding in the differentiation between these types of lesions, the transmission of the liquid crystal filter is relatively low at the these wavelengths, ranging from 8% at 420 nm to 20% at 460 nm. Therefore, a higher transmission filter may be better able to produce higher contrast in the ratioed fluorescence images. Moreover, a higher power light source would allow shorter exposure times, reducing the blurring effects due to movement during image acquisition. Nonetheless, even with these deficiencies, the preliminary images show promising results.

6.3.6 Summary and Outlook

Preliminary results from the clinical study on pigmented skin lesions have been presented. Autofluorescence images were obtained using a pulsed excitation light source at 355 nm and a synchronously gated imaging system. This allowed for better signal-to-background ratio, to the extent that imaging in ambient room light is possible. The preliminary images from the clinical study show good contrast; however, further investigation into the optimal ratioing wavelengths with a larger sample set may be beneficial. In addition, using a light source at around 340 nm may better tune into the absorption peak of NADH, which may compensate for the low transmittance of the liquid crystal filter.

6.4 Unidirectional Ring Laser using χ^2 Non-linear Optics

To further explore the methods to suppress Q-switch mode-locking in the 946 nm laser, a ring laser is considered. As opposed to the standing-wave cavities that have been described so far, ring shaped resonators do not suffer from spatial hole-burning. Thus, they are more easily able to achieve single-mode operation, which would prevent mode-locking. However, differential loss needs to be introduced between the two directions of propagation to ensure stable single-mode operation. Traditionally, this is done by inserting a polarizer, a half-wave plate and a Faraday rotator into the ring cavity [13,90], but these are in general bulky and expensive.

In 1985, Kane and Byer proposed a non-planar monolithic ring laser that uses the laser crystal itself to perform all three functions of the polarizer, the half-wave plate and the Faraday rotator [91]. Figure 6.8 below illustrates their setup.

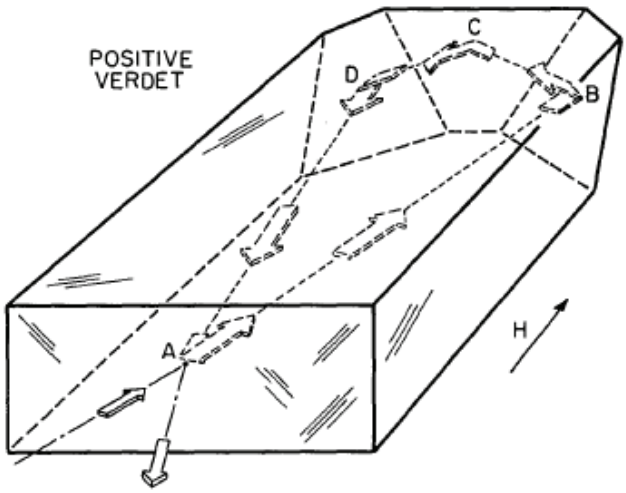

Figure 6.8 - Monolithic Nd:YAG ring laser. Source: Kane et al. [91].

A magnetic field is applied across the Nd:YAG laser crystal to induce the Faraday rotation along paths AB and DA. The two non-planar total internal reflections at points B and D rotates the polarization and act as the half-wave plate, and the output coupling surface at A discriminates one polarization against the other, thus acting as the polarizer. Due to the monolithic design, this laser is compact, single-frequency, and proved to be very stable [13]. A CW quasi-three-level monolithic ring laser at 946 nm [92], and a passively

Q-switched monolithic ring laser at 1064 nm [93] have also been reported previously.

Other methods for producing single-frequency, unidirectional lasing in ring cavities include using an acousto-optic modulator [94,95] and injection seeding [96]. These methods, however, are generally more cumbersome and increase the complexity of the system.

In this section, a novel unidirectional ring laser, using the differential loss induced by sum-frequency mixing to enforce single-frequency operation, is described. While a CW laser at 1342 nm is presented, the approach is generic and is applicable to both CW and Q-switched lasers. It may be particularly interesting for spectral regions where Faraday materials are not readily available.

It should be noted that Peter Tidemand-Lichtenberg performed most of the experimental work described here. The author only participated in some of the experiments and assisted in manuscript preparation.

6.4.1 Experimental Setup

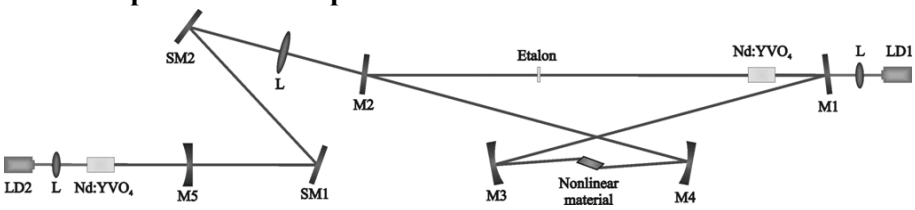

Figure 6.9 - Experimental setup for unidirectional ring laser based on non-linear parametric loss

Figure 6.9 shows the laser being considered. Mirrors M1, M2, M3, and M4 form the 815 mm long ring cavity at 1342 nm, while LD2 is the diode pump source for the single pass laser at 1064 nm, which is a hemispherical cavity bounded by the high reflection coating on the Nd:YVO_4 crystal and M5, the output coupler (r = -100 mm, $R_{1064\,nm}$ = 95%). M1 and M2 are plane mirrors, with high reflection coatings at 1342 nm and antireflection coatings at 1064 nm, while M3 and M4 are concave mirrors (r = -100 mm) with high reflection coatings at 1342 nm and 1064 nm. Both lasers were pumped by 3 W 808 nm fiber-coupled diode-lasers (Lumics LU0808M030).

A 10 mm long Brewster-cut PP:KTP crystal is phase-matched for sum-frequency mixing between the ring laser (at 1342 nm) and the single-pass

laser (at 1064 nm). It induces a non-linear loss in the two co-propagating beams. Because of this additional discriminative, non-linear loss, the ring laser would lase in the reverse direction, relative to the single-pass beam. The PP:KTP crystal had a poling period of 12.65 μm, which implies an optimum phase-matching temperature of 48 °C.

Sum-frequency mixing between three collinear plane waves in a lossless non-linear material can be described by the following set of coupled differential equations [6]:

$$\begin{aligned} \frac{da_i}{dz} &= -iga_g a_s^* \exp(-i\Delta kz) \\ \frac{da_s}{dz} &= -iga_g a_i^* \exp(-i\Delta kz) \\ \frac{da_g}{dz} &= -iga_s a_i \exp(-i\Delta kz) \end{aligned} \tag{6.2}$$

where $g^2 = 2\hbar\omega_i\omega_s\omega_g\eta^3 d^2_{eff}$ and $\Delta k = k_g - k_s - k_i$. The indices i, s and g are the intra-cavity, single-pass and generated fields respectively. a is the square root of the photon flux, while $\hbar$, ω, η and d_{eff} are the reduced Planck's constant, the angular frequency, the impedance and the second order non-linear coefficient respectively. If the power of the single-pass laser is not depleted, the parametric loss, $L_{parametric}$, induced by the non-linear process on the co-propagating intracavity beam is then:

$$L_{parametric} = \frac{g^2 L^2}{\hbar\omega_s} I_s \left(\frac{\sin(\frac{1}{2}\Delta kL)}{(\frac{1}{2}\Delta kL)} \right)^2 \tag{6.3}$$

where I_s is the intensity of the single-pass laser and L is the length of the non-linear crystal.

For the non-planar monolithic ring laser considered in [91], a loss difference of 0.01% was calculated. According to equation (6.3), a loss difference of 0.01% can be realized with an external single-pass laser power of less than 100 mW at optimum phase-matching. However, as the actual loss difference necessary to obtain unidirectional operation depends on mechanical stability, which would be excellent in a monolithic laser, a significantly larger loss

difference is needed for stable operation in the non-linear setup currently described.

6.4.2 Experimental Results

To contrast the effect of the non-linear loss, the single-pass laser was modulated with a mechanical chopper, and two photodiodes were used to measure the power generated in the two directions of propagation. Figure 6.10 shows chaotic bidirectional operation of the ring laser when the single-pass laser is blocked by the mechanical chopper and stable unidirectional operation when the single-pass laser is not blocked by the chopper. Contrary to what might be expected in sum-frequency generation (SFG) in the normal approach, the SFG yellow power, propagating in the direction of the single-pass laser, dropped to zero when the phase-matching temperature was reached, which confirmed that the co-propagating 1342 nm field in the ring laser ceased to lase, and that the single-pass beam was not depleted.

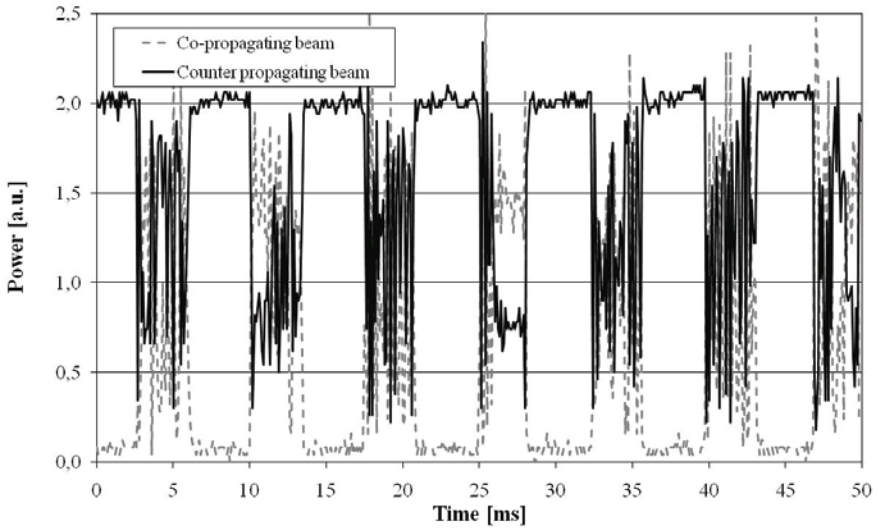

Figure 6.10 - Measured 1342 nm power in the ring cavity for the beam co-propagating with the single-pass laser, and the beam counter-propagating with the single-pass laser.

The power of the single-pass laser was 0.5 W in these experiments, corresponding to a theoretically calculated parametric loss of approximately 0.1 %. Experimentally, unidirectional operation was maintained within ±2 °C of the optimum phase-matching temperature, indicating that a parametric loss as low as 0.05 % was sufficient to ensure stable unidirectional operation.

6.4.3 Summary and outlook

Using the proposed nonlinear optical approach, stable unidirectional operation of a ring laser was demonstrated. The principle relies on a second order parametric process and is limited only by the transparency range and phase-matching properties of the available nonlinear materials. Furthermore, the differential loss can be controlled dynamically by varying the power of the single-pass laser. A unidirectional, single-mode 946 nm ring laser seem feasible, which would then prevent the Q-switched mode-locking behavior currently observed.

7. Conclusion

In conclusion, the work reported here paves the way for a compact, cost-effective, pulsed UV laser light source based on efficient operation of a quasi-three-level laser and passively synchronized Q-switching.

Optimization of the quasi-three-level laser under CW operation has been studied and the experimental results show that a broad-spectrum tapered diode pump source may provide the best compromise between output power and output stability.

Q-switched operation of a quasi-three-level laser has also been investigated. Using an all passive approach, a quasi-three-level and a four-level Q-switched Nd:YAG laser had been synchronized stably for the first time. Temporal overlap between the two lasers was 79% when normalized against the zero-delay scenario. The minimum timing jitter was 9 ns, which was comparable to an actively synchronized system previously reported in the literature. The theoretical lower limit for the relative timing jitter was found to be 6 ns. Comparing this with the experimental result highlights the stability of the passive synchronization.

Preliminary clinical trials using a 355 nm laser excitation source for autofluorescence imaging obtained promising results, but would benefit from a laser at 340 nm that could tune into the absorption peak of NADH.

Based on the temporal performance obtained, a high peak power 340 nm laser using sum-frequency generation seems feasible. While the results are presented from the perspective of non-linear conversion to 340 nm, the approach is generic to other laser transitions, particularly the relatively short wavelength quasi-three-level transitions that would extend the spectral coverage of SFG into the UV. Furthermore, by achieving synchronized Q-switching using only passive optical components, the system complexity, footprint, and cost are minimized. It would seem, then, a new approach based on efficient operation of quasi-three-level lasers and their sum-frequency generation through passively synchronized Q-switching could bring a new generation of compact, efficient, cost-effective, pulsed blue and UV light sources into realization.

Source: Banksy.

References

[1] Z. Y. Ou, S. F. Pereira, E. S. Polzik, and H. J. Kimble, "85-percent efficiency for CW frequency doubling from 1.08 to 0.54 μm," Opt. Lett. **17**, 640-642 (1992).

[2] W. Seka, S. D. Jacobs, J. E. Rizzo, R. Boni, and R. S. Craxton, "Demonstration of high efficiency third harmonic conversion of high power Nd-glass laser radiation," Opt. Commun. **34**, 469-473 (1980).

[3] B. C. Wu, N. Chen, C. T. Chen, D. Q. Deng, and Z. Y. Xu, "Highly efficient ultraviolet generation at 355 nm in LiB_3O_5," Opt. Lett. **14**, 1080-1081 (1989).

[4] T. Kojima, S. Konno, S. Fujikawa, K. Yasui, and K. Yoshizawa, "20-W ultraviolet-beam generation by fourth-harmonic generation of an all-solid-state laser," Opt. Lett. **25**, 58-60 (2000).

[5] O. P. Kimmelma, I. Tittonen, and S. C. Buchter, "Short pulse, diode pumped, passively Q-switched Nd:YAG laser at 946 nm quadrupled for UV production," J. Europ. Opt. Soc. Rap. Public. **3**, 08008 (2008).

[6] B. E. A. Saleh and M. C. Teich, *Fundamental of Photonics 1st ed.* (Wiley-Interscience, New York, NY, 1991).

[7] B. F. Aull and H. P. Jenssen, "Vibronic interactions in Nd-YAG resulting in nonreciprocity of absorption and stimulated-emission cross-sections," IEEE J. Quantum Electron. **18**, 925-930 (1982).

[8] J. N. Walpole, "Semiconductor amplifiers and lasers with tapered gain regions," Opt. Quantum Electron. **28**, 623-645 (1996).

[9] P. A. Yazaki, K. Komori, G. Bendelli, S. Arai, and Y. Suematsu, "A GaInAsP/InP tapered-waveguide semiconductor laser amplifier integrated with a 1.5 μm distributed feedback laser," IEEE Photonics Technol. Lett. **3**, 1060-1063 (1991).

[10] J. N. Walpole, E. S. Kintzer, S. R. Chinn, C. A. Wang, and L. J. Missaggia, "High-power strained-layer InGaAs/AlGaAs tapered traveling wave amplifier," Appl. Phys. Lett. **61**, 740-742 (1992).

[11] J. Holm Lundeman, *Blue Laser Source for Laser-Induced Fluorescence*, PhD Thesis (Lund University, Lund, Sweden, 2008).

[12] T. Y. Fan and R. L. Byer, "Modeling and CW operation of a quasi-three-level 946 nm Nd:YAG laser," IEEE J. Quantum Electron. **QE-23**, 605-612 (1987).

[13] W. Koechner, *Solid-State Laser Engineering 6th ed.*, (Springer, Round Hill, VA, 2006).

[14] W. P. Risk, "Modeling of longitudinally pumped solid-state lasers exhibiting reabsorption losses," J. Opt. Soc. Am. B **5**, 1412-1423 (1988).

[15] I. D. Lindsay and M. Ebrahimzadeh, "Efficient continuous-wave and Q-switched operation of a 946-nm Nd:YAG laser pumped by an injection-locked broad-area diode laser," Appl. Opt. **37**, 3961-3970 (1998).

[16] T. Y. Fan and R. L. Byer, "Continuous-wave operation of a room-temperature, diode-laser-pumped, 946-nm Nd:YAG laser," Opt. Lett. **12**, 809-811 (1987).

[17] A. Giesen, H. Hugel, A. Voss, K. Wittig, U. Brauch, and H. Opower, "Scalable concept for diode-pumped high-power solid-state lasers," Appl. Phys. B **58**, 365-372 (1994).

[18] J. P. Cuthbertson and G. J. Dixon, "Pump-resonant excitation of the 946-nm Nd:YAG laser," Opt. Lett. **16**, 396-398 (1991).

[19] G. Hollemann, E. Peik, and H. Walther, "Frequency-stabilized diode-pumped Nd:YAG laser at 946 nm with harmonics at 473 and 237 nm," Opt. Lett. **19**, 192-194 (1994).

[20] D. Paboeuf, G. Lucas-Leclin, P. Georges, B. Sumpf, G. Erbert, C. Varona, P. Loiseau, G. Aka, B. Ferrand, "Blue laser emission by intracavity second harmonic generation in Nd:ASL pumped by a tapered amplifier laser diode stabilized by a volume Bragg grating," Appl. Phys. B **92**, 189-193 (2008).

[21] W. A. Clarkson, R. Koch, and D. C. Hanna, "Room-temperature diode-bar-pumped Nd:YAG laser at 946 nm," Opt. Lett. **21**, 737-739 (1996).

[22] T. Kellner, F. Heine, and G. Huber, "Efficient laser performance of Nd:YAG at 946 nm and intracavity frequency doubling with $LiJO_3$, β-BaB_2O_4, and LiB_3O_5," Appl. Phys. B **65**, 789-792 (1997),

[23] R. Zhou, E. Li, H. Li, P. Wang, and J. Yao, "Continuous-wave, 15.2 W diode-end-pumped Nd:YAG laser operating at 946 nm," Opt. Lett. **31**, 1869-1871 (2006).

[24] D. Vijayakumar, O. B. Jensen, R. Ostendorf, T. Westphalen, and B. Thestrup, "Spectral beam combining of a 980 nm tapered diode laser bar," Opt. Express **18**, 893-898 (2010).

[25] D. Paboeuf, G. Lucas-Leclin, P. Georges, N. Michel, M. Krakowski, J. Lim, S. Sujecki, and E. Larkins, "Narrow-line coherently combined

tapered laser diodes in a Talbot external cavity with a volume Bragg grating," Appl. Phys. Lett. **93**, 211102 (2008).

[26] F. Auge, F. Druon, F. Balembois, P. Georges, A. Brun, F. Mougel, G. Aka, and D. Vivien, "Theoretical and experimental investigations of a diode-pumped quasi-three-level laser: The Yb^{3+}-doped $Ca_4GdO(BO_3)_3$ (Yb:GdCOB) laser," IEEE J. Quantum Electron. **36**, 598-606 (2000).

[27] M. J. Chi, O. B. Jensen, J. Holm, C. Pedersen, P. E. Andersen, G. Erbert, B. Sumpf, and P. M. Petersen, "Tunable high-power narrow-linewidth semiconductor laser based on an external-cavity tapered amplifier ," Opt. Express. **13**, 10589-10596 (2005).

[28] NASA Database LASERS, <http://www.mennerat.fr/gab/References/DatabaseLasers/spectra/spectra.htm> Accessed June 24, 2010.

[29] D. E. Zelmon, D. L. Small, and R. Page, "Refractive-index measurements of undoped yttrium aluminum garnet from 0.4 to 5.0 μm" Appl. Opt. 37 (1998) 4933-4935.

[30] N. P. Barnes and B. M. Walsh, "Quantum efficiency measurements of Nd:YAG, Yb:YAG, and Tm:YAG," in *OSA TOPS Advanced Solid-State Lasers*, **68**, 284-287 (2002).

[31] N. Pavel, "In-band pumping of Nd-based solid-state lasers," Rom. Rep. Phys. **60**, 995-1012 (2008).

[32] S. Bjurshagen and R. Koch, "Modeling of energy-transfer upconversion and thermal effects in end-pumped quasi-three-level lasers," Appl. Opt. **43**, 4753-4767 (2004).

[33] P. Tidemand-Lichtenberg, M. T. Andersen, S. Johansson, C. Canalias, F. Laurell, P. Buchhave, E. Karamehmedovic, and C. Pedersen, "Nonlinear cavity dumping of a high finesse frequency mixing module," Opt. Express **15**, 9799-9803 (2007).

[34] H. Liu, O. Hornia, Y. C. Chen, and S. H. Zhou, "Single-frequency Q-switched Cr-Nd:YAG laser operating at 946-nm wavelength," IEEE J. Sel. Top. Quantum Electron. **3**, 26-28 (1997).

[35] O. Kimmelma, M. Kaivola, I. Tittonen, and S. Buchter, "Short pulse, high peak power, diode pumped, passively Q-switched 946 nm Nd:YAG laser," Opt. Commun. **273**, 496-499 (2007).

[36] C. W. Wang, Y. L. Weng, P. L. Huang, H. Z. Cheng, and S. L. Huang, "Passively Q-switched quasi-three-level laser and its intracavity frequency doubling," Appl. Opt. **41**, 1075-1081 (2002).

[37] X. B. Chen, L. Wang, J. G. Zhu, L. B. Lv, Z. G. Zhang, G. Z. Yang, W. M. Du, and D. Z. Zhang, "Study of diode-laser pumped self-Q-switched intracavity-doubled laser of $Cr^{4+}Nd^{3+}$:YAG plus $KNbO_3$ material," Opt. Eng. **43**, 1350-1354 (2004).

[38] Q. Li, B. Feng, D. Zhang, S. Du, Y. Shi, Z. Zhang, and S. Zhang, "Numerical solution and experiment of a self-Q-switched 946 nm Cr,Nd:YAG laser," Appl. Phys. B **93**, 421-427 (2008).

[39] T. Kellner, F. Heine, G. Huber, and S. Kück, "Passive Q switching of a diode-pumped 946-nm Nd:YAG laser with 1.6-W average output power," Appl. Opt. **37**, 7076-7079 (1998).

[40] Y. P. Huang, K. W. Su, A. Li, Y. F. Chen, and K. F. Huang, "High-peak-power passively Q-switched Nd:YAG laser at 946 nm," Appl. Phys. B **91**, 429-432 (2008).

[41] S. M. Wang, Q. L. Zhang, L. Zhang, C. Y. Zhang, D. X. Zhang, B. H. Feng, and Z. G. Zhang, "Diode-pumped passive Q-switched 946 nm Nd:YAG laser with a GaAs saturable absorber," Chin. Phys. Lett. **23**, 619-621 (2006).

[42] J. Hong, B. D. Sinclair, W. Sibbett, and M. H. Dunn, "Frequency-doubled and Q-switched 946-nm Nd:YAG laser pumped by a diode-laser array," Appl. Opt. **31**, 1318-1321 (1992).

[43] X. Zhang, A. Brenier, J. Want, and H. Zhang, "Absorption cross-sections of Cr^{4+}:YAG at 946 and 914 nm," Opt. Mat. **26**, 293-296 (2004).

[44] Q. Li, S. Wang, S. Du, Y. Shi, J. Xing, D. Zhang, B. Feng, Z. Zhang, and S. Zhang, "Self-Q-switched and mode-locked 946 nm Cr,Nd:YAG laser," Opt. Commun. **281**, 2184-2188 (2008).

[45] L. Zhang, D. Li, Q. Zhang, C. Li, Z. Wei, B. Feng, P. Fu, and Z. Zhang, "Diode-pumped passive Q-switched and mode-locked 946 nm Nd:YAG laser with a Nd,Cr:YAG saturable absorber," Opt. Commun. **250**, 174-177 (2005).

[46] Y. F. Chen, J. L. Lee, H. D. Hsieh, and S. W. Tsai, "Analysis of passively Q-switched lasers with simultaneous modelocking," IEEE J. Quantum Electron. **38**, 312-317 (2002).

[47] A. L. Shawlow, and G. E. Devlin, "Simultaneous optical maser action in two ruby satellite lines," Physical Review Letters **6**, 96-98 (1961).

[48] T. H. Maiman, "Stimulated optical radiation in ruby," Nature **187**, 493-494 (1960).

[49] H. W. Gandy, and R. J. Ginther, "Simultaneous Laser Action of Neodymium and Ytterbium Ions in Silicate Glass," in Proceedings of the IRE, 2114-2115 (1962).

[50] J. D. Rigden, and A. D. White, "Simultaneous Gas Maser Action in the Visible and Infrared," in Proceedings of the IRE, 2366-2367 (1962).

[51] H. Nelson, and G. C. Dousmanis, "Effect of impurity distribution on simultaneous laser action in GaAs at 0.84 and 0.88 μ," Applied Physics Letters **4**, 192-194 (1964).

[52] W. R. Bennett, and J. W. Knutson, "Simultaneous Laser Oscillation on the Neon Doublet at 1.1523 μ," in Proceedings of the IEEE, 861-862 (1964).

[53] D. W. Gregg, and S. T. Thomas, "Simultaneous Giant Pulses from Five Ruby Laser Oscillators," Journal of Applied Physics **37**, 3750-3753 (1966).

[54] J. A. Calviello, E. W. Fisher, and Z. H. Heller, "Simultaneous Laser Oscillation at R1 and R2 Wavelengths in Ruby," IEEE Journal of Quantum Electronics **QE1**, 132 (1965).

[55] G. A. Henderson, "A computational model of a dual-wavelength solid-state laser," J. Appl. Phys. **68**, 5451-5455 (1990).

[56] H. Y. Shen, "Oscillation condition of simultaneous multiple wavelength lasing," Chinese Phys. Lett. **7**, 174-176 (1990).

[57] W. Lin , and H. Shen, "A configuration of the laser cavity for simultaneous dual wavelength Q-switch pulsed Nd:$YAlO_3$ laser," J. Appl. Phys. **86**, 2979-2983 (1999).

[58] P. Tidemand-Lichtenberg, J. Janousek, R. Melich, J. L. Mortensen, and P. Buchave, "Synchronization of 1064 and 1342 nm pulses using passive saturable absorbers," Opt. Commun. **241**, 487-492 (2004).

[59] J. Janousek, P. Tidemand-Lichtenberg, J. L. Mortensen, and P. Buchave, "Investigation of passively synchronized dual-wavelength Q-switched lasers based on V:YAG saturable absorber," Opt. Commun. **265**, 277-282 (2006).

[60] C. G. Bethea, "Megawatt Power at 1.318 μ in Nd^{3+}:YAG and Simultaneous Oscillation at Both 1.06 and 1.318 μ," IEEE J. Quantum Electron. **9**, 254 (1973).

[61] R. W. Farley, and P. D. Dao "Development of an intracavity-summed multiple-wavelength Nd:YAG laser for a rugged, solid-state sodium lidar system," Appl. Optics **34**, 4269-4273 (1995).

[62] R. A. Morgan, F. A. Hopf, and N. Peyghambarian, "Dual-frequency Nd:YAG laser for the study and application of nonlinear optical crystals," Opt. Eng. **26**, 1240-1244 (1987).

[63] C. H. Huang, G. Zhang, Y. Wei, L. X. Huang, and H. Y. Zhu, "A Q-switched Nd:$YAlO_3$ laser emitting 1080 and 1342 nm," Opt. Commun. **281**, 3820-3823 (2008).

[64] Y. F. Chen and S. W. Tsai, "Diode-pumped Q-switched Nd:YVO_4 yellow laser with intracavity sum-frequency mixing," Opt. Lett. **27**, 397-399 (2002).

[65] W. K. Chang, Y. H. Chen, and J. W. Chang, "Pulsed orange generation optimized in a diode-pumped Nd:YVO4 laser using monolithic dual PPLN electro-optic Q switches," Opt. Lett. **35**, 2687-2689 (2010).

[66] H. T. Huang, J. L. he, B. T. Zhang, J. F. Yang, J. L. Xu, C. H. Zuo, and X. T. Tao, "V^{3+}:YAG as the saturable absorber for a diode pumped quasi-three-level dual-wavelength Nd:GGG laser," Opt. Express **18**, 3352-3357 (2010).

[67] L. Zhang, Z. Wei, B. Feng, D. Li, and Z. Zhang, "Simultaneous dual-wavelength Q-switched Nd:YAG laser operating at 1.06 μm and 946 nm," Opt. Commun. **264**, 51-54 (2006).

[68] T. Y. Tsai, Y. C. Fang, H. M. Huang, H. X. Tsao, and S. T. Lin, "Saturable absorber Q- and gain-switched all-Yb^{3+} all-fiber laser at 976 and 1064 nm," Opt. Express **18**, 23523-23528 (2010).

[69] E. Herault, M. Lelek, F. Balembois, and P. Georges, "Pulsed blue laser at 491 nm by nonlinear cavity dumping," Opt. Express **16**, 19419-19426 (2008).

[70] B. M. Walsh, "Dual Wavelength Lasers," Laser Phys. **20**, 622-634 (2010).

[71] P. X. Li, D. H. Li, C. Y Li, and Z. G. Zhang, "Simultaneous dual-wavelength continuous wave laser operation at 1.06 μm and 946 nm in Nd:YAG and their frequency doubling," Opt. Commun. **235**, 169-174 (2004).

[72] K. Lunstedt, N. Pavel, K. Petermann, and G. Huber, "Continuous-wave simultaneous dual-wavelength operation at 912 nm and 1063 nm in Nd:GdVO4," Appl. Phys. B **86**, 65-70 (2007).

[73] V. Kh. Bagdasarov, N. N. Denisov, A. A. Malyutin, and I. A. Chigaev, "Pulse synchronisation in passively Q-switched lasers

emitting at 1.053 and 1.064 μm," Quantum Electron. **39**, 887-890 (2009).

[74] B. H. Soffer, and B. B. McFarland, "Frequency locking and dy spectal hole burning in Q-spoiled lasers," Appl. Phys. Lett. **8**, 166-169 (1966).

[75] H. Opower, and W. Kaiser, "Synchronization of giant pulse lasers," Physics Letters **21**, 638-640 (1966).

[76] H. P. H. Cheng, P. Tidemand-Lichtenberg, O. B. Jensen, P. E. Andersen, P. M. Petersen, and C. Pedersen, "All passive synchronized Q-switching of a quasi-three-level and a four-level Nd:YAG laser," Opt. Express **18**, 23987-23993 (2010).

[77] J. B. Khurgin, F. Jin, G. Solyar, C. C. Wang, and S. Trivedi, "Cost-effective low timing jitter passively Q-switched diode-pumped solid-state laser with composite pumping pulses," Appl. Opt. **41**, 1095-1097 (2002).

[78] S. L. Huang, T. Y. Tsui, C. H. Wang, and F. J. Kao, "Timing jitter reduction of a passively Q-switched laser," Jpn. J. Appl. Phys. **38**, L239-L241 (1999).

[79] X. Wang and Z. Xu, "Timing jitter reduction and single-frequency operation in an acousto-optic Q-switched Cr,Nd:YAG laser," Appl. Opt. **45**, 8477-8483 (2006).

[80] B. Cole, L. Goldberg, C. W. Trussell, A. Hays, B. W. Schilling, and C. McIntosh, "Reduction of timing jitter in a Q-switched Nd:YAG laser by direct bleaching of a Cr4+:YAG saturable absorber," Opt. Express **17**, 1766-1771 (2009).

[81] A. Steinmetz, D. Nodop, A. Martin, J. Limpert, and A. Tünnermann, "Reduction of timing jitter in passively Q-switched microchip lasers using self-injection seeding," Opt. Lett. **35**, 2885-2887 (2010).

[82] H. P. H. Cheng, P. Tidemand-Lichtenberg, O. B. Jensen, P. E. Andersen, P. M. Petersen, and C. Pedersen, "Experimental investigation of relative timing jitter in passively synchronized *Q*-switched lasers," Opt. Lett. **36**, 415-417 (2011).

[83] H. Xie, H. Liu, P. Svenmarker, J. Axelsson, C. T. Xu, S. Gräfe, J. H. Lundeman, H. P. H. Cheng, S. Svanberg, N. Bendsoe, P. E. Andersen, K. Svanberg, and S. Andersson-Engels, "Drug quantification in turbid media by fluorescence imaging combined with light-absorption correction using White Monte Carlo Simulations," J. Biomed. Opt. (under review).

[84] J. H. Lundeman, O. B. Jensen, P. E. Andersen, S. Andersson-Engels, B. Sumpf, G. Erbert, and P. M. Petersen, "High power 404 nm source based on second harmonic generation in PPKTP of a tapered external feedback diode laser," Opt. Express **16**, 2486-2493 (2008).

[85] J. H. Lundeman, O. B. Jensen, P. E. Andersen, and P. M. Petersen, "Threshold for strong thermal dephasing in periodically poled KTP in external cavity frequency doubling," Appl. Phys. B **96**, 827-831 (2009).

[86] B. W. Chwirot, S. Chwirot, N. Sypniewska, Z. Michniewicz, J. Redzinski, G. Kurzawski, and W. Ruka, "Fluorescence in situ detection of human cutaneous melanoma: study of diagnostic parameters of the method," Journal of Investigative Dermatology **117**, 1449-1451 (2001).

[87] W. Lohmann and E. Paul, "In situ Detection of Melanomas by Fluorescence Measurements," Naturwissenschaften **75**, 201-202 (1988).

[88] P. Troyanova, E. Borisova, V. Stoyanova, and L. Avramov, "Laser-induced autofluorescence spectroscopy of benign and dysplastic nevi and malignant melanoma," Proc. SPIE 6284, 62840K (2006).

[89] E. Borisova, E. Dogandjiiska, I. Bliznakova, L. Avramov, E. Pavlova, and P. Troyanova, "Multispectral autofluorescence diagnosis of non-melanoma cutaneous tumors," Proc. of SPIE-OSA Biomedical Optics, SPIE Vol. 7368, 736823 (2009).

[90] A. R. Clobes and M. J. Brienza, "Single-frequency traveling-wave Nd:YAG laser," Appl. Phys. Lett. **21**, 265-267 (1972).

[91] T. J. Kane and R. L. Byer, "Monolithic, unidirectional single-mode Nd:YAG ring laser," Opt. Lett. **10**, 65-67 (1985).

[92] I. Freitag, R. Henking, A. Tünnermann, and H. Welling, "Quasi-three-level room-temperature Nd:YAG ring laser with high single-frequency output power at 946 nm," Opt. Lett. **20**, 2499-2501 (1995).

[93] I. Freitag, A. Tünnermann, and H. Welling, "Passively *Q*-switched Nd:YAG ring lasers with high average output power in single-frequency operation," Opt. Lett. **22**, 706-708 (1997).

[94] W. A. Clarkson and D. C. Hanna, "Acousto-optically induced unidirectional single mode operation of a Q-switched miniature Nd:YAG ring laser," Opt. Comm. **81**, 375-378 (1991).

[95] D. Y. Shen, W. A. Clarkson, L. J. Cooper and R. B. Williams, "Efficient single-axial-mode operation of a Ho:YAG ring laser pumped by a Tm-doped silica fiber laser," Opt. Lett. **29**, 2396-2398 (2004).

[96] Y. K. Park, G. Guiliani, and R. L. Byer, “Single Axial Mode Operation of a Q-Switched Nd:YAG Oscillator by Injection Seeding,” IEEE J. Quantum Electron. **QE-20**, 117-125 (1984).

Appendix: Derivation of Steady State Condition

$$2\iiint_{crystal} G \cdot I \, dV = P\delta; \qquad G = \sigma \Delta N$$

The optical intensity going in one direction inside the laser crystal:

$$I = h\nu\left(S\, r_c(r,z)\right)\frac{c}{n}\frac{1}{2}$$

where:

$$S \equiv \text{total number of photons in cavity}$$

$$r_c(r,z) \equiv \frac{1}{\text{laser cavity mode volume}}$$

$$S\, r_c(r,z) = \text{photon density}$$

The intracavity power, P, is:

$$P = h\nu\frac{S}{2l_{cav}}c; \qquad l_{cav} \equiv \text{optical length of cavity}$$

The steady state integral then becomes:

$$2\iiint_{crystal} \sigma \Delta N \; S\, r_c(r,z)\frac{1}{n}dV = \frac{S}{l_{cav}}\delta$$

$$\frac{2\sigma l_{cav}}{n}\iiint_{crystal} \Delta N \, r_c(r,z)dV = \delta$$

For $l_{cav} = l_{xtal}$ = length of crystal:

$$P = h\nu\frac{S}{2l_{xtal}}\frac{c}{n}$$

$$2\iiint_{crystal} \sigma \Delta N \; S\, r_c(r,z)\frac{1}{n}dV = \frac{S}{nl_{xtal}}\delta$$

$$2\sigma l_{xtal}\iiint_{crystal} \Delta N \, r_c(r,z)dV = \delta$$